INTERREG-V OCEAN INDIEN 2014-2020

Projet de Recherche

RENOVRISK-CYCLONES ET CHANGEMENT CLIMATIQUE

Axe-1 OT-1 OS-01a - Action I-3 TF

Livrable 16

Rapport ou publication sur l'analyse des modèles de houle, depuis l'échelle du bassin jusqu'à l'échelle locale avec les observations directes de terrain (sismologiques, pression de fond de mer, bouées)

Elisa RINDRAHARISAONA et Emmanuel CORDIER
Geosciences Réunion / OSU-Réunion

Mars 2021

Ce livrable est associé à la sous-action 2.3 intitulée :

Simulations numériques à haute-résolution

Ces travaux ont fait l'objet de deux publications de Mme Elisa Rindraharisaona et al. (2020, 2021), reproduites ci-après, comparant les simulations et analyses des modèles de houles GOW2 et WW3 avec un ensemble de données issues d'observations.

Une autre publication (Pianezze et al. 2019), basée sur des travaux menés en parallèle du projet, et dont les résultats ont ensuite été exploités dans RNR-C3 est également jointe à la fin du document.

Geophysical Journal International

Geophys. J. Int. (2020) **221,** 1883–1895
Advance Access publication 2020 March 13
0GJI Seismology

doi: 10.1093/gji/ggaa117

Assessing swells in La Réunion Island from terrestrial seismic observations, oceanographic records and offshore wave models

E.J. Rindraharisaona [1,2] E. Cordier,[3] G. Barruol [1] F. R. Fontaine [1,2] and M. Singh[4]

[1] *Université de Paris, Institut de physique du globe de Paris, CNRS, F-75005 Paris, France. E-mail: elisajosia@gmail.com*
[2] *Université de La Réunion, Laboratoire GéoSciences Réunion, F-97744, Saint Denis, France*
[3] *Observatoire des Sciences de l'Université de La Réunion, UMS3365 (CNRS, Université de La Réunion, Météo-France), Saint-Denis de La Réunion, France*
[4] *Mauritius Oceanography Institute, Albion, Mauritius*

Accepted 2020 March 9. Received 2020 March 6; in original form 2019 November 27

SUMMARY

La Réunion Island in the southwest Indian Ocean is seasonally affected by austral swells among which some extreme events may have strong impacts on coastal infrastructures. The very limited number of sensors available on and around the island and in the whole SW Indian Ocean impedes any direct monitoring of the swell activity. In this study, we analyse direct observations of the ocean swell by combining terrestrial measurements of the microseismic noise with *in situ* oceanographic observations issued from two pressure gauges and an Acoustic Doppler Current Profiler (ADCP), together with swell numerical modelling. The reliability of the terrestrial seismic station to characterize the ocean activity in both the primary and secondary microseisms peaks (PM and SM, respectively), and also in the long period secondary microseismic peak (LPSM) for the case of La Réunion Island is presented and discussed here. By computing the hourly RMS of the PM and LP(SM) amplitudes, we establish a transfer function between the PM and (LP)SM amplitude and the maximum wave height, which appears to be valid for any PM and LPSM amplitudes >0.15 μm and >1.0 μm, respectively. The correlation coefficient between the PM amplitude and the wave height is >0.92. It suggests that the PM amplitude can be used as a robust proxy for the swell height and may help calibrating the wave heights from other independent observable. For some swell events, we observe LPSM that correlate well (>0.91) with the local wave height suggesting a generation by coastal swell reflection. From polarization and spectral analyses, directions and periods of swells are also well retrieved from seismic data. Finally, continuous measure of the SM amplitude shows that it can be used as precursor information for distant swells that may hit La Réunion Island a few days after their generation in the southern Indian Ocean.

Key words: Indian Ocean; Seismic noise; Surface waves and free oscillations.

1 INTRODUCTION

La Réunion Island is located in the southwest (SW) Indian Ocean (Fig. 1). It is affected by sporadic oceanic swells generated by tropical cyclones (occurring mainly during summer periods, i.e. from November to March) or by austral swell events (observed in austral winter, from April to October). Austral swells that reach La Réunion Island are generated by distant storms in the Southern Indian Ocean at distance of 3000–4000 km (e.g. Davy *et al.* 2015). Generated by strong winds and long fetches within strong atmospheric depressions circulating around Antarctica, the swells may take a few days to reach La Réunion Island, where it may produce significant damage to the coastal infrastructures such as roads, houses, harbors, but also to the natural coral reef protecting part of the western coast of La Réunion (e.g. Cordier *et al.* 2012). Monitoring the swell activity around the island and in the SW Indian Ocean is therefore of broad interest but is strongly limited by the little number of oceanographic sensors available. To extend the work of Davy *et al.* (2014, 2015, 2016) and Barruol *et al.* (2016), we analyse the ocean-induced microseismic noise recorded by terrestrial seismic stations installed on La Réunion Island, and we combine those observables with *in situ* ocean observations issued from two pressure sensors (OSSI, Ocean Sensor Systems Inc.) deployed in the fringing reef and off shore, and an ADCP (Acoustic Doppler Current Profiler, Nortek Aquadopp Profiler) deployed off shore (Figs 1b and c).

Microseisms have been long known to be generated by ocean gravity waves (e.g. Longuet-Higgins 1950) and can be recorded by seismic stations worldwide. The existence of two types of microseisms—the Primary and Secondary Microseisms (PM and SM, respectively), which differ from their dominant periods and

origins—is broadly accepted despite their origins and the involved processes are still actively studied (e.g. Ardhuin *et al.* 2011, 2015). PM are accepted to occur in coastal waters and concentrate the energy at the same period as the ocean swell, that is at periods ∼10–20 s (frequencies between 0.05 and 0.10 Hz). They are interpreted as the interaction between sloping seafloor and the approaching ocean waves (e.g. Hasselmann 1963; Barruol *et al.* 2006; Ardhuin *et al.* 2015). On the other hand, SM are accepted to be generated within the ocean basins by the interaction of two swells of same periods propagating in opposite directions (e.g. Longuet-Higgins 1950), generating standing waves and vertical pressure variations across the water column, that excite seismic waves on the ocean bottom. SM therefore dominate at half the dominant swell periods, that is between ∼3 and 10 s (frequencies between ∼0.10 and 0.33 Hz). SM sources have been located (1) in the open ocean where standing waves are created by the interaction of two distant swells (e.g. Obrebski *et al.* 2012), (2) in coastal regions where a swell reflected at the coast may interact with the incoming waves (e.g. Ardhuin *et al.* 2011; Stutzmann *et al.* 2012; Bromirski *et al.* 2013), generating the so-called long period secondary microseism (LPSM) and (3) in a storm due to the interaction of two waves from opposite directions issued from the same system or waves issued from two different storms (e.g. Ardhuin *et al.* 2011; Obrebski *et al.* 2013; Davy *et al.* 2014).

In this study, we analyse a sequence of austral swells that hit La Réunion Island between 13 March and 5 May 2017.

On land, we analyse the seismological data to determine the dominant frequency of the PM and SM using the power spectral density analysis that may provide a link to the swell peak period T_p; we quantify the microseismic amplitudes by computing an hourly root mean square (RMS) in each frequency band that provides information on the local or distant significant wave height H_s (in the case of the PM or SM band, respectively); we finally perform a polarization analysis to determine the dominant direction and strength of polarization of the recorded microseismic noise, that may indicate the wave peak direction D_p for the case of the PM band or the source direction in the SM band.

At sea, oceanographic sensors were deployed during this period inside and outside the fringing reef along the west coast of La Réunion Island: one sensor on the reef flat and two others on the reef external slope (Fig. 1). Such *in situ* measurements allowed us to derive the local wave heights and periods from bottom pressure gauges and the swell direction from the ADCP sensor. We used those oceanographic observations, together with the land seismological data and the WaveWatch III (WWIII) swell models to establish relations between the observed and modelled swell parameters. One of the objectives of this work is indeed to establish the relationship between the land-recorded seismological PM amplitudes and the ocean-observed significant wave height (H_s, measured by the OSSI pressure wave gauge) and to demonstrate that the PM can be used as a proxy of the H_s, and therefore, that a land seismometer can be used as a well calibrated swell gauge. We also evaluate the accuracy of the modelled swell direction, height and period (respectively D_{pm}, H_{sm} and T_{pm} parameters) derived from numerical models (WWIII) in the west of La Réunion Island by comparing them with the observed parameters. These approaches allow us to compute the transfer function relating the microseism amplitudes (in the PM and LPSM bands) and the wave height derived from the wave gauges and modelled from WWIII. We finally show that analysing distant SM sources can provide precursory information of the swells impacting La Réunion Island.

2 SEISMIC DATA ANALYSES

This study uses data from the temporary deployment of 10 broad-band seismometers from the 'Rivière des Pluies' network (Fontaine *et al.* 2015). Most of the stations deployed in the northern part of the island have been operated since 2016 and are installed along two hydrological basins in La Réunion Island: the Rivière des Pluies (RIV∗) and Rivière du Mât (RMA∗). These stations were initially deployed to study the erosion and the sediment transport in the flooding rivers during cyclones (Gonzalez 2019). The station SALI installed on the western shore of the island, in the very neighbourhood of the fringing reef was deployed in February 2017 and is in appropriate location to study the swell seismic signature (Fig. 1). We also used the data recorded by the permanent seismic stations (16 broad-band seismometers) of the Observatoire Volcanologique du Piton de la Fournaise (OVPF/IPGP). The seismic data are available at the RESIF data portal (http://seismology.resif.fr) under the FDSN network code ZF and PF for the temporary and permanent stations, respectively. In this work, we analysed the microseismic noise recorded by these stations between 13 March and 5 May 2017, as oceanographic sensors (pressures gauges and ADCP) were deployed near to La Réunion Island during this period (Fig. 1).

Three methods are used to analyse the microseismic noise.

(i) To constrain the swell period T_p in the neighbourhood of the island, we calculate the seismological power spectral density (PSD) in the PM frequency band. To compute the PSD, we selected 1-hr data with 50 per cent overlap; then, each 1-hr time-series was divided into 13 segments with 75 per cent overlap between neighbouring segments, and later transformed into the time–frequency domain using the method of McNamara & Buland (2004). The obtained PSD was finally converted into decibels with respect to acceleration. To compute the daily average PSD into decibels with respect to acceleration as a function of the frequency, the *sacpsd* command from Herrmann (2013) was used.

(ii) To estimate the wave height H_s, we measured the hourly root mean square (RMS) of the microseism amplitude. The information about the wave height that hit the coastal area can be found in the PM amplitude, while the SM amplitude gives us an insight about the wave height at the swell source location, that is within the storm where it is generated. To compute the RMS, we first converted the amplitude of the microseism into displacement (μm) by removing the instrument response. Then, we divided the data into 1-hr segments and applied a Butterworth bandpass filter with corner frequencies of 0.05 and 0.10 Hz for the PM and 0.10 and 0.33 Hz for the SM. The hourly RMS of the microseism amplitude were then computed from the filtered data. Finally, we determined the correlation coefficients between the microseism amplitude and the wave height using the Pearson method (Pearson 1909). Estimating the significant wave height using seismic land station, have been successfully used before using different methods (e.g. Bromirski *et al.* 1999; Donne *et al.* 2014).

(iii) To characterize the swell direction D_p, we performed a polarization analysis using two methods: a complex polarization analysis (e.g. Vidale 1986) and a principal component analysis (e.g. Barruol *et al.* 2006; Fontaine *et al.* 2009). Both methods provided comparable values, so we only present results from the second approach. Analysing the polarization in the PM frequency band would give information regarding the swell direction before it breaks at the coastal area, while the polarization in the SM frequency band should give the information on the distant source (i.e. storm) backazimuth. Practically, we detrend and taper the three components (E–W, N–S

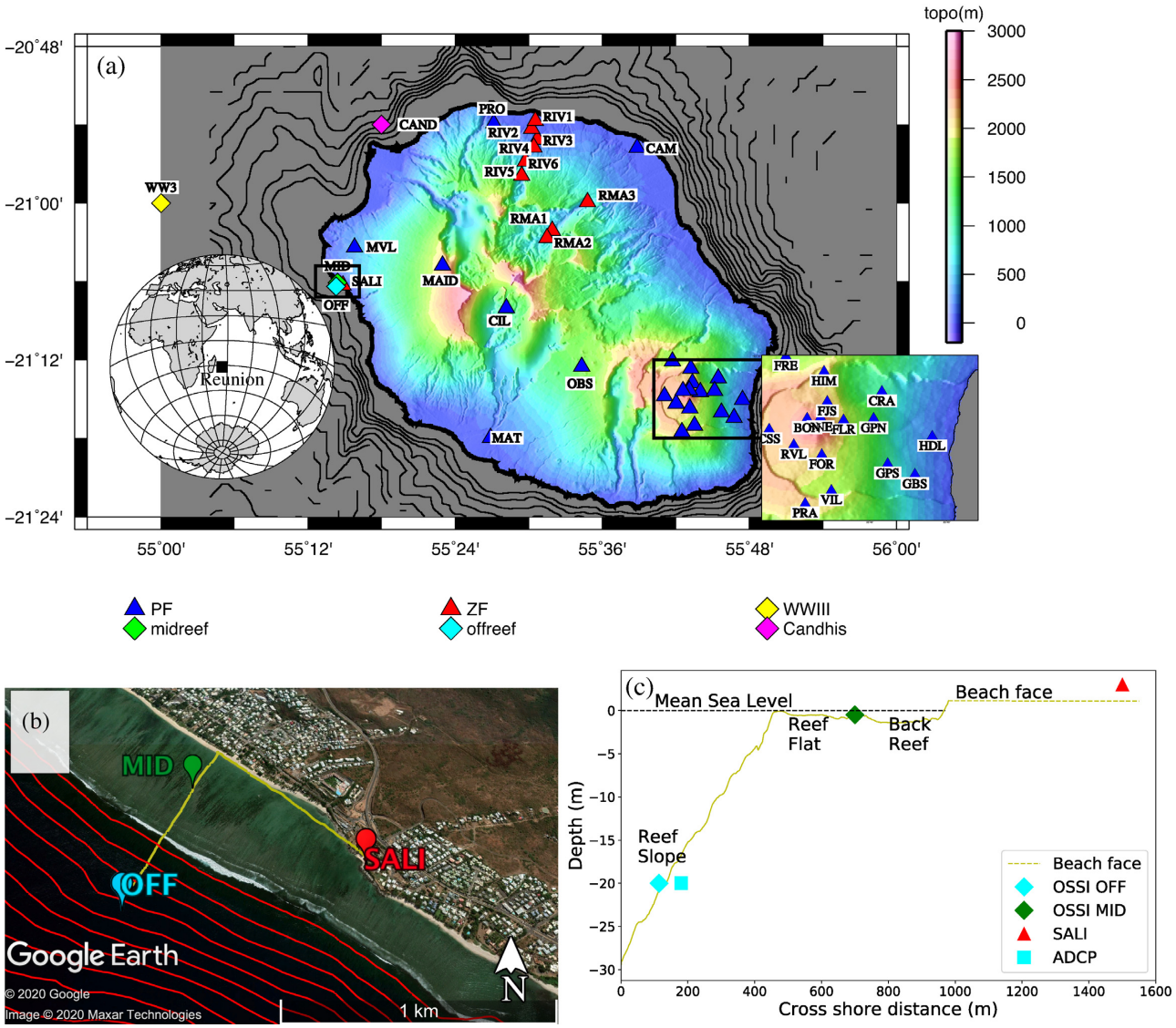

Figure 1. Location of the seismic stations and oceanographic instruments in La Réunion Island. (a) Blue and red triangles show the permanent (OVPF/IPGP, PF network) and temporary seismic network (Rivière des Pluies, ZF network). Diamonds indicate the location of the wave gauge from the Candhis network installed in Le Port harbour (magenta) and the OSSI pressure instruments offshore (cyan) and in the lagoon (green). Yellow diamond shows the location of the WW3 model node used in this study. Bathymetry data is from Délégation Ifremer océan Indien (2012) and 200 m isocontours are presented. (b) Green and cyan points indicate the pressure sensors located within the lagoon (MID, midreef) and the ADCP and pressure sensor deployed outside of the reef (OFF, offreef), respectively. SALI is the seismic station running on land close to the oceanographic instrumental transect. Yellow line shows the cross-section in subplot (c). The step of the bathymetric isocontour here is 5 m. (c) Schematic bathymetric cross-section illustrating the instrumental transect deployed from land (seismic station SALI) to the open ocean (ADCP + pressure sensor deployed on the external slope of the reef), passing through the lagoon (pressure sensor).

and vertical) of the seismic waveform before converting them into ground velocity by removing the station response. For this step, we divided the data into hourly segments. For each segment, we obtained the eigenvalues and eigenvectors from which we derived the different parameters such as $0^\circ <$ backazimuth $<360^\circ$, and the coefficient of polarization in the horizontal ($0 < CpH < 1$) and vertical ($0 < CpZ < 1$) planes (e.g. Barruol *et al.* 2006). *CpH* or *CpZ* equal to 0 indicates a circular polarization in the corresponding plane, whereas a value of 1 indicates a perfectly rectilinear polarization. These different parameters were defined in Fontaine *et al.* (2009) and allow us to characterize the full 3-D ground motion, which helps us to locate the source of the microseism and to quantify the strength of polarization.

3 OCEANIC WAVE DATA ANALYSES

Three types of oceanic wave data were used in this study, two from local, *in situ* observations, and one from numerical modelling (Fig. 1).

The first *in situ* data set was obtained from two ocean pressure sensors OSSI (Ocean Sensor Systems Inc) and from an ADCP (Nortek Aquadopp Profiler) deployed in the coastal area of La Réunion Island from 13 March to 5 May 2017 (Fig. 1). A first pressure sensor was installed inside the fringing reef at a depth of around 1 m (MID, Figs 1b and c) and a second one on the reef external slope at a depth of 20 m (OFF, Figs 1b and c). They were continuously recording the pressure induced by the sea surface variations at a sampling rate of 10 Hz. The pressure data were corrected from atmospheric mean

sea level pressure and non-hydrostatic pressure following linear wave theory (Hom-ma *et al.* 1967). The tidal components were then removed from the computed water depth using a 2nd order Butterworth lowpass filter with 6-hr cut-off frequency. Finally, a spectral analysis was performed on the detided signal to determine the wave power spectral density, from which an hourly time-series of wave height and period was extracted. To measure the wave propagation direction, the OFF pressure sensor was coupled with the ADCP, that recorded the pressure P and the two components U, V of the subsurface velocities variations at 2 Hz in burst mode of 1024 s for each hour. To compute the wave parameters, the PUV method was used, which involves a cross spectral analysis of the pressure P and the orbital velocities U and V (Pedersen 2002; Sullivan *et al.* 2006).

The second *in situ* data set was obtained from the non-directional datawell wave buoy located at the 'Rivière des Galets', a coastal station installed at a depth of 33 m, as part of the Candhis (Centre d'Archivage National de Données de Houle In Situ) network (CAND, Fig. 1). The data are freely available at the Candhis website (http://candhis.cetmef.developpement-durable.gouv.fr) from which one can retrieve hourly time-series of significant wave height (H_s) and wave peak period (T_p).

Finally, the last data set used was an hourly forecast of wave parameters issued from the 0.5° resolution global wave model forecast distributed by the Pacific Islands Ocean Observing System (PacIOOS, http://www.pacioos.hawaii.edu/waves/model-global) and configured in the School of Ocean and Earth Science and Technology (SOEST) at the University of Hawaii. These forecasts are based on the WaveWatch III model developed by the National Oceanic and Atmospheric Administration (NOAA) and National Centers for Environmental Prediction (NCEP). The hourly significant wave height (H_{sm}, with m subscript used for model), peak period (T_{pm}), peak direction for sea state (D_{pm}) and for swell component only (D_{pms}) were extracted at a node of the model located west of La Réunion Island, at latitude 21°S and longitude 55°E (point WW3, Fig. 1). The forecast parameters were used in this study because they have an hourly time step, which is similar to the observations and seismic data time steps. Also, as shown in Fig. S1, the data are comparable to the 3 hr hindcasts global wave model from IOWAGA Ifremer (Rascle & Ardhuin 2013).

4 SPECTRAL CHARACTERISTICS OF MICROSEISMS

The temporal evolution of the microseisms for station SALI derived from the PSD analysis between 13 March and 5 May 2017 is presented in Figs 2 and S2. These figures indicate that both the PM and SM have a higher level of energy during the swell events, and that SM dominates the signal.

The daily average PSDs are presented in Fig. 2(b) for the various individual swell events, selected by the white boxes on Fig. 2(a) at station SALI, occurring between 13 March and 5 May 2017. Compared to a quiet period without any austral swell (indicated by the spectrum measured on 21 March and 6 April 2017, dashed colored lines Fig. 2b), the increase of the microseismic noise during the occurrence of each swell is clearly observed in both the SM (up to 10 dB) and the PM bands (up to 30 dB) indicated by the different grey areas. Each swell event recorded at SALI has a clear signature in the PM band, the amplitude of which depends on the swell strength (Fig. 2).

The very low level of noise in the PM band in the absence of swell is shown for two different days (21 March and 6 April 2017), but the two corresponding daily spectra behave differently in the SM band. On April 6 (orange dashed line), the noise is very low in the SM band whereas on March 21 (pink dashed line), one can observe a peak of energy in the SM. This results from the fact that PM is known to be generated in shallow water, near coastal areas, due to a pressure variation at the bottom of the sea (e.g. Ardhuin *et al.* 2015) whereas the SM is sourced within storms at large distance in ocean basins. The high SM energy on March 21 likely indicates a distant storm that transmits the SM energy almost instantaneously at the seismic station, whereas the swell produced by this particular storm will reach the island only few days later. The presence of an individualized LPSM peak is observed for the April 28 event, which is the most energetic swell event visible on the spectrogram in Fig. 2. It has twice the frequency of the PM, suggesting its local origin, due to interaction of the wave reflected from the coast with the incident swell. Such a process likely generates standing waves in the near-coastal region and provides energy in the LPSM band to the ocean floor.

Fig. 2(c) presents the PSD calculated for the individual swell event of 28 April 2017, but at the various seismic stations on La Réunion Island. For this particular swell event, Fig. 2(c) indicates the presence of clear PM, LPSM and SM peaks at all island stations. The homogeneous PM amplitudes indicate that the swell energy propagates well across the island. The two distinct peaks observed at ∼0.15 Hz (LPSM) and ∼0.25 Hz (SM) suggest the presence of two source locations of secondary microseisms, with distinct dominant frequencies. Note that all of the stations recorded a comparable amount of noise during the occurrence of this swell event. The exception being for station FOR where the PM is very low compared to the other stations, likely explained by a site effect causing attenuation close to the station.

5 COMPARING SWELL DATA AND MICROSEISMS AMPLITUDES

The wave data time-series are illustrated in Figs 3 and S3 for the coastal *in situ* observations and the swell modelled from WWIII. In general, the H_{sm} modelled at site WW3 (in red Fig. 3a) displays a systematic higher amplitude compared to the actual coastal observations. Exception occurs on April 23 to 29 (Box F) during which the observed H_s offshore has the highest amplitude. This observation could be associated to the fact that the global wave model (resolution 0.5°) is relatively crude to represent coastal processes and that the waves modelled in the open ocean do not take into account refraction, diffraction and/or shoaling processes that occur at a local scale. In fact, the wave reflected from the coastal area (which produced the LPSM) attenuated rapidly and are likely to be weakly felt at the WWIII location (i.e. at latitude 21°S and longitude 55°E, WW3 node). However, despite these systematic amplitude differences, the time-series show very similar patterns with H_s peaks related to strong swell events occurring at the same time in the observations and in the models.

An important insight shown in Fig. 3(a) is the role of the reef as shore protector. The wave amplitudes are indeed reduced by a factor of ∼10 when crossing the coral reef (see the 10 times smaller right vertical axis associated to the midreef H_s measurement as the pink curve) while preserving very well the overall amplitude variations. This observation is in agreement with the tidal amplitude attenuation in the reef described by Cordier *et al.* (2012) in the same area, and indicates that the swell recorded inside the lagoon (midreef) is a very good proxy of the swell recorded further in the open ocean.

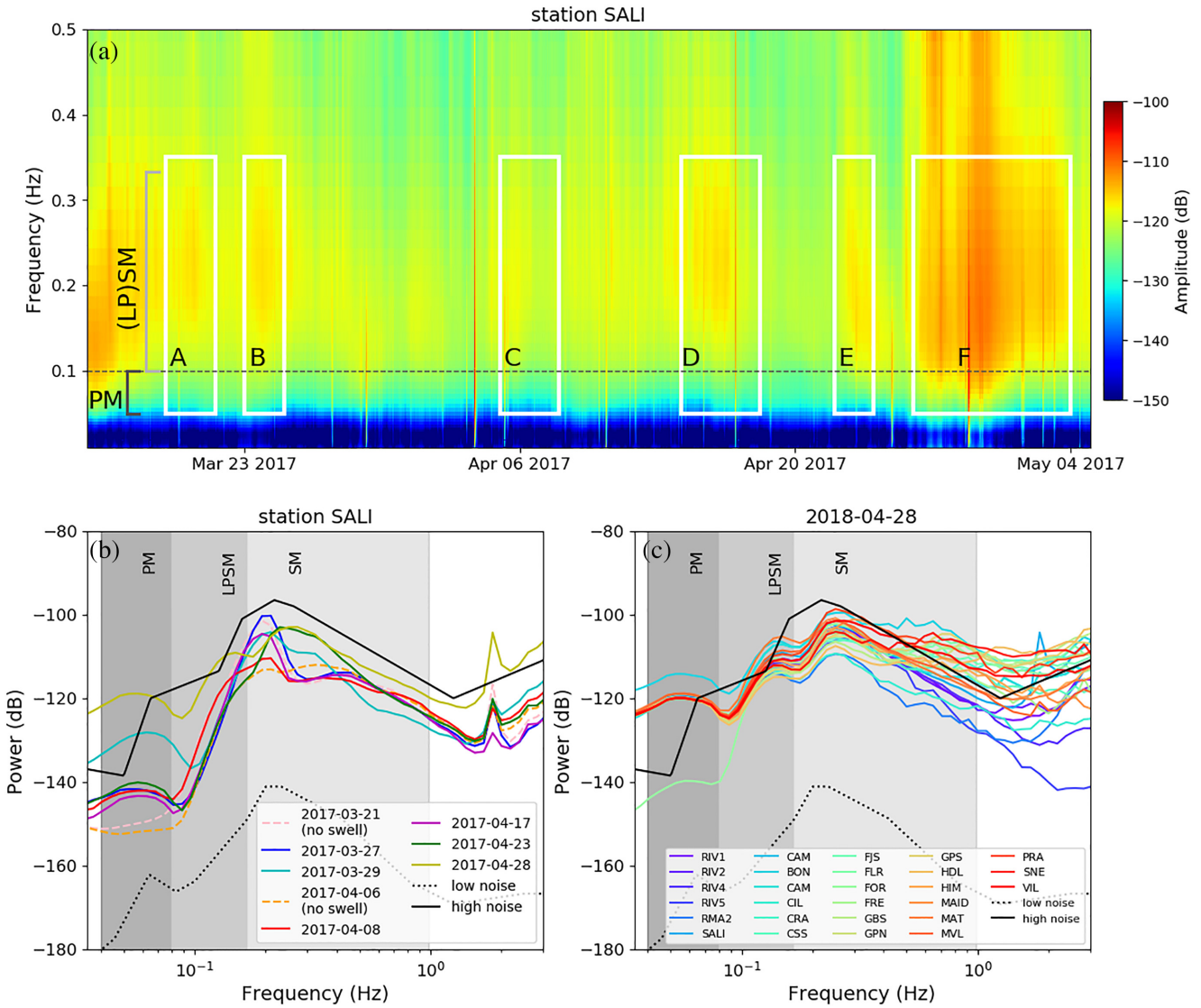

Figure 2. Power spectral density (PSD) of seismic noise converted into decibels relative to ground acceleration. (a) Spectrogram of the vertical component of seismic station SALI from 13 March to 5 May 2017. White rectangles show the swell events we analysed in this work. The 10 s (0.10 Hz) period limit between PM and SM is marked by the horizontal dashed line. (b) Daily mean PSD of data recorded at station SALI (vertical component) during the occurrence of the austral swell events occurring between 13 March and 5 May 2017. The orange and pink dashed line indicates the PSD at this station during quiet days without swell. The source of the peak at 2 Hz observed at station SALI is not identified but is likely associated with anthropogenic activity in the site neighbourhood. (c) Mean PSD of the vertical components of the different stations in La Réunion for the austral swell that occurred on 28 April 2017. For reference, the high and low noise models from Peterson (1993) are plotted in black continuous and dashed lines, respectively. Grey shadings indicate the frequency domains of PM, LPSM and SM.

Also, this shows the mechanical importance of a coral barrier to attenuate strong swell events and hence to avoid significant damage to coastal infrastructures.

Another observation from Fig. 3(a) is that the amplitudes of the swell events are generally much smaller (except the event in box C) at the 'Rivière des Galets' station (CAND) compared to those measured at the offshore coastal reef measurements (OFF). These differences likely suggest that the direction of propagation of the incident waves significantly affects how the waves impact the shore. The CAND station is indeed located 20 km north of the fringing reef area where the pressure measurements are performed. As the swells arrive from the south or the southwest, they likely experienced refraction and diffraction processes along the coast of the island, thus reducing their energy before being recorded at the CAND station. Regarding the swell event of box C, its origin of propagation is slightly more westward, thus preventing the waves to be damped due to coastal processes before arriving at CAND station. Therefore, to better monitor the Austral swell activity in La Réunion Island, it may be useful to have a buoy installed in the south.

The pattern of the PM and SM variations together with the observed H_s are presented in Figs 3(b) and (c), respectively, and also in Fig. S4. In general, for the austral swell events, the PM amplitude and the observed H_s display very similar trends (Fig. 3b). However, a clear discrepancy between the two data set are observed at the early stage of the recordings (March 13–17). During this period, the PM has a high amplitude (also the SM, Fig. 3c), while the observed H_s (in lagoon and offshore) remain low. We

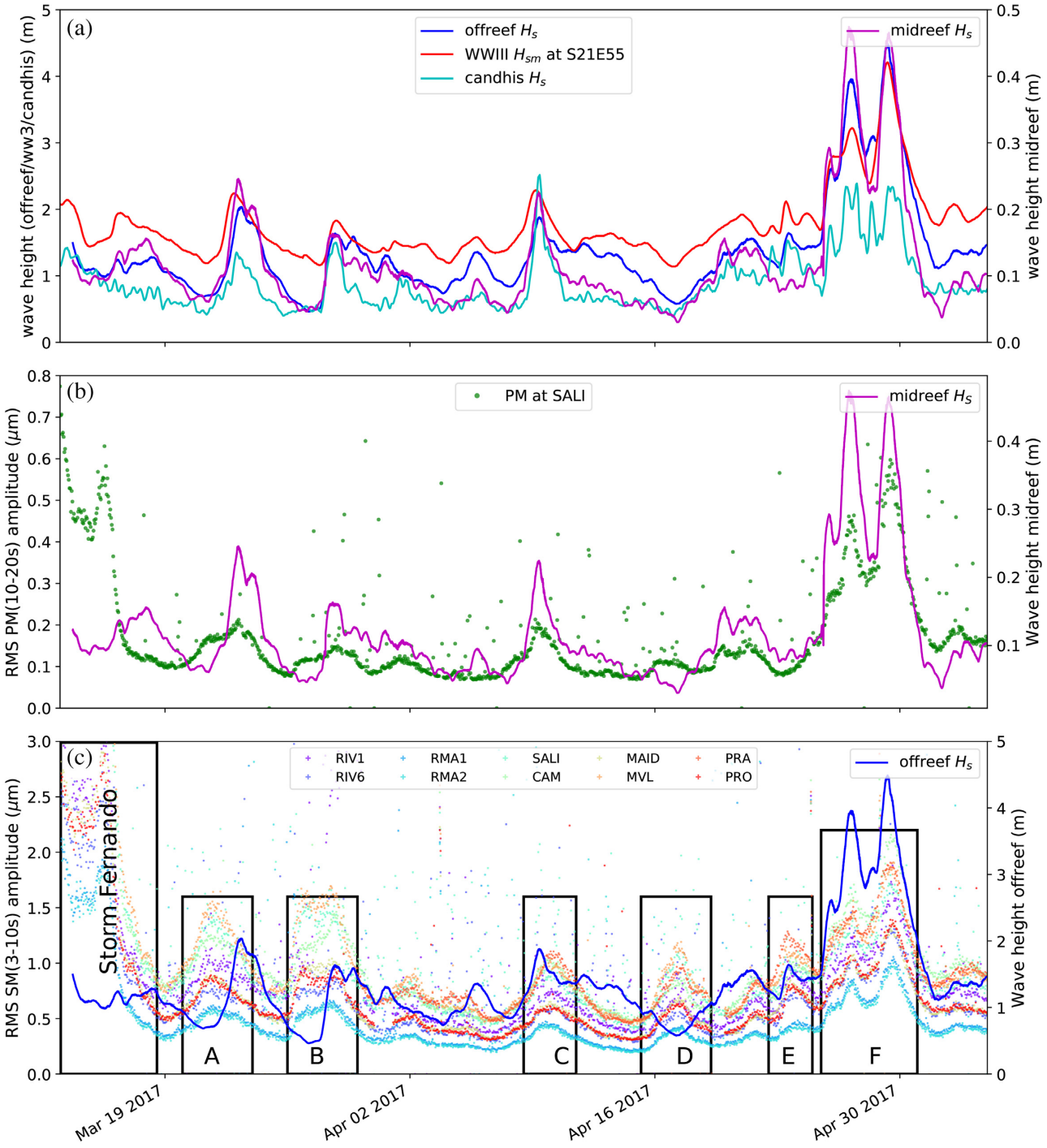

Figure 3. (a) Significant wave height H_s recorded by the different oceanographic instruments along the West coast of La Réunion from 13 March to 5 May 2017. The offreef (blue line) and the midreef (magenta line) are derived from the pressure recorded off shore and in the lagoon, respectively. The Candhis (cyan) represents the wave gauge station located in Le Port (Fig. 1). The significant wave height (H_s) from the NOAA WWIII model is shown in red and extracted at node WW3 located on Fig. 1. Note that the vertical axes are not at the same scale, for the offreef and Candhis stations (on the left) and for the midreef pressure sensor (on the right). (b) Time-series of the wave height measured in the lagoon (magenta) and primary microseisms (PM) amplitudes (green dots) from seismic station SALI, filtered in the 10–20 s period band. (c) Time-series of the offreef wave height H_s (blue line) and secondary microseisms (SM) amplitudes (seismic data filtered in the 3–10 s period band), recorded at various seismic stations on La Réunion Island (colored points). The high amplitude of the SM between March 13 and 16 is related to the ending phase of the tropical storm Fernando.

interpret these observations as induced by the tropical storm Fernando, which was active from March 6 to 15 in the SW Indian Ocean and which passed close to Réunion Island on March 12 (http://www.meteofrance.re/cyclone/saisons-passees). On March 13, the storm was already south of the island and continued escaping southward. We suggest that this storm was likely still generating SM noise close to 10 s period (observed throughout the whole Réunion island in both PM and SM bands), and a swell propagating towards the

south which did not interact with the island. Therefore, the PM recorded by the station SALI from March 13 to 16 has likely a distant origin and was not generated locally by swell interacting with the coastal slope.

Fig. 3(c) shows that the measured SM amplitudes for different seismic stations on the island have the same pattern but with slightly different amplitudes from station to station. This indicates that the SM amplitude depends on the site effect near the station. A clear split in time between the elevated values of the SM and the local observed H_s (blue curves, Figs 3c and S4) is also observed. The delay times between the two parameters are proportional to the distance between the source location and the seismic station (discussed in Section 8). The recorded PM and SM amplitudes appear to depend not only on the strength of the storm that produced the swell and the distance between the source and the seismic station but also on a local site effect. For instance, the boxes A and B have similar SM amplitudes. However, the recorded H_s corresponding to box A is relatively high compare to the H_s in box B (OFF H_s, Fig. 3c).

6 CORRELATING MICROSEISMIC AMPLITUDES WITH OBSERVED AND MODELLED WAVE HEIGHTS—TRANSFER FUNCTIONS

To determine the relationship between the local sea conditions and the microseismic noise, we correlate the RMS amplitude of the PM recorded at the seismic station SALI on land with the observed wave heights derived from the pressure sensors and the modelled wave heights from the WWIII model. Fig. 3(b) shows the PM amplitude variation together with the swell amplitude observed inside the reef (midreef H_s). This plot clearly displays good correlations between the two independent observables (except for the period when the tropical storm Fernando was still active), which we use below to determine transfer functions between microseismic noise amplitude and the wave height.

We focus here on the seismic station SALI which is the nearest to the oceanographic sensors (Fig. 1) and which has the largest RMS amplitude during the observing period. To discuss the correlation between the microseismic noise and the significant wave height, we take as an example in Fig. 4 the Austral swell occurring between 23 April and 2 May 2017 (box F, Fig. 3c). We chose this event, because of the presence of the LPSM and of the largest microseisms amplitudes. Figs 4(a) to (h) compare the observed and modelled wave height and the RMS amplitudes in the PM (upper row in Fig. 4) and in the LPSM (mid-row Fig. 4) noise bands for seismic station SALI. Microseismic noise is compared to observed H_s inside the reef (MID, midreef, Fig. 4 column I), outside the reef (OFF, offreef, Fig. 4 column II), northernmost off shore (at Candhis site, Fig. 4 column III) and to the modelled H_{sm} at node WW3 (Fig. 4 column IV). In these plots, each point represents an hourly measurement of the wave height and of the RMS microseismic noise amplitude.

As shown in Fig. 3(b), we observe a very good correlation between the wave heights and the PM amplitude during the observing period. The amplitude of the PM correlates with both the observed significant wave height derived from the OSSI wave gauges (MID, midreef and OFF, offreef) and the WWIII model, with Pearson correlation coefficient >0.95 (Figs 4a, b and d). These observations confirm that the PM relates to the local sea condition and is generated in the very coastal region, as suggested by previous studies (e.g. Barruol *et al.* 2006; Ardhuin *et al.* 2011). The correlation between the PM and the significant wave height at the northernmost CAND station is relatively lower, with Pearson coefficient correlation of 0.88 (Fig. 4c). As explained in the previous section (Section 5), this is due to the fact that the swell arriving from the SSW experienced refraction and energy reduction along its propagation path before being recorded at the Candhis wave buoy. This wave height reduction is clearly visible by comparing the swell height measured offreef (29 April 2017, Fig. 4b) and the maximum of swell amplitude of 2.4 m observed further north at Candhis (Fig. 4c).

The correlation between the amplitude of the LPSM and the significant wave heights for the different observations/model are plotted in Figs 4(e)–(h). These figures show how well the LPSM and the wave heights correlate with Pearson coefficient >0.9. These observations strongly favour that the observed LPSM is generated locally by the coastal reflected waves, which have been observed in other studies (e.g. Bromirski *et al.* 2005; Davy *et al.* 2016).

Figs 4(a)–(h) indicate that the microseism amplitudes at station SALI in both the PM and LPSM frequency bands correlate well and are linearly proportional to the significant wave heights measured in the ocean or derived from the numerical model WWIII. This suggests that these two parameters can be linked using a simple linear equation. Therefore, we used a linear regression technique to establish the transfer function between these parameters, that is between the different measured or modelled wave heights and the PM or LPSM amplitudes. In total, we determine 8 transfer functions shown in Figs 4(i)–(l). For each equation, the microseism amplitude and the wave height are in μm and in m, respectively. Note that during our linear regression, we used a thresholds values of 0.15 and 1.0 μm for the amplitude of the PM and LPSM, respectively. Therefore, the transfer functions are only valid for the microseism amplitudes above these values, which represent the recorded amplitudes when there is no swell activity.

The transfer functions between the PM noise amplitude (in green, Fig. 4) and the wave heights inside (MID, midreef) and outside (OFF, offreef) the reef, at the Candhis wave gauge and at the modelled WWIII point are $H_s = 0.95{*}A_{\mathrm{PM}} + 0.04$, $H_S = 6.78{*}A_{\mathrm{PM}} + 0.35$, $H_s = 2.77{*}A_{\mathrm{PM}} + 0.66$ and $H_s = 4.91{*}A_{\mathrm{PM}} + 0.86$, respectively. To validate these relations, we computed the wave height of the other swell events using the corresponding transfer function. Figs S5(a) to S5(d) show that the computed and the observed wave heights are comparable for the swell occurring between 21 and 25 March 2017 (box B, Fig. 3c) and Figs S5(e) to S5(h) for the swell occurring from 7 to 11 April 2017 (box C, Fig. 3c). This suggests that these equations are valid for any austral swell events and demonstrate that one can derive a reasonable estimate of the wave height from the terrestrial observation of the amplitude of the primary microseisms. This confirms that the PM amplitude is a good proxy of the coastal wave height and that a well calibrated seismic station can become a terrestrial wave gauge that can be useful in the absence of direct wave gauge in the ocean, which is the case of La Réunion Island. However, misfit between the observed and the computed wave heights are clearly observed for the 7–11 April swell event (box C, Fig. 3c), for station CAND (Fig. S5g). As discussed in Sections 4 and 5, the misfit between the two data sets may be due to the presence of additional swell recorded at the Candhis buoy only, which was strongly dissipated and did not generate PM. The presence of the swell from other source(s) is confirmed by the fact that only during these periods (April 7–11, box C, Fig. 3), Candhis station has the largest wave height amplitude.

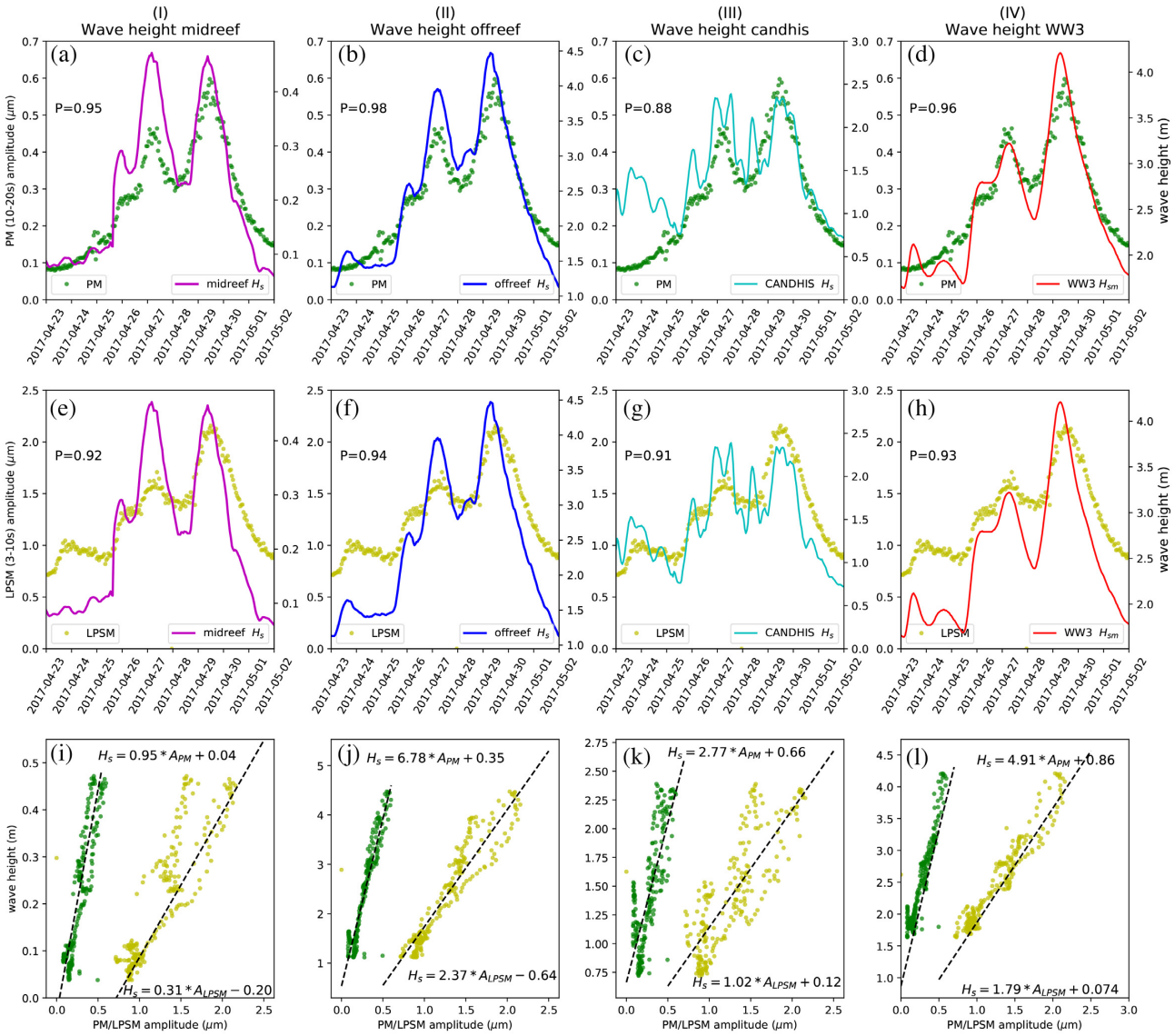

Figure 4. RMS amplitude of the PM (top, a–d) and the LPSM (middle, e–h) together with the significant wave heights H_s from observations in the ocean (I, midreef, II, offreef and III, Candhis station) and from the WWIII swell models extracted at node WW3 (IV) for the period 22 April to 2 May 2017. For each plot, the left axis represents the amplitudes of the microseisms (in μm) at station SALI and in the right axis the wave heights H_s (in m). P values indicate the Pearson coefficient for the correlations. Bottom (i–l): Transfer functions between the significant wave height H_s and the hourly RMS amplitude of the PM (green) and the LPSM (yellow). For each equation, A_{PM} and A_{LPSM} stand for primary and long-period secondary microseisms amplitude, respectively.

7 DIRECTIONS AND PERIODS OF SWELLS DEDUCED FROM SEISMIC NOISE

We present in Fig. 5(a) the hourly values of *CpH* and *CpZ* in the PM band, that is between 0.05 and 0.10 Hz, during the period 13 March and 5 May 2017 for station SALI, together with the H_s observed inside the reef (MID, midreef). This figure indicates that prior to the swell arrival, most of the *CpH* are dispersed between 0.6 and 1.0, while *CpZ* varies between 0.8 and 1.0. Both of these values clearly focus above 0.95 during the occurrence of the wave events (marked by the boxes). Strong polarization in both vertical and horizontal planes, indicates a strong linear polarization of the ground motion, similar to a horizontally propagating compressional *P* wave as described by Barruol *et al.* (2006) from near-shore seismic stations in French Polynesia islands.

The hourly measurements of the ground polarization azimuth at the coastal station SALI in the PM frequency band (0.05–0.10 Hz), together with the observed (ADCP D_p) and the modelled (WW3 D_{pm} and D_{pms} for swell) azimuths are plotted in Fig. 5(b). The azimuths determined at the seismic station from polarization analysis (PM) are likely to be generated by the interaction of waves with the local bathymetry in the coastal area, and therefore, do not provide a measure of the direction of propagation of the swell at larger distance in the open ocean. In the following, we only referred to the azimuth values in the presence of swell activities (i.e. inside the boxes). Fig. 5(b) indicates a fairly good agreement between the swell peak directions issued from the model (D_{pms}, ~N015°E±5°) and the observed peak wave direction (D_p, ~N010°E±10°). It is accepted that low frequency swells can propagate to longer distance with minimal energy loss (e.g. Ardhuin *et al.* 2009), therefore, the similarity between these two parameters (observed peak wave

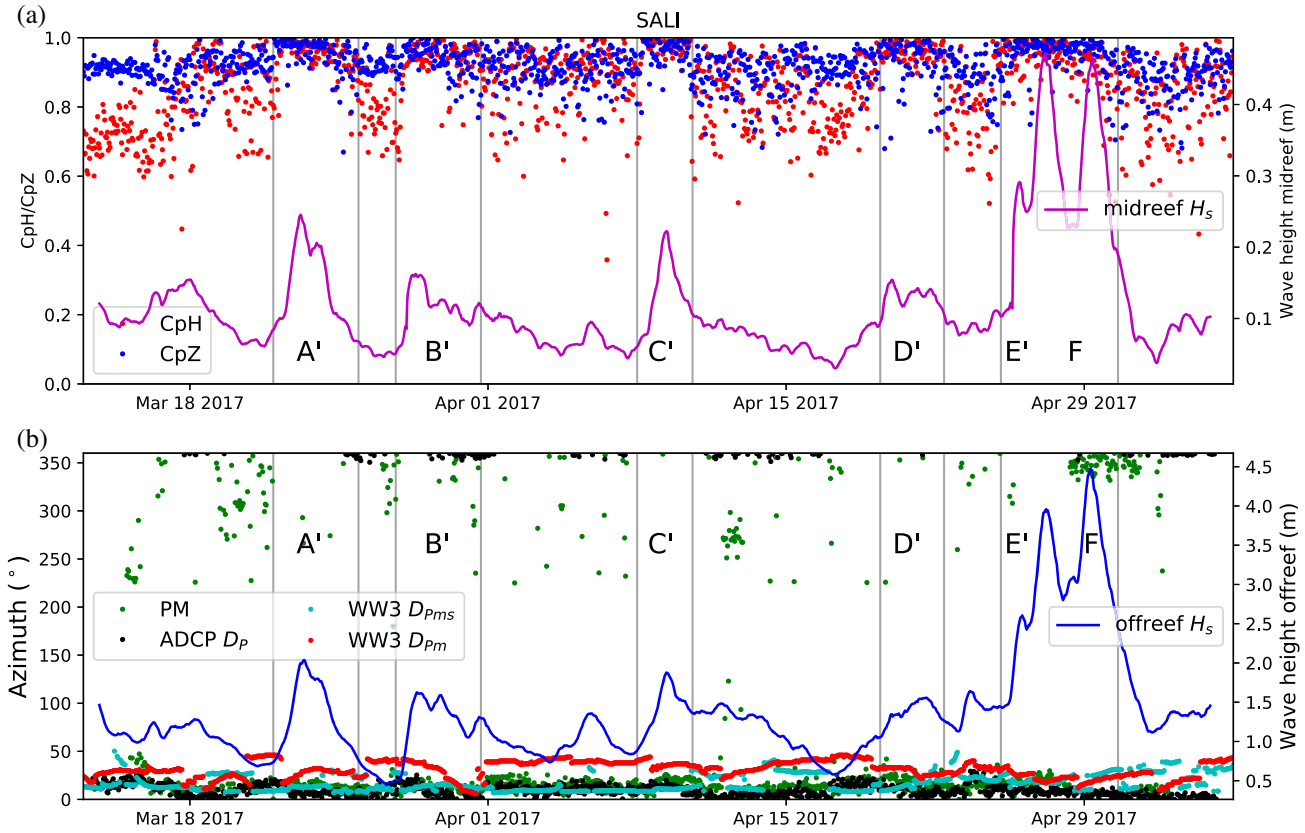

Figure 5. (a) Polarization parameters *CpH* (red dots) and *CpZ* (blue dots) measured on an hourly base in the PM, together with the wave height H_s measured in the lagoon (midreef, magenta line). Note that both polarization parameters (*CpH* and *CpZ*) are close to 1 for each swell event. (b) Plot of the polarization azimuths in the horizontal plane determined from the 3-D seismological data (green dots), and issued from oceanographic sensor ADCP (black dots) or from the WWIII model at the node WW3, swell peak wave direction (cyan dots) and wave peak direction for sea state (red dots).

direction nearshore and the modelled swells peak direction offshore) are not unexpected. The overall difference between the observed peak direction (D_p) and the modelled sea-state directions (D_{pm}) of around ∼25°E±15° is due to the fact that the observed and the modelled peak wave directions do not relate to the same physical processes, since they are in coastal and deep water environments, respectively. The observations describe waves that have already been refracted, whereas the modelled waves have not been yet refracted and also include local wind-induced waves.

The azimuths measured from the seismic polarization analysis indicate a value equal to ∼N017°E±8°. The difference (∼10°) between the observed (D_p) and the computed azimuth (PM) is likely related to the swell progressive rotation when approaching the coast. As the swell interacts with relatively shallow bathymetry (half of the wavelength), the refraction process makes it progressively rotating and to finally propagate normal to the shoreline. Here, the estimated swell wavelength is around ∼280 m (based on the modelled T_{pm} from the WWIII model), thus the waves likely start refracting at a depth of ∼140 m and continue until a depth of ∼14 m. This suggests that at the location of the ADCP (at ∼20 m depth, OFF location Fig. 1), the swell has already begun to rotate and continues its rotation before breaking at the neighbouring reef crest.

A difference between the observed (∼N005°E, *Dp*), the modelled (∼N020°E, D_{pm}) and the computed azimuths (∼N345°E) is observed for the swell in box F (i.e. April 28 to May 1). We propose that some of the reflected swells (from box E) propagated towards the south and may have interacted with the incoming waves, producing simultaneously PM and LPSM peaks. These waves hit the coastal area at the south of the SALI station, resulting in the obtained azimuth ∼N345°E. The difference between the observed swell direction (N005°, D_p) and the modelled one (N025°E, D_{pm}) may suggest that the recorded directions by offreef (OFF) station (D_p) are partly related to the reflected swell from box E. Alternatively, the ADCP (D_p) and the WWIII modelled (WW3, D_{pm}) could have recorded different direction of the incident swells, as the waves propagate in many directions from the source.

The SM azimuths for the swells in boxes A, D and E (Figs 6 a and b), for SALI station, are estimated from seismic data polarization analyses to be N345°E, N045°E and N030°E, respectively (Fig. 6c). The azimuths for these swell events and for all seismic stations on La Réunion Island are presented on the map in Fig. 7. The computed azimuths in the secondary microseismic frequency band point towards to the storm where the swell is issued (Figs 6c and 7). The observed and modelled azimuths of wave propagation (ADCP D_p, WW3 D_{pm}) are however not comparable to the azimuths of the source location (SM polarization) because the local oceanographic observations are influenced by the local coastal geometry. Consequently it is not surprising that the modelled azimuths (D_{pm}) from the WWIII model (at the point WW3 at latitude 21°S and longitude 55°E, Fig. 1 and for other nodes in the south of the Island Fig. S6) indicate the presence of the swells that have direction of propagation ∼N010–030°E and do not appear to change much despite different source locations during the observing period. Hence, the

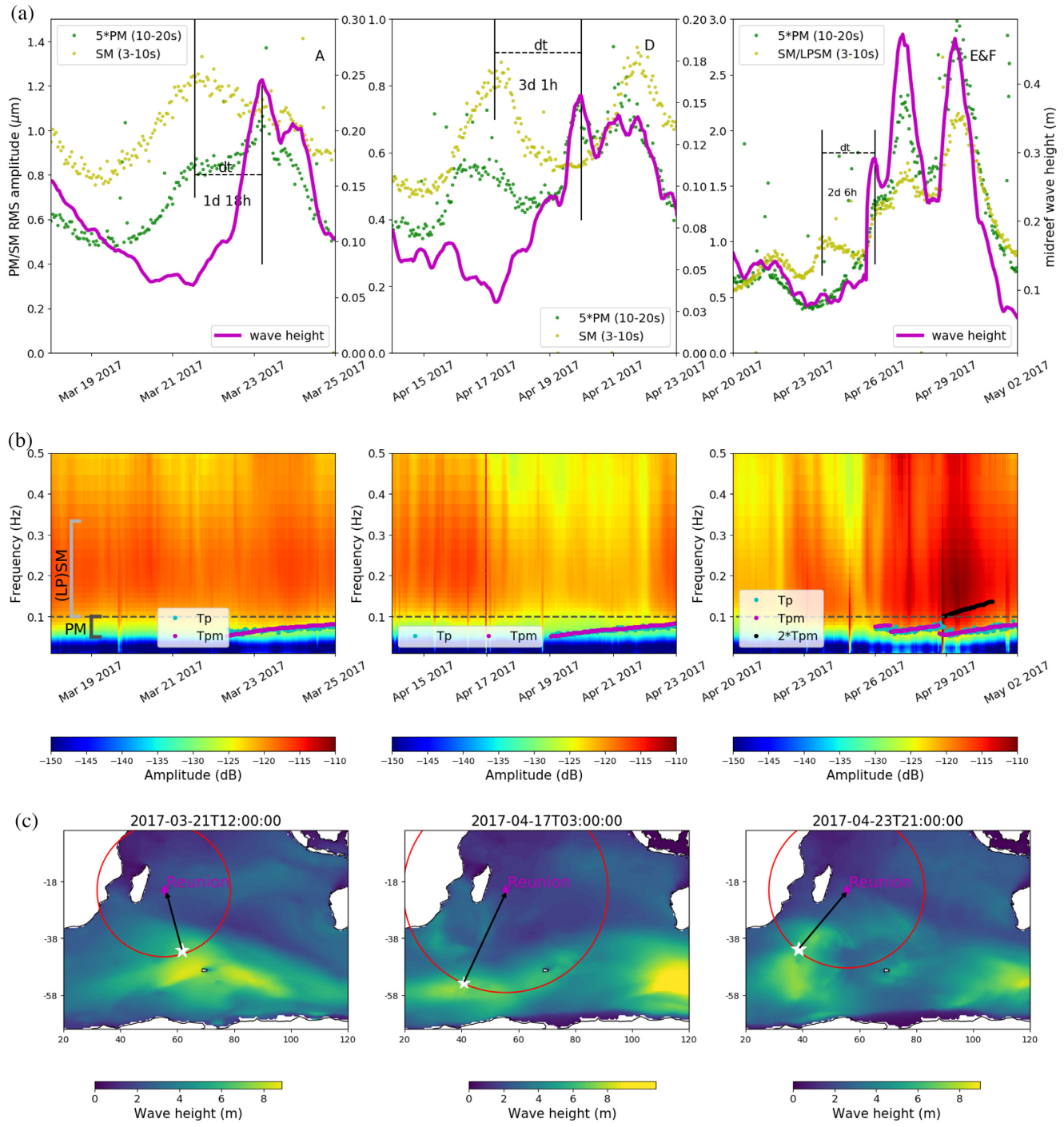

Figure 6. Examples of swell events, for station SALI. (a) Amplitude of the PM (green dots) and SM (yellow dots) and the midreef wave height (magenta line) measured in the lagoon for time interval in boxes A, D, E and F (Fig. 3c). Note that the amplitude of the PM is multiplied by a factor 5 to reach the same amplitude on the diagram as the SM. The dt shows the estimated delay time between the PM and SM. (b) Spectrograms of the vertical component of station SALI, together with the hourly swell frequency from the NOAA WWIII model (T_{pm} magenta dots) and recorded offshore (cyan dots). Black dots indicate ($2*T_{pm}$) to show the good fit with the increase of energy in the LPSM. PM and SM frequency bands are separated by the horizontal dashed line. (c) Maps of the *Hs* swell parameter issued from wave watch model WWIII on March 21 (left-hand panel), April 17 (middle panel) and April 23 (right-hand panel). Red circles show the distance between the seismic station in La Réunion Island and the SM sources. White stars indicate the approximate location of the SM source, determined from its distance and its measured incoming azimuth. Black arrows indicate the SM azimuth determined from the seismic polarization analysis.

SM azimuths cannot be related to local oceanographic observations nor modelled values. However, as we discuss in section 8, the SM azimuths (combined with its amplitude) can be used as precursory information for swell arrivals.

The frequencies relative to the swell peak period (T_{pm}) from WWIII (Fig. 6, at the point WW3, latitude 21°S and longitude 55°E in Fig. 1) and the observed peak period (T_p) by the offshore station (OFF, Fig. 1) are superposed with the microseismic spectrum in

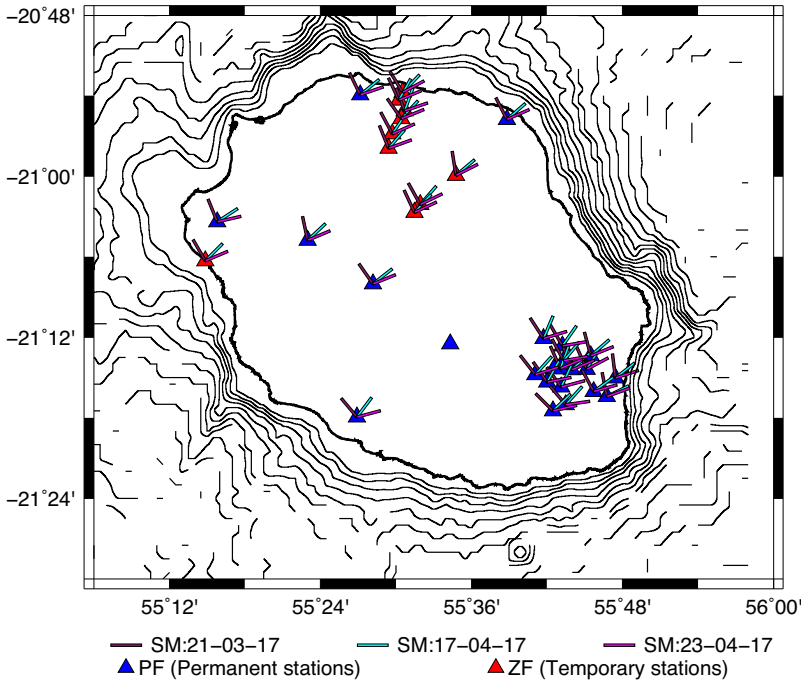

Figure 7. SM polarization azimuth measured at all seismic stations for the three swells presented in Fig. 6(c). It shows a very homogeneous pattern of polarization in this frequency band. Bathymetry isocontours are displayed by step of 200 m.

Fig. 6(b), for the swell events in boxes A, D, E and F. The observed (T_p) and modelled (T_{pm}) swells are similar and correlate well with the PM periods (Fig. 6b), suggesting that a coastal seismic station can be used to determine the swell's dominant period.

During any swell event, a clear peak in the PM frequency band between 0.05 and 0.10 Hz is observed (Fig. 2a), which corresponds to the swell frequency band. As presented in Section 4 and Figs 2(b) and (c), the presence of the long period secondary microseism (LPSM) is observed for the April 28 swell event. The spectrum in Fig. 6(b) for box F confirms the presence of such LPSM, which displays frequencies twice of the PM. We interpret such LPSM as generated by interaction between the incoming and the reflected swells, which creates standing waves near to the coastal areas. This likely induces a pressure recorded by the wave gauge and transformed into seismic waves, recorded by the seismic station, which confirms the near coastal source of the LPSM issued from swell coastal reflection, as suggested from previous works (e.g. Bromirski *et al.* 2005; Ardhuin *et al.* 2011). Bromirski *et al.* (2005) also suggested that the standing waves oscillate at twice the frequency of the incoming wave, such as the observed LPSM frequency here.

8 SM AS PRECURSORS OF STRONG SWELLS IMPACTING LA RÉUNION ISLAND

During the observing period (March 13 to May 5), SM often display a peak in amplitude preceding the actual arrival time of the H_s peak measured by the ocean sensor (Fig. 3c) and by seismic PM amplitude (Fig. 3b). In several cases, swells hit the coast (peak in the offreef *Hs*, Fig. 3c) ∼1–3 d after the SM is recorded on-land at the seismic stations (boxes A, B, D and E, Figs 3c and 6a). Exception is observed during the period April 8–13 (box C, Fig. 3), while PM arrived a few hours before the SM, likely indicating the absence of causal relationship between them. Also, for box F, the (LP)SM and PM (Fig. 6a) were recorded at the same time favouring a (LP)SM source located close to the coast. Note also the presence of high SM amplitude (also PM amplitude but with low H_s) without any H_s followed, at the beginning of the recording (March 13–18). As discussed in Section 5, we interpret that these observations are related to the final stage of the tropical storm Fernando. On March 13, the cyclone was already at the south of the island and continued to propagate southward and was likely generating a swell propagating towards the south with a dominant period of 10 s. It is therefore likely that the PM recorded by the stations SALI had a distant origin and was not generated by a local swell, explaining thus the low H_s. Some examples of swell activities (boxes A, D, E and F in Fig. 3c) are presented in the following and are illustrated in Fig. 6.

Fig. 6(a) shows in greater detail that the maximum in SM amplitude (3–10 s, in yellow) measured at station SALI arrives before the PM peak (green dots) and the wave height peak (in the midreef station, in magenta). This can be explained by the signals associated with the SM travelling as a seismic wave in the solid Earth, whereas the PM is generated by ocean waves that travel across the ocean at much slower velocity. The SM is indeed generated within the active storm by the interaction of two swells of similar periods and can be recorded almost instantaneously at a seismic station, with delay time depending on the distance between the source and the seismic station. Assuming that the surface waves that dominate the SM propagate at ∼3 km s^{-1}, they reach the station located thousands km away within few minutes. In the meantime, the swell generated by the same storm is accepted to travel at a velocity between 40 and 60 km hr^{-1} depending on the wave period. At 50 km hr^{-1} for instance, the swell may cross 1000 km of the ocean within 20 hr and for a distance of 4000 km (from La Réunion to a storm centre) will require more than 3 d of travel. This results in the observed delay times (d*t* in Fig. 6a) between the SM and the PM and/or *Hs*. The secondary microseisms can arrive simultaneously or shortly after the PM in case of near coastal sources of LPSM (box F, Fig. 6a)

or it may take few days (boxes A, B, D and E) for distant sources. Fig. 6(a) shows that for box A, the SM peak was estimated to be recorded 1 d and 18 hr before the PM peak, while for the box D, the time difference between the PM and the SM was estimated to be 3 d and 1 hr, suggesting a more distant storm. For box E, the PM peak arrived 2 d and 6 hr after the SM. The reflected swells from box E interfere with an incoming swell likely resulting in a near-coastal area source for the secondary microseisms (i.e. presence of LPSM). Thus, for box F (swell impacting La Réunion on 26 April 2017) the PM and SM (i.e. LPSM) arrived at the same time.

To estimate the SM source location, we first estimate its distance from the delay time between the PM and SM and the group velocity $U(f)$, such as $d = U(f)*dt$ (e.g. Chevrot *et al.* 2007), in which dt is the delay time (between PM and SM) and $U(f) = 3.6*g/(4*\pi*f)$, with g the gravitational acceleration (9.8 $m^2\ s^{-1}$), and f is the wave frequency that can be determined from the slope of the PM (Fig. 6b). The constant 3.6 is used to convert the velocity into km hr^{-1}. Fig. 6(c) plots the possible SM source locations on the red circles, for each of the swells indicated in boxes A, D and E. Secondly, by performing a polarization analysis, we determine the incoming direction (azimuth) of the secondary microseisms. For station SALI, we obtained an azimuth of N345°E, N030°E and N040°E for boxes A, D and E, respectively (black arrows Fig. 6c). For each event, the intersection of the azimuth of incoming noise derived from the polarization analysis with the distance circle provides a rough approximation of the SM source location (white stars). We observe that in the three cases (boxes A, D and E), the white stars are in areas of maximum H_s parameters (yellow colours), indicating the SM source location is consistent with the swell activity (WWIII model) and that the maximum noise is generated in areas of maximum wave heights within the storms. We performed a polarization analysis for all stations in Fig. 1(a) and the computed azimuth for those stations, for the three swells (boxes A, D and E), are presented in Fig. 7. This Figure shows that all the stations consistently pointed to approximately towards the same sources: N345°E (box A), N030°E (box D) and N040°E (box E).

This simple analysis indicates first the feasibility of combining the delay time between the seismologically derived PM and SM peaks and the polarization analysis to locate the SM noise source. Secondly, this analysis also demonstrates that a continuous monitoring of the SM amplitude could be used to determine precursory information of the swell height that might impact the island few days later. Unfortunately, the SM data alone are not sufficient to predict the arrival time and the amplitude of the swell to hit the island. In order to carry out the prediction of the swell, the SM information could be combined with satellite data or wave forecasting models. Knowing the areas of the maximum H_s parameters in the oceans, one can estimate the arrival time of the PM and its strength and therefore, anticipate the impact of strong swell events on the island. The use of the SM could improve the accuracy of the existing models of swell forecasting (e.g. https://www.surf-forecast.com/) around the La Réunion Island. More generally, microseismic noise analysis will not only increase the number of ocean observations but will also be very useful in validating ocean wave models worldwide (e.g. Stopa *et al.* 2019).

9 CONCLUSIONS

This study shows that terrestrial seismic stations may represent alternative tools to improve swell observations, especially in regions of limited number of oceanographic sensors and in regions where cyclones and storms may render surface buoy deployments very hazardous. We demonstrate the reliability of using the microseismic noise recorded by land seismic stations as a swell proxy. We derive the significant wave height and period parameters (H_s and T_p) together with the wave direction (D_p) from pressure gauges and Acoustic Doppler Current Profiler (ADCP), respectively. These instruments were deployed on the ocean bottom in La Réunion near-coastal areas and were operated in March–May 2017. The swell periods T_p were also retrieved from spectral analyses of the microseismic noise. Our results show that the swells measured on both sides of the reef display similar variations, but with an amplitude outside the reef about ten times higher than that inside, evidencing a strong reduction of the swell strength when crossing the reef crest, while preserving its frequency content. From the high correlation between the H_s and the primary microseisms (PM, 0.05-0.10 Hz) amplitudes (correlation coefficients >0.92), we established linear transfer functions between the two data sets that can be used for quantifying swell height from terrestrial seismic observations. A good correlation between the long-period secondary microseisms (LPSM, 0.10–0.15 Hz) and H_s is also observed in case of near-coastal source of microseisms. The secondary microseisms (SM, 0.10–0.33 Hz) that develop within the storm at several thousands of km and that propagate as seismic waves in the solid Earth arrive ∼1–3 d before the swell hits the coast of La Réunion Island, indicating that SM may represent good precursors of an extreme swell event. We estimated the location of the SM source from the polarization analysis and the delay time between the arrival times of the PM and SM, which fits well with the WWIII wave height model. We therefore propose that continuous monitoring of SM may provide good precursory information for strong swells reaching the island, that can also be used to validate the existing forecasting global model around the island.

ACKNOWLEDGEMENTS

We acknowledge the French INSU-RESIF/SISMOB instrumental pool for providing five stations deployed in the 'Rivière des Pluies' network. The data are archived at RESIF data centre (http://seismology.resif.fr) and will be available in 2022, http://dx.doi.org/10.15778/RESIF.ZF2015. We are thankful to Météo-France and the French 'Ministère de la Défense' to kindly provide access to their site in 'La Saline'. We are very grateful to the OVPF (Observatoire Volcanologique du Piton de la Fournaise) and IPGP colleagues who maintain the PF seismic stations and for the easy access and the quality of their data. We appreciate the help of E. Delcher and A. Gonzalez during the Rivière des Pluies fieldworks. E. Rindraharisaona and the oceanographic instruments and deployments were funded by the ReNovRisk project supported by the FEDER (Fond Européen de Développement Régional), Région Réunion, Etat Français CPER (Contrat de Plan Etat Région) and European Community. Thanks to the University of La Réunion and the Laboratoire Geosciences Réunion for their supports. Part of the wave data used in this study were collected during the CALHYCO research program (2015–2017) funded by Région Réunion. We thank Anya M. Reading and Laura Ermert for providing constructive comments and Editor Martin Schimmel for additional careful reading of the paper. This is IPGP contribution number 4114.

REFERENCES

Ardhuin, F., Marié, L., Rascle, N., Forget, P. & Roland, A., 2009. Observation and estimation of Lagrangian, Stokes and Eulerian currents induced by wind and waves at the sea surface, *J. Phys. Oceanogr.,* **39,** 2820–2838.

Ardhuin, F., Gualtieri, L. & Stutzmann, E., 2015. How ocean waves rock the earth: two mechanisms explain microseisms with periods 3 to 300 s, *Geophys. Res. Lett.,* **42**(3), 765–772.

Ardhuin, F., Stutzmann, E., Schimmel, M. & Mangeney, A., 2011. Ocean wave sources of seismic noise, *J. geophys. Res.,* **116**(C9), doi:10.1029/2011JC006952.

Barruol, G., Davy, C., Fontaine, F.R., Schlindwein, V. & Sigloch, K., 2016. Monitoring Austral and cyclonic swells in the "Iles Eparses"(Mozambique channel) from microseismic noise, *Acta Oecologica,* **72,** 120–128, doi:10.1016/j.actao.2015.10.015.

Barruol, G., Reymond, D., Fontaine, F.R., Hyvernaud, O., Maurer, V. & Maamaatuaiahutapu, K., 2006. Characterizing swells in the southern Pacific from seismic and infrasonic noise analyses, *Geophys. J. Int.,* **164**(3), 516–542, doi:10.1111/J.1365-246X.2006.02871.x.

Bromirski, P.D., Duennebier, F.K. & Stephen, R.A., 2005. Mid-ocean microseisms, *Geochem., Geophys., Geosys.,* **6**(4), doi:10.1029/2004GC000768.

Bromirski, P.D., Flick, R.E. & Graham, N., 1999. Ocean wave height determined from inland seismometer data: implications for investigating wave climate changes in the NE Pacific, *J. geophys. Res.,* **104**(C9), 20 753–20 766.

Bromirski, P.D., Stephen, R.A. & Gerstoft, P., 2013. Are deep-ocean-generated surface-wave microseisms observed on land?, *J. geophys. Res.,* **118**(7), 3610–3629.

Chevrot, S., Sylvander, M., Benahmed, S., Ponsolles, C., Lefevre, J. & Paradis, D., 2007. Source locations of secondary microseisms in Western Europe: evidence for both coastal and pelagic sources, *J. geophys. Res.,* **112**(B11), doi:10.1029/2007JB005059.

Cordier, E., Poizot, E. & Mear, Y., 2012. Swell impact on reef sedimentary processes: a case study of the La Réunion fringing reef, *Sedimentology,* **59**(7), 2004–2023.

Davy, C., Barruol, G., Fontaine, F.R. & Cordier, E., 2016. Analyses of extreme swell events on La Réunion Island from microseismic noise, *Geophys. J. Int.,* **207**(3), 1767–1782, doi:10.1093/gji/ggw365.

Davy, C., Barruol, G., Fontaine, F.R., Sigloch, K. & Stutzmann, E., 2014. Tracking major storms from microseismic and hydroacoustic observations on the seafloor, *Geophys. Res. Lett.,* **41**(24), 8825–8831, doi:10.1002/2014GL062319.

Davy, C., Stutzmann, E., Barruol, G., Fontaine, F.R. & Schimmel, M., 2015. Sources of secondary microseisms in the Indian ocean, *Geophys. J. Int.,* **202**(2), 1180–1189, doi:10.1093/gji/ggv221.

Délégation Ifremer océan Indien, 2012, BATHYMETRIE : MNT Hydrorun à 100m pour les 6 modèles de rang 3 autour de l'île de La Réunion, https://sextant.ifremer.fr/record/70a263ff-8095-4dcd-9d82-16badd19453d/.

Donne, S., Nicolau, M., Bean, C. & O'Neill, M., 2014. Wave height quantification using land based seismic data with grammatical evolution , in *Proceedings of the 2014 IEEE Congress on Evolutionary Computation (CEC),* pp. 2909–2916, IEEE.

Fontaine, F.R., Barruol, G., Kennett, B.L., Bokelmann, G.H.R. & Reymond, D., 2009. Upper mantle anisotropy beneath Australia and Tahiti from P-wave polarization: implications for real-time earthquake location, *J. geophys. Res.,* **114**(B3), doi:10.1029/2008JB005709.

Fontaine, F.R., Barruol, G. & Gonzalez, A., 2015. Rivière des Pluies Project, La Réunion Island, 2015-2018 2015-2018; RESIF - Réseau Sismologique et géodésique Français. http://dx. doi.org/10.15778/RESIF.ZF2015 .

Gonzalez, A., 2019, Suivi sismologique de l'impact des cyclones sur la charge de fond de la Rivière des Pluies et de la Rivière du Mât à La Réunion. *PhD thesis*, Université de La Réunion, Saint-Denis, 164 pp.

Hasselmann, K., 1963. A statistical analysis of the generation of microseisms, *Rev. Geophys.,* **1**(2), 177–210.

Herrmann, R.B., 2013. Computer programs in seismology: An evolving tool for instruction and research, *Seismol. Res. Lett.,* **84**(6), 1081–1088.

Hom-ma, M., Horikawa, K. & Komori, S., 1967. Response characteristics of underwater wave gauge, *Coast. Eng. J.,* **9**(1), 45–54.

Longuet-Higgins, M.S., 1950. A theory of the origin of microseisms, *Phil. Trans. R. Soc. Lond., A,* **243**(857), 1–35.

McNamara, D.E. & Buland, R.P., 2004. Ambient noise levels in the continental united states, *Bull. seism. Soc. Am.,* **94**(4), 1517–1527.

Obrebski, M., Ardhuin, F., Stutzmann, E. & Schimmel, M., 2012. How moderate sea states can generate loud seismic noise in the deep ocean, *Geophys. Res. Lett.,* **39**(11), doi:10.1029/2012GL051896.

Obrebski, M., Ardhuin, F., Stutzmann, E. & Schimmel, M., 2013. Detection of microseismic compressional (P) body waves aided by numerical modeling of oceanic noise sources, *J. geophys. Res.,* **118**(8), 4312–4324.

Pearson, K., 1909. On a new method of determining correlation between a measured character a, and a character b, of which only the percentage of cases wherein b exceeds (or falls short of) a given intensity is recorded for each grade of a, *Biometrika,* **7**(1/2), 96–105.

Pedersen, T., 2002. Wave measurements using the PUV method, Technical Report, Nortek Group, 15 p.

Peterson, J., 1993. Observations and modeling of seismic background noise, US Geological Survey, pp. 93–322.

Rascle, N. & Ardhuin, F., 2013. A global wave parameter database for geophysical applications. Part 2: model validation with improved source term parameterization, *Ocean Model.,* **70,** 174–188.

Stopa, J., Ardhuin, F., Stutzmann, E. & Lecocq, T., 2019. Sea state trends and variability: consistency between models, altimeters, buoys, and seismic data (1979-2016), *J. geophys. Res.,* **124**(6), 3923–3940.

Stutzmann, E., Ardhuin, F., Schimmel, M., Mangeney, A. & Patau, G., 2012. Modelling long-term seismic noise in various environments, *Geophys. J. Int.,* **191**(2), 707–722.

Sullivan, C., Warner, J., Martin, M., Lightsom, F., Voulgaris, G. & Work, P., 2006, *Wave Data Processing Toolbox Manual,* Open-File Report 2005-1211, USGS.

Vidale, J.E., 1986. Complex polarization analysis of particle motion, *Bull. seism. Soc. Am.,* **76**(5), 1393–1405.

SUPPORTING INFORMATION

Supplementary data are available at *GJI* online.

sm_Assessing_Swell_Reunion.pdf

Figure S1 Comparison between the Haiwaii/NOAA/NCEP and IFREMER wave models, (a) wave height H_s, (b) swell frequncy (period T_p) and (c) swell direction T_p .

Figure S2 Top panel: spectrograms of vertical component from 13 March to 5 May 2017 at station SALI. Rectangles show the swell that we analysed/discussed in this work (same as Fig. 2a). Bottom panel: time evolution of the PM (blue) and SM (red).

Figure S3 (a) Continuous line shows the significant wave height for the different oceanography stations (same as Fig. 3a). (b) Plot of the offreef versus midreef amplitudes showing the attenuation of the wave when crossed the reef.

Figure S4 PM (top panel) and SM (bottom panel) RMS amplitude for all seismic stations versus significant wave heights in the Lagoon (midreef) and offshore (offreef).

Figure S5 PM RMS amplitude (green dots) for SALI station versus wave heights for swells in boxes A and C (Fig. 3). The Observed wave heights for offreef (blue), midreef (magenta), Candhis (cyan) and from modelled WWIII (red) are plotted in continuous lines here. The dashed lines indicate the estimated wave heights using the transfer function from Section 6 and Fig. 4.

Figure S6 Plot of the polarization azimuths in the horizontal plane determined from the 3-D seismological data (green dots), and issued from oceanography sensor ADCP (black dots) or from the WWIII model at the different nodes S21°E55° (red dots), S21.5°E55° (cyan dots), S21.5°E55.5° (magenta dots) and S21.5°E56° (yellow dots). In general, the WWIII model at different nodes show a comparable direction.

atmosphere

MDPI

Article

Cyclone Signatures in the South-West Indian Ocean from Two Decades of Microseismic Noise

Elisa J. Rindraharisaona [1,2,*], Guilhem Barruol [1], Emmanuel Cordier [3] and Fabrice R. Fontaine [1,2,4] and Alicia Gonzalez [1,2,5]

1 Institut de Physique du Globe de Paris, Université de Paris, CNRS, 75005 Paris, France; barruol@ipgp.fr (G.B.); frfont@ipgp.fr (F.R.F.); alicia.gonzalez@univ-fcomte.fr (A.G.)
2 Laboratoire GéoSciences Réunion, Université de La Réunion, 97744 Saint Denis, France
3 Observatoire des Sciences de l'Université de La Réunion, UAR3365 (CNRS, Université de La Réunion, Météo-France), 97744 Saint Denis, France; emmanuel.cordier@univ-reunion.fr
4 Observatoire Volcanologique et Sismologique de la Martinique, Institut de Physique du Globe de Paris, 97250 Fonds Saint Denis, France
5 Chrono-Environnement, Université de Bourgogne/Franche-Comté—CNRS UMR 6249, 16 Route de Gray, CEDEX, 25030 Besançon, France
* Correspondence: elisa.rindraharisaona@univ-reunion.fr

Abstract: Tropical Cyclones (TC) represent the most destructive natural disaster affecting the islands in the South-West Indian Ocean (SWIO) each year. Monitoring ocean activity is therefore of primary importance to secure lands, infrastructures and peoples, but the little number of oceanographic instruments makes it challenging, particularly in real time. Long-term seismological records provide a way to decipher and quantify the past cyclonic activity by analyzing microseisms, seismic waves generated by the ocean activity and propagating through the solid Earth. In the present study, we analyze this microseismic noise generated by cyclones that develop in the SWIO basin between 1999 and 2020, using broadband seismic stations in La Réunion. The power spectral density (PSD), together with the root mean square (RMS) analyses of continuous seismic data recorded by the permanent Geoscope RER seismic station, indicate the intensification of the microseismic noise amplitude in proportion to the cyclone intensity. Thus, we establish a relationship between the cyclone intensity and the PSD of the Secondary Microseisms (SM) in frequency band ∼0.14 to 0.25 Hz (4 to 7 s period). The Pearson coefficient between the observed and estimated TC intensity are >0.8 in the presence of a cyclone with mean wind speeds >75 km/h and with a seismic station distance-to-storm center D < 3000 km. A polarization analysis in the time and frequency domains allows the retrieval of the backazimuth of the SM sources during isolated cyclone events and well-polarized signal, i.e., $CpH > 0.6$. We also analyzed the RMS of the Primary Microseisms (PM frequency between ∼0.05 and 0.1 Hz, i.e., for 10 to 20 s period) for cyclones passing nearby La Réunion (D < 500 km), using the available temporary and permanent broadband seismic stations. We also found high correlation coefficients (>0.8) between the PM amplitude and the local wave height issued from the global hindcast model demonstrating that the PM amplitude can be used as a robust proxy to perform a real-time wave-height monitoring in the neighboring ocean. Transfer functions are calculated for several cyclones to infer wave height from the seismic noise amplitude recorded on land. From the analysis of two decades of data, our results suggest that it is possible to quantify the past ocean activity for as long as continuous seismic archives are available, emphasizing microseismic noise as a key observable for quantifying and understanding the climate change.

Keywords: Indian Ocean; microseismic noise; wave height; tropical cyclones

Citation: Rindraharisaona, E.J.; Barruol, G.; Cordier, E.; Fontaine, F.R.; Gonzalez, A. Cyclone Signatures in the South-West Indian Ocean from Two Decades of Microseismic Noise. *Atmosphere* **2021**, *12*, 488. https://doi.org/10.3390/atmos12040488

Academic Editor: Olivier Bousquet

Received: 29 January 2021
Accepted: 5 April 2021
Published: 13 April 2021

1. Introduction

The South-West Indian Ocean (SWIO) is an active ocean basin in terms of Tropical Cyclones (TCs). Each year, during the cyclonic season (November–April), TCs cause

extensive damages due to the effects of rain, wind and waves, not only to the islands located in the SWIO such as Madagascar, La Réunion and Mauritius, but also to the continental countries along the east coast of Africa such as Mozambique (e.g., TC Idai in 2019). Coastal areas of those countries are particularly vulnerable to the waves generated by the TCs or storms, motivating the approach of better forecasting and monitoring the ocean wave activity. The little number of direct wave observations available in the SWIO is, however, a strongly limiting factor in the present or past TCs analyses. In this general frame, our objective in this paper is to explore seismic data to extract proxies of the ocean activity, providing new observables associated with TC activities in the SWIO and hence a way to quantify present or past TC through the analysis of real-time or archived time series. In our approach, this is done by analyzing the microseismic noise recorded by seismic stations on La Réunion for TCs that occurred in the past 20 years Figure 1. Such long-term microseismic noise characterization is crucial for learning more details about the ocean wave activity in the past TCs, especially in places with limited oceanographic direct observations. Recovering past information related to TCs are also of major interest to assess long-term climate changes e.g., [1].

The ocean-induced microseismic noise also called microseisms reveals the continuous interactions between the atmosphere, the ocean and the solid Earth. Microseisms correspond to continuous vibrations propagating as elastic waves in the solid Earth, induced by the oceanic gravity waves e.g., [2]. They are recorded worldwide on land and on the ocean bottom by the broadband seismic stations in the frequency range ∼0.05 to 1 Hz. There are two types of microseisms, which differ from their frequencies and origins: the Primary Microseisms (hereafter called PM, with frequency ∼0.05–0.1 Hz) and Secondary Microseisms (SM, with frequency range ∼0.1 to 1 Hz). PM have the same period as the ocean wave e.g., [3] and have been used as a wave proxy e.g., [4,5]. They are accepted to be generated in the shallow waters through the interaction between the sloping seafloor pressurization by ocean waves e.g., [6,7]. On the other hand, SM have a frequency range twice those of the ocean waves and are generated both in the shallow and deep waters. SM are accepted to be induced by non-linear interactions between ocean waves of similar periods that propagate in opposite directions generating local standing waves e.g., [2]. SM sources are primarily located in the open oceans where two distant swells may interact e.g., [8–11] and may generate standing waves allowing pressure waves to be transmitted to the ocean bottom. In addition, SM are also created in the vicinity of storm centers due to the interactions of two waves from opposite directions, which are generated by the same storm at different times e.g., [8,9,12]. SM sources have also been detected in coastal regions where the sea waves reflected at the coastal slope may interact with the incoming swell e.g., [5,8,13,14]. This last origin of SM is also known as long period secondary microseisms (LPSM).

Several works used the microseismic noise to analyze historical TCs e.g., [4,9,13,15–18]. Gualtieri et al. [17] analyzed 22 years of seismic data to estimate the relationship between the TC in the Pacific Ocean and the SM recorded by seismic stations located in the northwest of Pacific. Several studies involving the use of the microseismic data have shown the feasibility of tracking the TC using the microseismic noise e.g., [9,16,18–21]. Apart from the works of Davy et al. [4,9] and Barruol et al. [13], none of these studies focused on the cyclone activity in the SWIO.

In the current work, we make use of the microseismic noise recorded by terrestrial seismic stations on La Réunion Figure 1a to study the cyclonic activity in the SWIO since 1999. We first use the seismic station RER (network, G, Figure 1a) that operated since 1986. We investigate the continuous microseisms data recorded by the RER station and correlate them with cyclone data (position, strength, wind). To further analyze the cyclonic events that passed at distance <500 km from the island, we also investigate the relatively recent (operated since ∼2010) seismic data from permanent (network code PF, Figure 1a) and temporary networks (2015–2021, network code ZF, Figure 1a) on La Réunion. In order to retrieve wave height from seismic data, and therefore to use a seismic station as a wave

gauge, we establish relationships (or transfer functions) between the PM amplitude and significant wave height from the global wave model GOW2 [22].

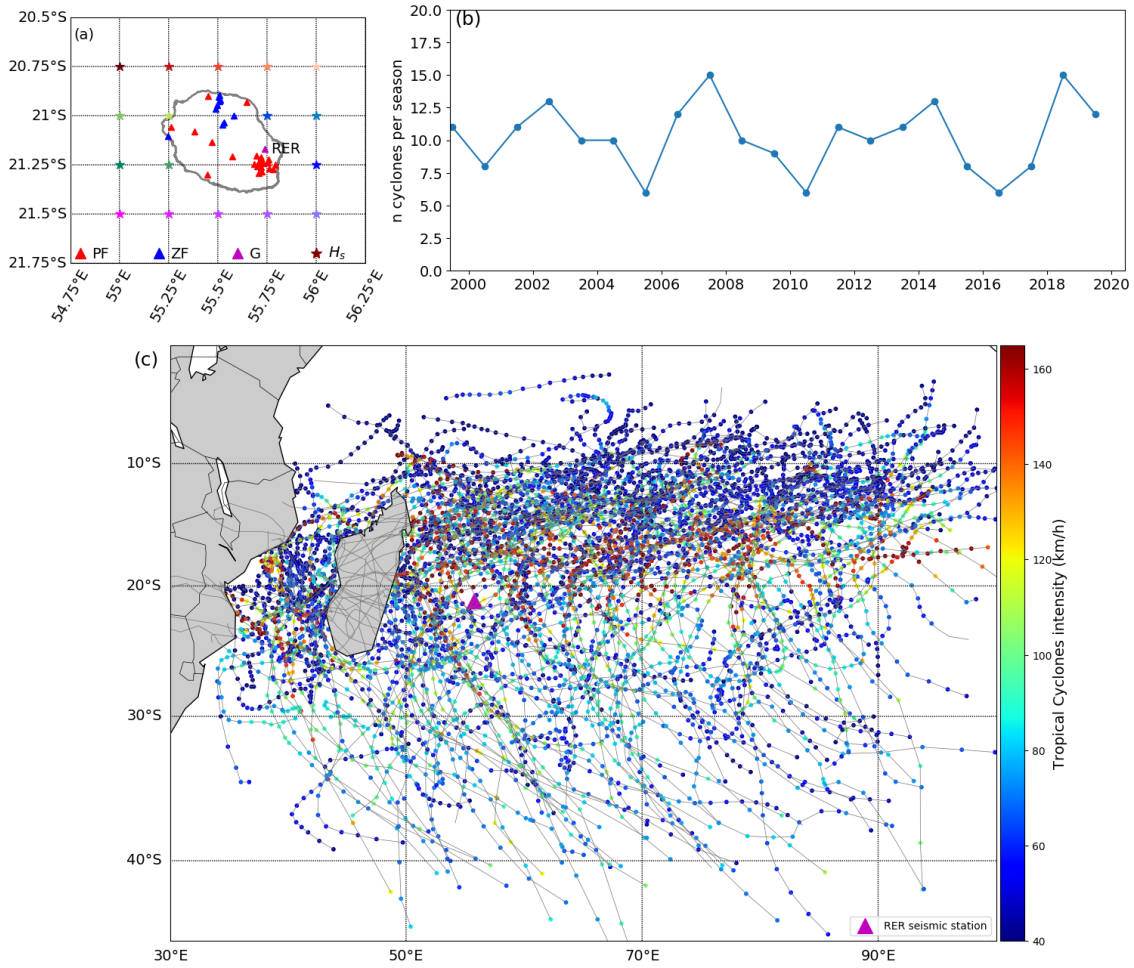

Figure 1. Geographic framework and two decades of TC in the SWIO. (**a**) Map of La Réunion showing the distribution of the terrestrial seismic stations from the OVPF-IPGP (red triangles), from the temporary experiment (blue triangles) and from the Geoscope RER station (magenta triangle). Colored stars show the offshore location of the nodes at which the significant wave heights (H_S) were extracted from GOW2 wave model Perez et al. [22]. (**b**) Number of tropical cyclones/storms, per season, between 1999 and 2020. (**c**) TC tracks (continuous grey lines) in the South-West Indian Ocean during the cyclonic period between 1999 and 2020. The color of each dot indicate the cyclone intensity on a 6-hours basis. The magenta triangle marks the RER seismic station.

2. Materials and Methods

2.1. Tropical Cyclones and Microseismic Noise Data

Cyclones develop in the SWIO each year between October and April. In this work, the word cyclone is used in a broad sense to refer to a tropical cyclone or to a tropical storm. We analyzed seismic signatures of cyclones that occurred in the SWIO between 1999 and 2020 (Figure 1b,c). The number of cyclones for each season is plotted in Figure 1a. The cyclonic seasons 2005–2006, 2010–2011, 2016–2017 and 2007–2008, 2018–2019 have the minimum (6) and maximum (16) number of cyclones, respectively. The information about the cyclone in the SWIO is freely available from the Météo France (MF) website (http://www.meteo.fr/temps/domtom/La_Reunion/webcmrs9.0/anglais/index.html, accessed on 12 April 2021). Each cyclone is characterized by the intensity and pressure at the storm center, along with its geographical position. This information is made available on a 6 h basis during the cyclone lifespan. The intensity of the cyclone in this work is defined by the average of the maximum wind (km/h, see Table S1). More details about cyclone names

and classifications can be found in Leroux et al. [23] and in the MF database. Figure 1c indicates that typical cyclones start at latitude ∼10° S, move SW, reinforce down to latitude of 15 to 20° S and then turn toward the SE to finally decrease in intensity. Strong cyclones form usually in the north, north-east and east of La Réunion. Individual information (i.e., track and intensity) for all the cyclones occurring between 1999 and 2020 are plotted in Figure 1c.

To assess the long-term cyclone climatology, we used seismic station RER to estimate the relationship between the cyclone activity and the microseismic noise. This station is in the south-eastern part of La Réunion and has been operating since 1986 (Figure 1a). RER has been instrumented with a broadband seismic sensor, with a sampling rate of 20 Hz since 1990. However, only since July 1999, the East (BHE) North (BHN) and Vertical (BHZ) components were continuously archived. Thus, to have a uniform data set, we focus our analysis on the data between 1999 and 2020.

To focus on some particular cyclones passing near La Réunion (Section 3.2), we also used data recorded by the seismic stations from the permanent network managed by the Observatoire Volcanologique du Piton de la Fournaise (code PF, OVPF/IPGP, 16 broadband seismometers, shown in red triangles in Figure 1a) and from the temporary network of the "Rivière des Pluies" experiment (code ZF, [24], 10 broadband seismometers plotted in blue triangles in Figure 1a). The corresponding seismic data are available at the French RESIF data portal center (http://seismology.resif.fr, accessed on 12 April 2021.) under their respective FDSN (Federation of Digital Sesimograph Networks) network codes. These stations are equipped with broadband seismometers with sampling rate of 100 Hz, with three components HHE (East), HHN (North) and HHZ (vertical).

2.2. Seismic Data Analyses

To estimate the relationship between the cyclone activity and the microseismic noise, we computed the continuous Power Spectral Density (PSD) of the vertical component (BHZ) of the seismic station RER. We first selected 1-h long seismic data with 50% overlap. Then each 1-h time series was divided into 13 segments with 75% overlap with neighboring segments. After that, each segment was transformed into the time-frequency domain using the method of McNamara and Buland [25]. The obtained PSD was converted into decibel (dB) with respect to acceleration (i.e., with respect to $m^2/s^2/Hz$). Finally, we averaged data every 6-h to have a similar time step as the cyclone intensity data, i.e., the average of the maximum wind. During our computation, we used SM with frequency ranges 0.14 to 0.25 Hz (period 4–7 s, short period SM), as it has proven to correlate well with a cyclone e.g., [16–18].

To evaluate the backazimuth (BAZ) of the incoming noise, we performed a polarization analysis on successive one hour-long seismic time series. The three components of the seismograms (BHE/HHE, BHN/HHN, BHZ/HHZ) were detrended and decimated to 1 Hz sampling rate before converting them into ground velocity by removing the station response. We obtained different parameters such as CpH and CpZ which correspond to the degree of polarization in the horizontal and vertical plane, respectively, and the azimuth of the ellipse long axis (between 0 and 360°). These different parameters allow us to characterize the full 3-D ground motion. A CpH of 1 corresponds to a perfectly polarized signal in the corresponding plane (i.e., a linear ground motion), while a value of 0 characterizes a random (circular) ground motion. More details about these parameters are presented in Section S1 and can be found in previous works [5,7,26,27]. In this work, we focused our attention to the azimuth of significantly polarized signal corresponding to $CpH > 0.6$.

To quantify the relationship between the PM and the significant wave height H_S through a transfer function, we calculate the hourly Root Mean Square (RMS) amplitude of the microseismic noise on the vertical component (HHZ) of the seismograph. The vertical component was used as it is generally less affected by artefacts and has relatively larger amplitudes than the horizontal components in this frequency band e.g., [4,7]. We first

converted the time series into displacement (units of μm) by removing the instrumental response and divided the data into 1-hour segments. We then filtered the data using a 2nd order Butterworth bandpass filter, with corner frequencies at 0.05 and 0.1 Hz (periods ∼10 and 20 s) and computed the RMS. After that, we calculated the Pearson correlation coefficient (P_{coef}) between the PM amplitude and the significant wave height H_S, extracted from the global wave hindcast model GOW2 developed by Perez et al. [22], at 17 selected nodes locations around the island Figure 1a. Finally, we computed transfer functions between PM (observed seismic) and H_S (modeled ocean waves) amplitudes at 3 nodes located close to the coastal area (55.25° E 21.00° S, 55.25° E 21.50° S and 55.75° E 21.00° S) and 2 other nodes that have the highest Pearson coefficients (55.00° E 20.75° S and 55.50° E 20.75° S). In total, we obtain 5 transfer functions corresponding to each nodal point (details in Section 3.2.3).

3. Results and Discussion

3.1. Analysis of SWIO Cyclones in the SM Frequency Band Using RER Seismic Station

3.1.1. Spectral Characteristics of Microseisms in the Presence of Tropical Cyclones

The cyclone tracks from the 2018–2019 season are plotted in Figure 2a. The choice of this season was driven by the maximum number of cyclones (Figure 1b). Figures 2b–d show the intensification of the microseismic noise in the presence of a cyclone. The temporal PSD evolution of the other cyclonic seasons are presented in Figures S1–S4. In Figure 2b, we plot the PSD at station RER (expressed in dB with respect to acceleration) calculated in the presence (continuous colored lines) and absence (bold black dashed-dotted line) of cyclone activity, during the cyclonic season 2018–2019. We computed the daily average PSD, using the *sacpsd* command [28], during the cyclone lifespan, for the days that have a maximum wind intensity (V_{TC}) $\geq$ 90 km/h (i.e., when it reaches the severe tropical storm stage, see Table S1). Then, we calculated the median of the obtained PSD for each cyclone and presented them as continuous colored lines in Figure 2b. Each spectrum represents a cyclone, the track of which is plotted on the map Figure 2a using the same color code. The black dashed-dotted line indicates the median of daily average during the quiet period in 2019, i.e., in the absence of cyclone or austral swell activities. Austral swells are indeed generated by strong winds and long-distance fetches, in general by depressions moving around Antarctica, which affected La Réunion mainly in winter season, between April and October e.g., [5,29]. Some of them occurring in September and October 2018 are indicated by the pink boxes in Figure 2c. During cyclones, earthquake signatures were removed from the data to avoid the alteration of the PSD. However, in absence of cyclone, the large-amplitude signal generated by an earthquake lasts generally less than a minute and has little to none effect on the computed PSD. Figure 2b shows increase of the PSD amplitude in the presence of a cyclone, in the range ∼5 to 35 dB, depending on the intensity and the location of the storm center. Despite the absence of direct impact of any cyclone on La Réunion during the selected cyclonic season 2018–2019, the PM peaks are also well expressed in the various spectra, indicating the effect of distant swell generated within the cyclone and impacting coastal areas of the island. The amplitude increase of the PM can reach 15 dB in case of Alcide (shown in blue color).

To evaluate the temporal evolution of the cyclone signature, we computed the continuous PSD of the microseisms. As an example, the 2018–2019 cyclonic season shown in Figure 2c,d indicates that cyclones developing at distance as far as ∼3000 km induce clear noise intensification in the SM frequency band. Occasional transient noises observed on the spectra result from either earthquakes or glitches in the data. The presence of high level of energy in the SM frequency band, in absence of a cyclone, is generally related to the continuous storm activity around Antarctica that are well recorded by the seismic station on La Réunion [29]. Such episodes occur mostly during austral winters (April to October). To avoid overcrowded of the Figure 2c, we only marked the austral swell in October, which are within the magenta boxes (Figure 2c).

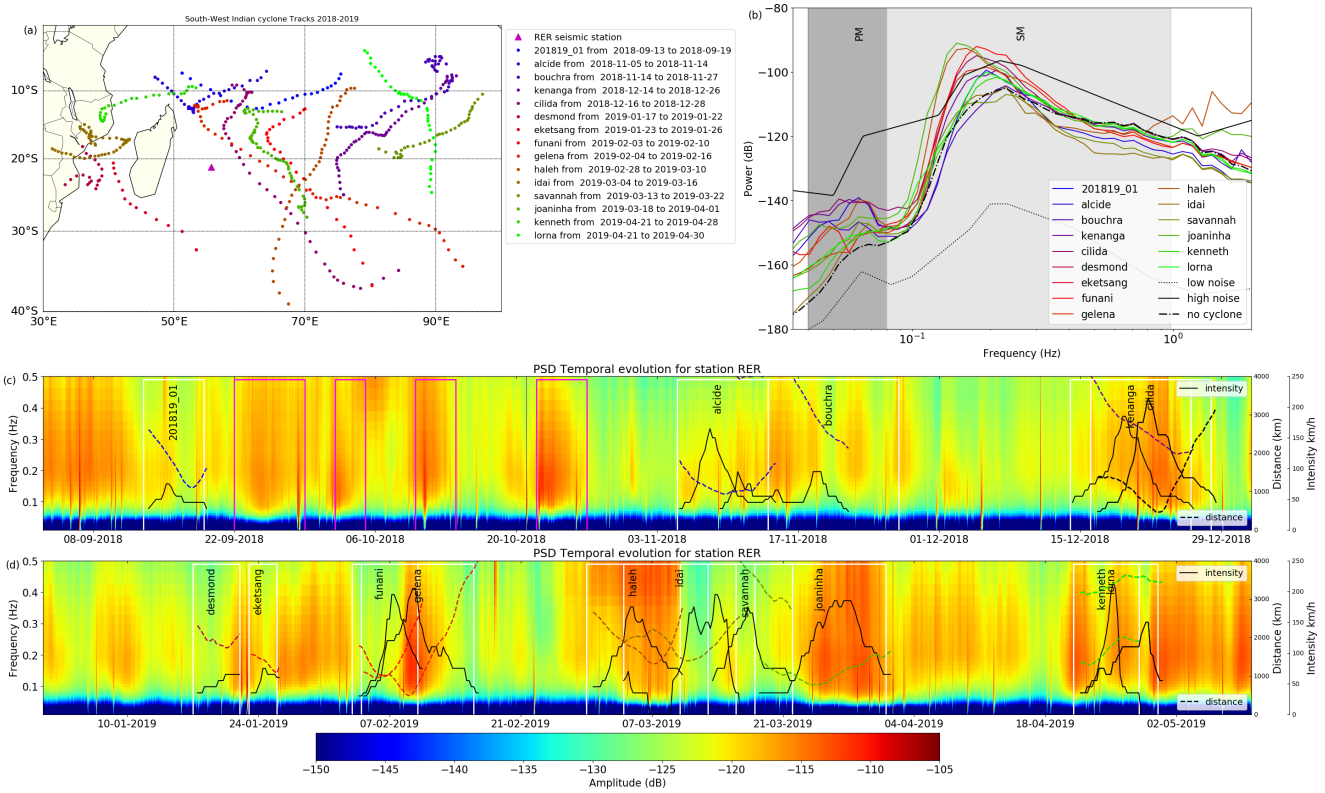

Figure 2. Spectral content of the RER seismic data. (**a**) Cyclone tracks in the South-West of the Indian ocean during the cyclonic season 2018–2019. Cyclone information is freely available at the Météo France (MF) website (http://www.meteo.fr/temps/domtom/La_Reunion/webcmrs9.0/anglais/index.html). (**b**) Average PSD of data recorded by station RER during each cyclone of the season 2018–2019. For each event, the median (continuous colored lines) of the daily average for the days with an intensity higher than 90 km/h are computed. The black dotted-dashed line indicates the PSD at RER for days without cyclone activity (nor austral swell activity) in 2019. For reference, the high and low noise models [30] are plotted in black continuous and dashed lines, respectively. Grey shadings indicate the frequency domains of PM and SM (in dark and light, respectively). (**c**,**d**) Spectrograms of microseismic noise of the RER station vertical component for the cyclonic season 2018–2019, up to 0.5 Hz (linear scale). Each cyclone is indicated by a white box. Black lines show the cyclone's intensity (right axis, showing the wind velocity in km/h from MF) and colored dashed lines show the distance between the storm center and RER station. Austral swell events are indicated by the pink boxes.

Figure 2 shows that the microseismic noise generated by cyclones in the Mozambique Channel (Desmond, Eketsang, Idai) is characterized by a weak amplitude at RER. As an example, Idai formed on 4 March 2019 as a tropical depression in the Mozambique Channel and ended on 16 March 2019. Idai was categorized as a TC from March 10 to 15, characterized by very powerful winds ($130 < V_{TC}$ (km/h) < 195) and a storm center in the Mozambique Channel. Surprisingly, at RER seismic station, Idai displays a low amplitude PSD comparable to the days without wave activity (Figure 2b). Idai was almost simultaneously active with Haleh (on March 4 to 10) and Savannah (on March 13 to 16), which makes them difficult to isolate but from March 10 to 13 (TC stage), Figure 2d shows a clear weak signal despite Idai was at its maximum power. Interestingly, TC Desmond and Eketsang, both also developing in the Mozambique Channel, are characterized by similarly weak signals at RER during their lifespans. A first hypothesis is that the weak SM amplitude observed in the Mozambique Channel may be related to a fetch of limited extent, which (and wind speed) controlled the size of significant wave height. The shape, size and location of the Mozambique Channel between the two continental masses of Africa and Madagascar could indeed represent limiting factors for long fetches development. A second, non-exclusive, factor for explaining the absence of SM recorded at RER during Idai is the absence of SM sources in this TC and all other TC travelling in the Mozambique Chan-

nel. The complex geometry of the channel could explain the difficulty in generating waves propagating in the opposite directions with the same period that could create standing waves and therefore SM sources. A third hypothesis could be related to a bathymetry effect and is also found from SM source modeling in this area e.g., [8] and polarization analysis e.g., [29], according that the SM amplitude is proportional to the square of the ocean wave height e.g., [2] and induced by pressure fluctuation e.g., [8]. A model of the power spectral density of the equivalent surface pressure ($fp2s$) in the Mozambique Channel could have lent evidence of the lack of SM source there. However, the $fp2s$ parameter is not available on the GOW2 wave model that we used in the current study.

3.1.2. Correlation between Secondary Microseisms and Cyclone Distance

Visual comparison between Figure 3a (Cyclone intensity) and Figure 3b (SM PSD amplitude) suggests that the strength of the microseismic noise depends at first on the distance between the storm center and the seismic station. In the area surrounding Réunion Island, even the relatively weak cyclones ($V_{TC} < 100$ km/h), sign with PSD higher than -115.0 dB. In contrast, between the longitude 70° E and 90° E, many powerful cyclones ($V_{TC} > 100$ km/h) occurred, but are associated with a low level of the PSD at RER (~ -118.0 dB). Figure 3 indicates that a seismic station starts to record a weak but clear SM from a strong TC at a distance ~4000 km, and that the SM intensified inversely proportional to distance. For each cyclone occurring from 1999 to 2020, we estimated the relation between cyclone distance and the intensification of the SM on the PSD. The obtained equations are plotted in grey lines in Figure 4a. These plots indicate logarithmic SM decays with respect to distance, such that $PSD_{SM} = A \times log(D) + B$, in which PSD_{SM} is the strength of the SM, D is the distance between the storm center and the seismic station, and A and B two constants depending on the cyclone intensity and how fast it evolves from tropical disturbance to tropical cyclone/storm (see Table S1, for cyclone classification). Average values of A and B were computed from the different cyclones, with their respective standard deviations. We first determined the standard deviation from all data and removed the outlier cyclones (representing 6% of our data), which had a variance of more than three times the standard deviation. After removing the outliers, we recomputed the averages and obtained values equal to -3.9 ± 1.5 and -89.5 ± 9 (red curve in Figure 4a) for the parameters A and B, respectively.

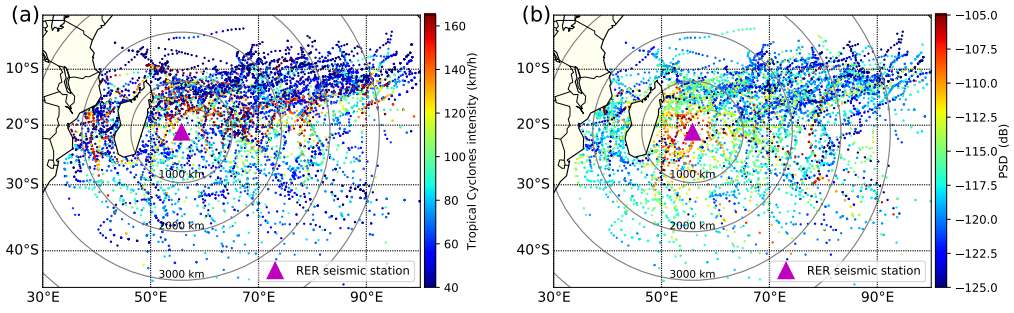

Figure 3. Cyclone powers and SM intensities. (**a**) Six hours average of cyclone intensity (i.e., maximum mean wind at the cyclone center, V_{TC}) in the SWIO during the cyclonic seasons between 1999 and 2020. Colored bar shows the cyclone intensity (colored dots), ranging between 40 km/h (TD) and 165 km/h (ITC). The magenta triangle indicates the RER seismic station used in this study. (**b**) Six hours average of the SM PSD in frequency bands between 0.14 and 0.25 Hz (periods ~4–7 s) recorded at station RER and plotted at the cyclone center, the color bar indicates the amplitude of the PSD ranging between −125 dB (blue) and −105 dB (red).

We also estimated the relationship between the distance and the strength of the PSD in the SM frequency band, using all cyclones occurring between 1999 and 2020 and with tracks geolocalized within latitudes 5° S–40° S and longitudes 50° E–90° E Figure 4a. We excluded cyclones developing in the Mozambique Channel as the recorded

SM appear to be always weaker for a given distance (and for different cyclone strengths, see Section 3.1.1). We derived the following relation: $PSD_{SM} = -4.41 \times log(D) - 85.68$ (green curve in Figure 4a). This equation confirms the direct influence of the distance of the storm center on the recorded SM as already proposed by Davy et al. [9].

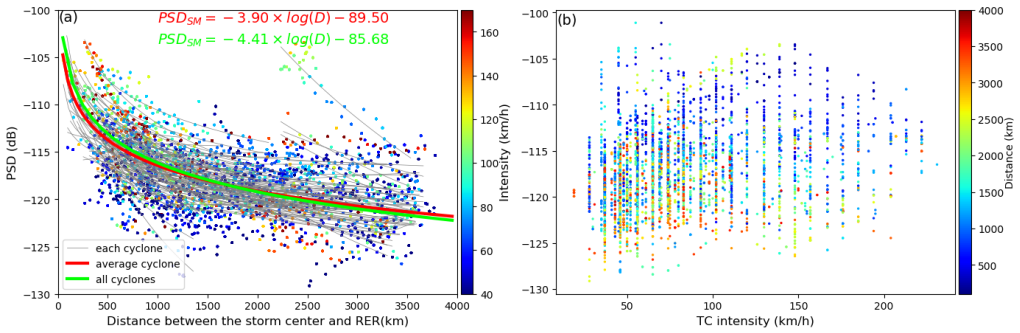

Figure 4. Seismic energy vs cyclone distance and intensity. (**a**) Relation between the SM PSD (periods ∼4–7 s) recorded at station RER and the distance to the storm center. The intensity of the TCs is plotted on a 6-hour basis (same as Figure 3) with the color bar scale indicating the average wind speed. Grey lines represent the transfer function between the PSD and each individual cyclone distance. Red line shows the average of the grey lines. Green line indicates the transfer function using all the cyclones. (**b**) Correlation between the SM PSD and the TC intensity. Color bar scale indicates the distance.

3.1.3. Relation between Secondary Microseisms and Cyclone Intensity

Figures 3 and 4 show that the intensification of the SM is not only depending on the distance from the storm center, but also on the cyclone intensity. Despite a widespread in the measurements, Figure 4a shows a general decrease of the recorded energy at the station RER as the cyclone is at larger distance (as discussed in Section 3.1.2). Alternatively, Figure 4b displays a general increase of the seismic noise amplitude as the cyclone is stronger. Distant cyclones (red colors Figure 4b) display generally low PSD whereas cyclone developing at short distance (in blue) are generally characterized by higher energies. Exceptions are observed while the cyclone has a $V_{TC} < 50$ km/h. In such a case, despite the small distance station-to-storm center <500 km, the recorded SM are weak (Figure 4b).

Figure 5 presents the relationship between the cyclone intensity and the SM PSD at different geographical locations. We divided the cyclone data into three groups according to their distance to RER and their locations in the SWIO basin. The latitude and longitude boundaries for each group are indicated on the corresponding plot in Figure 5 (left panels), presented on the maps (right panels) and listed in Table 1. To determine the relationship between the cyclone intensity and the microseismic noise, we correlate the cyclone intensity through the proxy of wind velocity, V_{TC}, with the SM PSD (PSD_{SM}). Statistically, the distribution of the V_{TC} can be approximated with a gamma distribution with relatively high standard deviations (Figure 5, top right panel). As suggested by Agresti [31], it is more accurate to apply the generalized linear model (GLM) technique to determine the relationship between the two parameters. We therefore applied such GLM technique to estimate the transfer function between the V_{TC} and PSD_{SM}, for the cyclone intensity and microseismic noise data between 1999 and 2017. Similar technique was successfully used in Gualtieri et al. [17] to assess the relationship between the cyclone intensity and the spectral characteristic of the microseismic ambient noise in the northwest of the Pacific Ocean. Please note that if two cyclones overlap or if a cyclone occurs simultaneously with an austral swell, the computed PSD_{SM} represents their cumulative effects and may bias the transfer function.

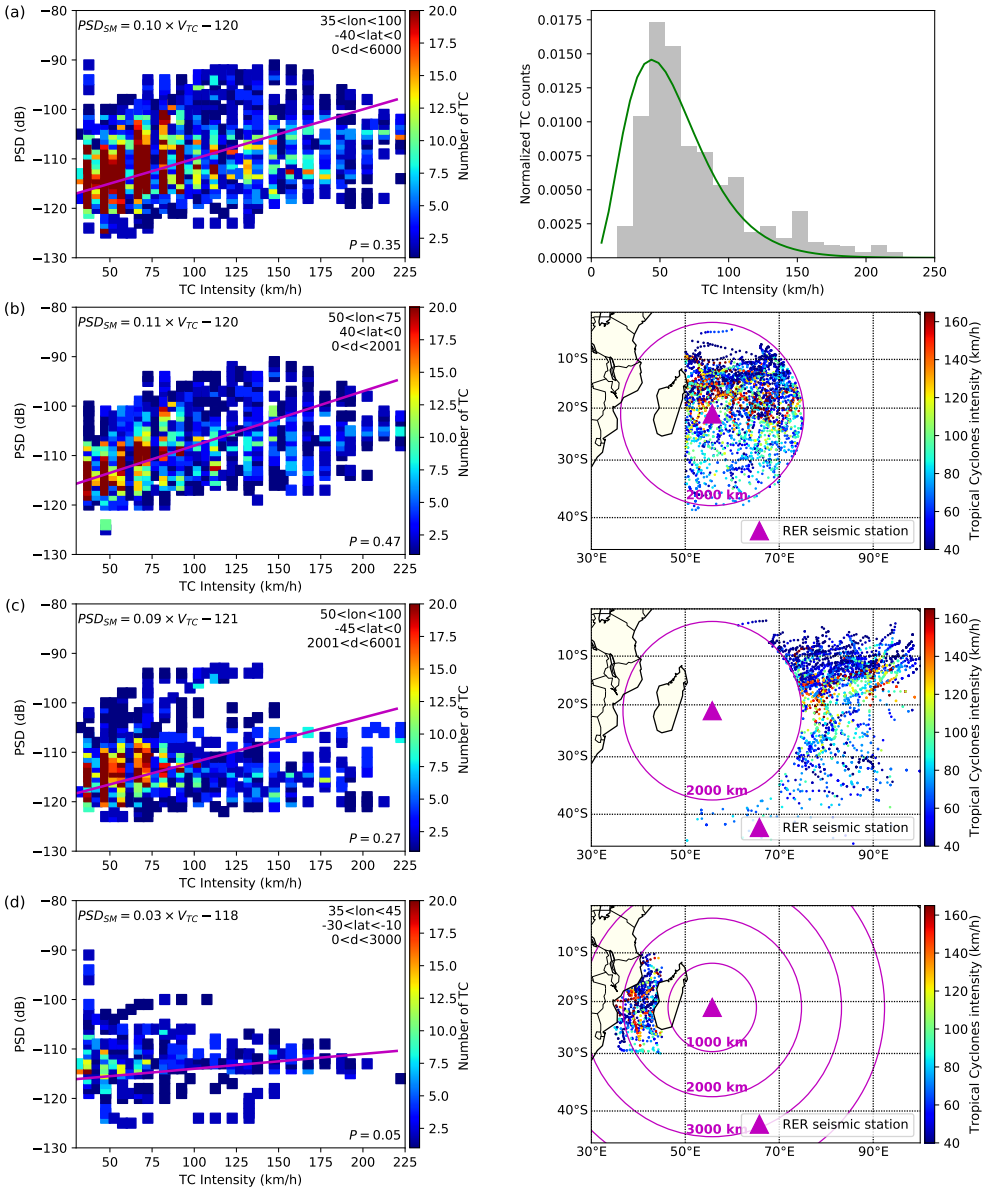

Figure 5. Regionalization of the cyclone signature. **Left column**: SM PSD in the 0.14–0.25 Hz frequency band (4 to 7 s period) plotted vs the cyclone intensity (V_{TC}). Color indicates the number of TC. For each subplot, the best transfer function between the SM PSD (PSD_{SM}) and V_{TC} is indicated at the top left corner. The P value (bottom right corner) indicates the Pearson coefficient correlation between the two data sets. Magenta line indicates the linear fit between the PSD_{SM} and V_{TC}. (**a**) Diagram combining all TC tracks, such as in Figure 3. The geographical locations for the other sub-groups (**b**–**d**) are shown in the top right corner and defined by the longitudes (lon), latitudes (lat) and distance ranges between the storm center and the seismic station RER. **Right column**: At the top, histogram of the density probability of the TC intensity data between 1999 and 2018 with their gamma distribution approximation (green line color). The 3 following subplots show the geographical boundaries for each sub-group of TC tracks.

The Pearson correlation coefficients and the transfer functions between the observed V_{TC} and the PSD_{SM}, for group 1,2, 3 and 4 are presented in Table 1. To validate these relations, we estimated the cyclone intensity for the cyclonic seasons 2017–2018 and 2018–2019 and compared them with the observed intensity (Figure 6), using the corresponding transfer function for each group. The fit between the observed and predicted cyclones are generally good, especially when the cyclone is isolated in time and space from

other events (e.g., Dumazile in March 2018 and Fakir in April 2018, Figure 6c). However, the TC intensity is generally over-estimated when two cyclones occur simultaneously in the studied area (e.g., Funani-Gelena in February 2019, Figure 6d). For the cyclones at a distance ≥3000 km, the intensities of the cyclones appear to be underestimated (e.g., Bouchra in November 2018, Figure 6d). Therefore, these equations are only valid for the cyclone with storm center at a distance <3000 km from the seismic station and more accurate in the occurrence of isolated cyclone and Pearson coefficient >0.3.

Table 1. Correlation between the SM PSD (PSD_{SM}) and the cyclone intensity (V_{TC}).

Group	Longitude	Latitude	Distance	Transfer Function	Pearson Coefficient
G1 (Figure 5a)	35° E < lon < 100° E	40° S < lat < 0° S	D ≤ 6000	$PSD_{SM} = 0.10 \times V_{TC} - 120$	0.35
G2 (Figure 5b)	50° E < lon < 75° E	40° S < lat < 0° S	D ≤ 2000	$PSD_{SM} = 0.11 \times V_{TC} - 120$	0.47
G3 (Figure 5c)	50° E < lon < 100° E	45° S < lat < 0° S	D > 2000	$PSD_{SM} = 0.09 \times V_{TC} - 121$	0.27
G4 (Figure 5d)	35° E < lon < 45° E	30° S < lat < 10° S	D ≤ 3000	$PSD_{SM} = 0.03 \times V_{TC} - 118$	0.05

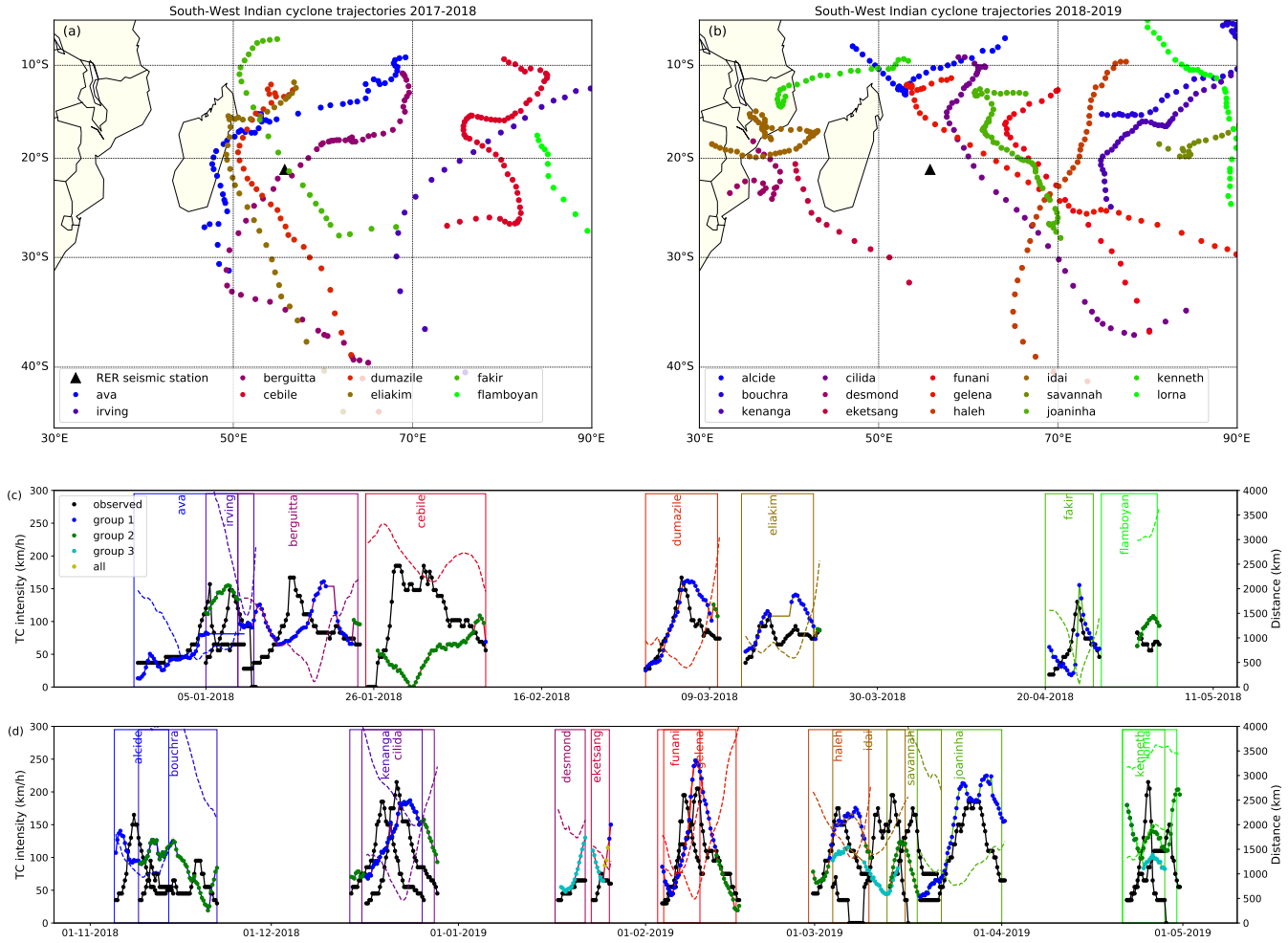

Figure 6. Cyclone trajectories and intensities. (**a**,**b**) Cyclone trajectories in the SWIO during the cyclonic seasons 2017–2018 (**a**) and 2018–2019 (**b**) with the TC center located every 6 h and color-coded by cyclones. RER station is located by a black triangle. (**c**) Observed (black dots) and estimated (colored dots) TC intensity for the cyclonic seasons 2017–2018 (left axis). The estimated TC intensity shown in blue, green and cyan dots were obtained from the transfer functions for a geographical location defined by group 2, group 3 and group 4, respectively (as defined in Figure 5 and Table 1). Dashed colored lines indicate the distance between the storm center and the seismic station RER (right axis). The Yellow dots (in Eketsang) color were estimated using the transfer function using all data (i.e., in Figure 5a). (**d**) Same as c but for the cyclonic season 2018–2019.

Delays (a few hours to a few days) between the observed and estimated V_{TC} are seen for some cyclones (e.g., Berguitta in January 2018, Figure 6c). Gualtieri et al. [17] made similar observation and attributed it to the non-linear coupling between atmosphere and ocean, and a potentially slow wind-wave growth which may take from a few hours to a few days to develop as suggested by Hasselmann et al. [32]. The Pearson correlation coefficient between the observed and predicted cyclone intensity is higher than 0.8, when the observed $V_{TC} \geq 75$ km/h, i.e., in the presence of tropical disturbance or higher categories, apart from Cebile (January 2018, Figure 6c), while the estimated V_{TC} is very weak. This could be associated with the presence of slow wind-wave growth. We can see that at the end of Cebile, the estimated V_{TC} begins to increase.

As already mentioned in Section 3.1.1, for the cyclones located in the Mozambique Channel, despite their powers and their distances less than 2000 km from Réunion Island, the SM recorded by RER seismic station remains surprisingly weak (Figure 5d). Very low correlation between the V_{TC} and the PSD_{SM} is observed ($P_{coef} = 0.05$). As proposed in Section 3.1.1, the weakness or even the absence of SM sources associated with TCs in the Mozambique Channel may be related to its small size impeding long fetches and to its complex structure limiting the possibility of developing standing waves.

3.2. Analysis of Cyclones Passing Near Réunion Island in the PM and SM Frequency Bands

3.2.1. Secondary Microseisms Source Locations

In this section, we focus on the results corresponding to well-polarized signals ($CpH \geq 0.6$, see Section 2.2). We computed the polarization analysis at RER seismic station, for the cyclonic seasons 2017–2018 and 2018–2019. The obtained CpH, CpZ and BAZ are plotted in Figure S5 and indicate that in the absence of cyclonic activity in the Indian ocean, the SM recorded at seismic station RER display BAZ ranging between $\sim$130° and 180°, centered at $\sim$150 $\pm$ 10°. This overall polarization can be associated with the dominant long-distance storm activity, occurring in particular in the southernmost part of the Indian Ocean, well recorded by the seismic station in La Réunion all over the year, but more frequently between April and October e.g., [29]. The low CpH (i.e., poorly polarized signal) observed in the presence of some cyclones is most likely due to multiple simultaneous sources of SM in the basin, such as the simultaneous occurrence of several storms and/or to simultaneous cyclone and austral swells. It is also very likely that other SM sources from other ocean basins may be recorded at RER, arriving with different azimuths and reducing the general strength of the ground motion polarization in this frequency range. During low CpH periods, the obtained BAZ are likely to not represent the BAZ of a single source but an average of simultaneous sources, hence without any physical signification. Figure 7 shows, however, that in the presence of well-polarized seismic signals occurring during a cyclone passage, the polarization (and hence the SM sources) points toward the storm center (e.g., Dumazile, Fakir and Cilida), consistent with the MF data. This agreement occurs dominantly when the cyclone is at the south or south-east of the island. This may indicate that the cyclonic swell direction interacts with long-distance swells at $\sim$150°, but further investigations and modeling would be necessary to better understand these characteristics.

Among the 22 cyclones that occurred between 2017 and 2019, five cyclones (Berguitta, Dumazile, Eliakim, Fakir and Cilida) passed close to the island. However, only Dumazile, Eliakim, Fakir and Cilida have a $CpH > 0.6$ during part of their lifespan (Figure S5). For these cyclones, we computed the polarization at all available seismic stations in La Réunion, from the permanents (G and PF) and the temporary (ZF) seismic networks. The obtained BAZ, of Dumazile, Fakir and Cilida are presented in Figure 7 and point consistently towards the SSE or the SE, i.e., towards the storm center. The results for Eliakim are not presented here as they are already presented and discussed in detail in another work [Bousquet et al, in this special issue] but points toward the SW, also in good agreement with the storm center. In Figure 7 we compare the average theoretical BAZ issued from the storm center locations provided by MF (pink arrows) with the average seismically derived

BAZ for Dumazile (lime arrow, Figure 7b), Fakir (Blue arrows, Figure 7c) and Cilida (green arrows, Figure 7d), obtained from the polarization analysis, for the various seismic stations in La Réunion. Figure 7 indicates indeed that in the presence of isolated cyclone and with $CpH > 0.6$, the SM BAZ point consistently toward the storm center.

Combining the azimuth issued from polarization analysis with the delays between the arrival time of PM and SM, it should be feasible to get an approximate location of the SM source, using a single seismic station e.g., [5]. However, polarization must be used with caution since, as explained above, the results may be biased by simultaneous SM sources from other storms worldwide, and in the case of La Réunion, by the strong depressions moving around Antarctica and generating austral swells [29]. Figure 7 indicates that a cyclone far from the seismic station (distance > 2000 km) has little to no influence on the computed BAZ (e.g., Flamboyan May 2018). Our polarization analyses show that a cyclone located in the Mozambique Channel (e.g., Idai, March 2019, Figure S5c) does not influence the recorded SM in La Réunion, which is fully consistent with the PSD results in Section 3.1.3 that showed weak amplitudes. Tracking the cyclone trajectory is beyond the scope of the present work, but should be achieved using different methods e.g., [9,18–21].

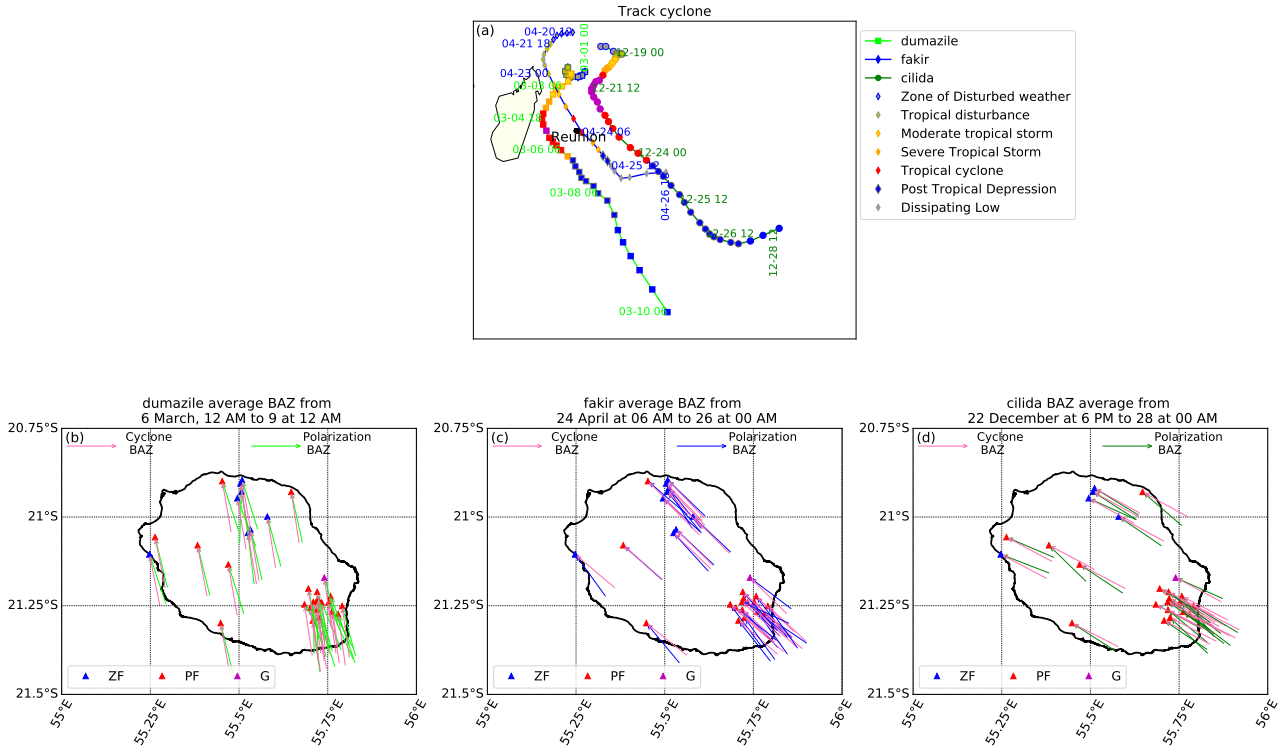

Figure 7. Cyclone trajectories and SM polarization in La Réunion Island. (**a**) Tracks of the tropical cyclones that have a CpH > 0.6 between 2017 and 2019. (**b**–**d**) Comparison of the averages obtained from the theoretical BAZ (pink arrows) with the average seismically measured BAZ for Dumazile ((**b**), lime arrow), Fakir ((**c**), Blue arrows) and Cilida ((**d**), green arrows).

3.2.2. Secondary Microseisms and Cyclone Intensity

In this Section, we analyze and discuss the seismic signatures of cyclones that passed close to Réunion Island, at a distance ≤500 km and recorded by the permanent (PF) and temporary (ZF) seismic networks on the Island. As discussed in Section 3.1, the intensification of the SM amplitude depends on the storm's intensity and the distance from the station to the storm center. Our results suggest that the seismic station RER starts to record SM visible on the PSD for a storm with $V_{TC} > 60$ km/h, i.e., above a depression stage (Table S1) and at a distance as far as ~4000 km (see Figures 1–3). Figure 8a maps cyclone tracks that passed in the proximity of La Réunion (distance ≤ 500 km) during the period 2011–2019 and Figure 8b–q present the variations of the amplitude of the SM

during each cyclone, at all seismic stations running on the island at that time (cf map in the inset), together with the cyclone distance and intensity. Figure 8b–q show that during the life span of a given storm, all operating seismic stations display very homogeneous records. For a given cyclone, the temporal evolution of the SM amplitude (same as for PM amplitude, see Section 3.2.3) has a very similar pattern at all stations despite some differences in amplitudes, depending on the location of the station on the island. This observation suggests that the amplitude of the microseismic noise largely depends on the storm dynamics and is modulated by local sites effects. Figure 8 indicates that each cyclone has its own seismic signature and confirms that the maximum SM amplitude depends on the distance to the storm center (e.g., Cherono, Figure 8b) and/or on its strength (e.g., Dumile and Fakir in Figure 8d,o). In this case, the SM is likely to be generated at the storm center in the presence of broad ocean wave directional spectra, as modeled by Ardhuin et al. [8]. However, as seen in Section 3.1, a long-distance austral swell, if present, may influence the observed SM.

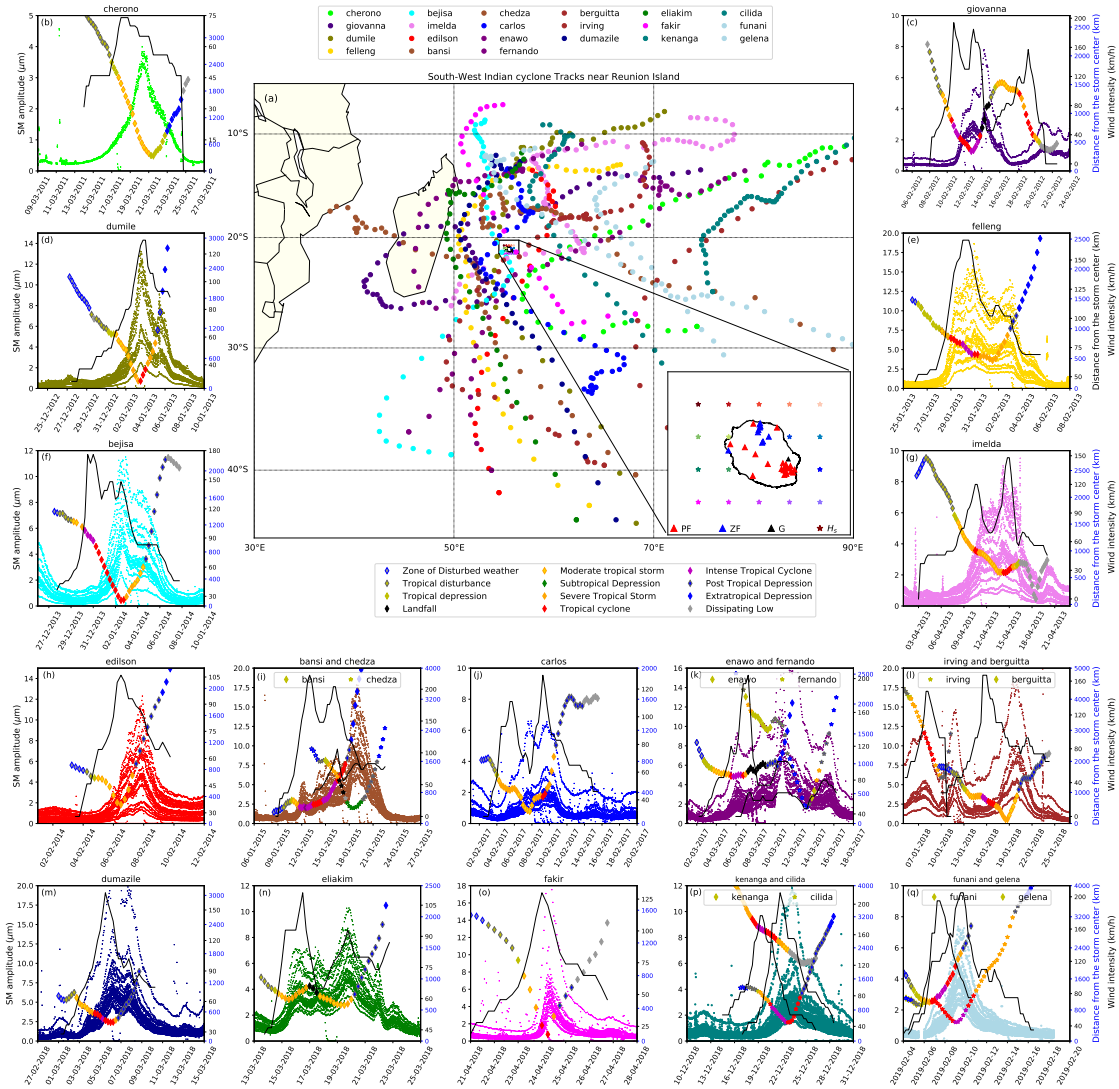

Figure 8. SM signatures of cyclones at La Réunion seismic stations. (**a**) Tracks of the tropical cyclones that passed close to Réunion Island between 2011 and 2019 (distance station-to-storm center <500 km). The inset map shows the seismic stations onland (in red from the OVPF and in blue from the ZF temporary network) and the offshore node locations at which the modeled H_S are extracted. (**b**–**q**) Each subplot shows the RMS amplitude of the SM (colored dots, left axis) for each selected cyclone, together with the distance between the storm center and the seismic station plotted as colored diamonds (on the right axis, blue scale) and the cyclone intensity plotted as continuous black lines (right axis, black scale). For each cyclone, the RMS amplitude at the various stations is plotted with the same color code as the track on the map Figure 8a. All seismic stations have the same color.

A delay (a few hours to a few days) between the maximum cyclone intensity (and after the passage of the cyclone close to the island) and the generation of the SM is visible for some storms (e.g., Edilson, Berguitta, Figure 8h,l). We associate these SM to the possible interaction between the cyclonic sea-states and an austral swell or to the time needed for a cyclone to generate standing waves resulting from the storm itself and its displacement. Alternatively, this delay may be related to the slow wind-wave growth, which may take from a few hours to a few days [32], as mentioned previously.

3.2.3. Primary Microseisms and Significant Wave Height

After analyzing the microseismic noise in the SM band (i.e., in the 3–10 s period), we focus here on the PM band (i.e., in the 10–20 s period) which is accepted to be related to the interaction of incoming waves with the local coastal bathymetry. In this section, we therefore compare the seismic signal to the significant wave height (H_S) extracted from the global GOW2 hindcast wave model from Perez et al. [22] implemented with the WAVEWATCH III wave model [33] with a reduced 0.25° grid space for the coastal locations and 0.5° elsewhere. Their model parametrizations used a high resolution of the input forcings and of the output wave model allowing the cyclones to be well captured, hence motivating our choice for the GOW2 model.

The tracks of the cyclones used to investigate the PM are plotted in Figure 9a and the recording stations on La Réunion are shown on the inset map. We used the same cyclones and seismic stations as for the SM analysis in Section 3.2.2 (Figure 8a). For each cyclone, the PM RMS amplitude measured at the various seismic stations are shown in Figure 9b–q (using the same color code as the cyclone tracks in Figure 9a). The corresponding H_S during the life span of each cyclone, at different nodes are also presented as colored continuous lines. These figures suggest that the characteristic of the H_S at each node may slightly differ in amplitude from each other and depends on the cyclone trajectories relative to the island. In the presence of a cyclone, the maximum H_S is located at the nodes closest to the cyclone center. It is clear that cyclones tracked east of the island have a maximum H_S computed at the eastern nodes of the wave model (e.g., Cherono, Dumile, Funani & Gelena, Figure 9b,d,q). Alternatively, when cyclones passed west from the island, the maximum H_S are clearly recorded at the western nodes (e.g., Felleng, Bejisa, Dumazile, Figure 9e,f,m). In the presence of a cyclone tracked on both sides of the island (i.e., formed at the western side and that passed close to the island at the eastern side or vice-versa), the nodes displaying maximum H_S values change accordingly. For example, Fakir (Figure 9o) began on 20 April 2018 on the north-west of the island, inducing a maximum H_S at the northern and western nodes. However, on April 24, Fakir was tracked at the eastern side of the island inducing maximums H_S values at the eastern nodes. These observations confirm that the GOW2 model captured well the cyclone activity and its local signatures around Réunion Island, confirming its ability to study the cyclone activity around La Réunion and in particular the relations between the PM amplitude and the wave height H_S.

For a given cyclone, the variations of the PM amplitudes recorded by the different seismic stations on the island display very similar patterns (Figure 9b–q). However, each station displays slightly different PM amplitudes, likely depending on local site effects and on the location of the station relative to the coast (similar conclusion as for the SM). Our results show that the strength of the PM amplitude also varies with the distance to the storm center and intensity. The cyclone trajectory also influences the PM amplitudes. Cyclones that passed west of the island (e.g., Dumile, Figure 9d) generated much stronger PM than those tracked east of the island (e.g., Fakir, Figure 9o). Dumile and Fakir have a comparable wind intensity (V_{TC} = ∼125 km/h Figure 8d,o), but the PM amplitude generated by Dumile is twice stronger than Fakir (Figure 9d,o). The observed weak PM signal from Fakir is most likely due to the fact that the waves generated by the cyclone at the north-east of the island were only partly interacting with the local bathymetry and/or was rapidly attenuated before interacting with the local bathymetry.

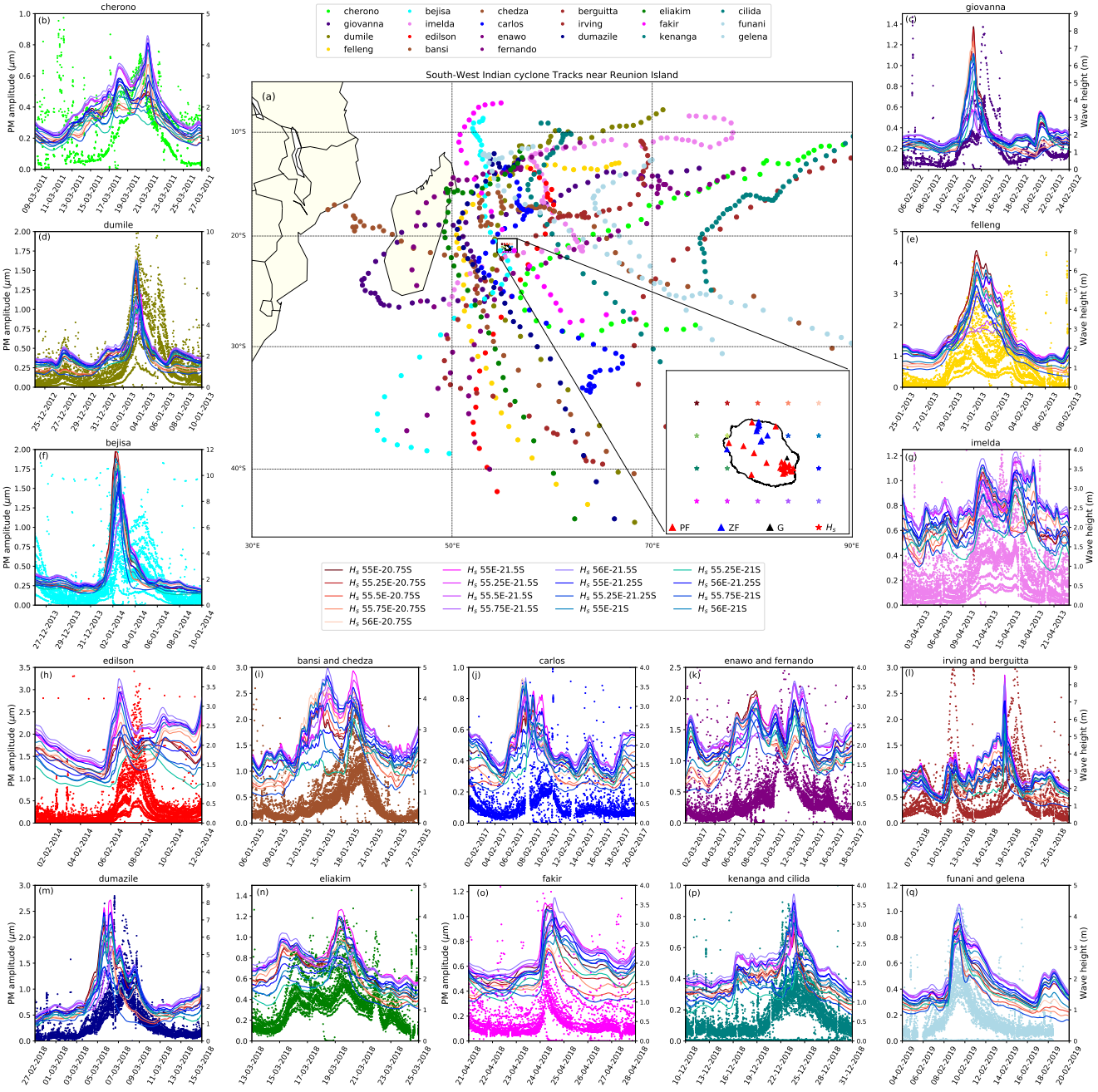

Figure 9. PM signatures of cyclones at La Réunion seismic stations. (**a**) Tracks of the cyclones that passed near Réunion island between 2011 and 2019 (distance < 500 km). The inset map shows the seismic stations onland (in red from the OVPF permanent and in blue from the ZF temporary, networks) and the offshore node locations at which the modeled H_S are extracted. (**b**–**q**) Each subplot shows the RMS amplitude of the PM (colored dots, left axis) together with the modeled significant wave height H_S extracted from GOW2 model Perez et al. [22] (plotted in colored continuous lines). The different H_S colors indicate their locations in the inset map. For each cyclone, the RMS amplitude is plotted in the same color as the track on the map in the center and all stations have the same color. Note the different scale amplitude for each subplot adapted for both the H_S and the PM RMS amplitude.

At first sight, the PM RMS amplitude correlates well with the H_S amplitude extracted from the GOW2 model (Figure 9b–q), in good agreement with the process of PM generated by oceanic waves interaction with the local bathymetry, creating elastic waves with the same frequency as the oceanic waves. Some exceptions are observed where the strongest PM is recorded a few hours (to a few days) after the strongest H_S. Those PM are likely originating from long-distance swells. As an example, for Edilson (Figure 9h), the maximum PM

amplitude (∼3.5 µm) is recorded one day and 15 h (from 7 to 9 February 2014) after it was tracked at the nearest of the island and the highest H_S at different nodes were computed. However, a small PM peak (with a maximum value of ∼1.5 µm) is also visible in the measurements from 5 to 7 February and likely corresponds to the maximums H_S (i.e., between 5 and 7 February 2014) generated in coastal areas. The recorded PM between 7 and 9 February was likely originating from long distant swells. The presence of the PM generated from simultaneous local waves and distant swells are seen for Giovanna, Felleng, Bejisa, Fernando (Figure 9c,e,f,k). Rindraharisaona et al. [5] have also associated the observed PM between 13 and 15 March 2017 for Fernando to a distant source.

3.2.4. Quantifying Relationship between Primary Microseisms and Significant Wave Heights

To determine the relationship between the PM amplitude and the significant H_S, we present in Figure 10 two cyclones as examples: Dumile and Fakir. Figure 10a shows the tracks of cyclones in the neighborhood of La Réunion. Dumile formed on 27 December 2013, as a tropical disturbance (TD) at the north-east of the island and became a TC on 3 January 2014, during its passage west of the island and continued its journey southward. In contrast, Fakir started as disturbed weather on 20 April 2018, north-west from La Réunion and evolved rapidly and approached the island at its northern and eastern sides on April 24 as a TC. The following zoomed maps of La Réunion Figure 10b,c plot the Pearson correlation coefficients (P_{coef}) between the PM amplitude observed at the seismic station MAT (located on the map) and the modeled H_S at each surrounding node. We selected the station MAT because this permanent station operated since January 2011 and is characterized by a maximum PM amplitude (in most cases), suggesting a good sensitivity to microseisms. In general, for each cyclone, at least one node has a $P_{coef} > 0.80$. The P_{coef} for the different cyclones were computed using the data between the period within the vertical black dashed lines on each following subplot (Figure 10d,e). During these selected periods, the storm center was either at the north or alongside the island. This indicates that a simple linear regression is appropriate to estimate the relation between the near-coastal PM and the modeled H_S. As mentioned previously, H_S around the island strongly depends on the cyclone trajectory. The PM amplitude was simultaneously strengthened with the H_S for Dumile and Fakir, as the wind speed increased to their maximum.

Figure 10b shows that in the case of Dumile, the western nodes have higher P_{coef} than the northern or eastern nodes. The highest correlation (P_{coef} = 0.93) corresponds to the node *W*1 Table 2, i.e., at the node west of the island, close to the shore and close to the seismic station MAT, indicating that the oceanic waves interacted efficiently with the local bathymetry around this point (north-western side). In contrast, for Fakir (Figure 10c), H_S modeled at the northern nodes and the node at 55.75° E 21.00° S correlate well with the PM amplitude, with $P_{coef} > 0.93$, which is consistent with the track of Fakir that passed north and east of the island. The significant wave heights modeled at the northern nodes continued travelling southward and likely interacted with the local bathymetry on the northern shores (hence the highest P_{coef} = 0.97 at the node *N*), which, in turn, generated PM that was recorded by all seismic stations on the island (Figure 9o). As Fakir continued its journey toward the south, H_S in the northern nodes decreased rapidly whereas nodes on the eastern side displayed an increasing and a second H_S peak on April 24 (for the nodes located in the eastern part of the island). We used these five nodes to compute the transfer functions presented in Figure 10f,g and Table 2.

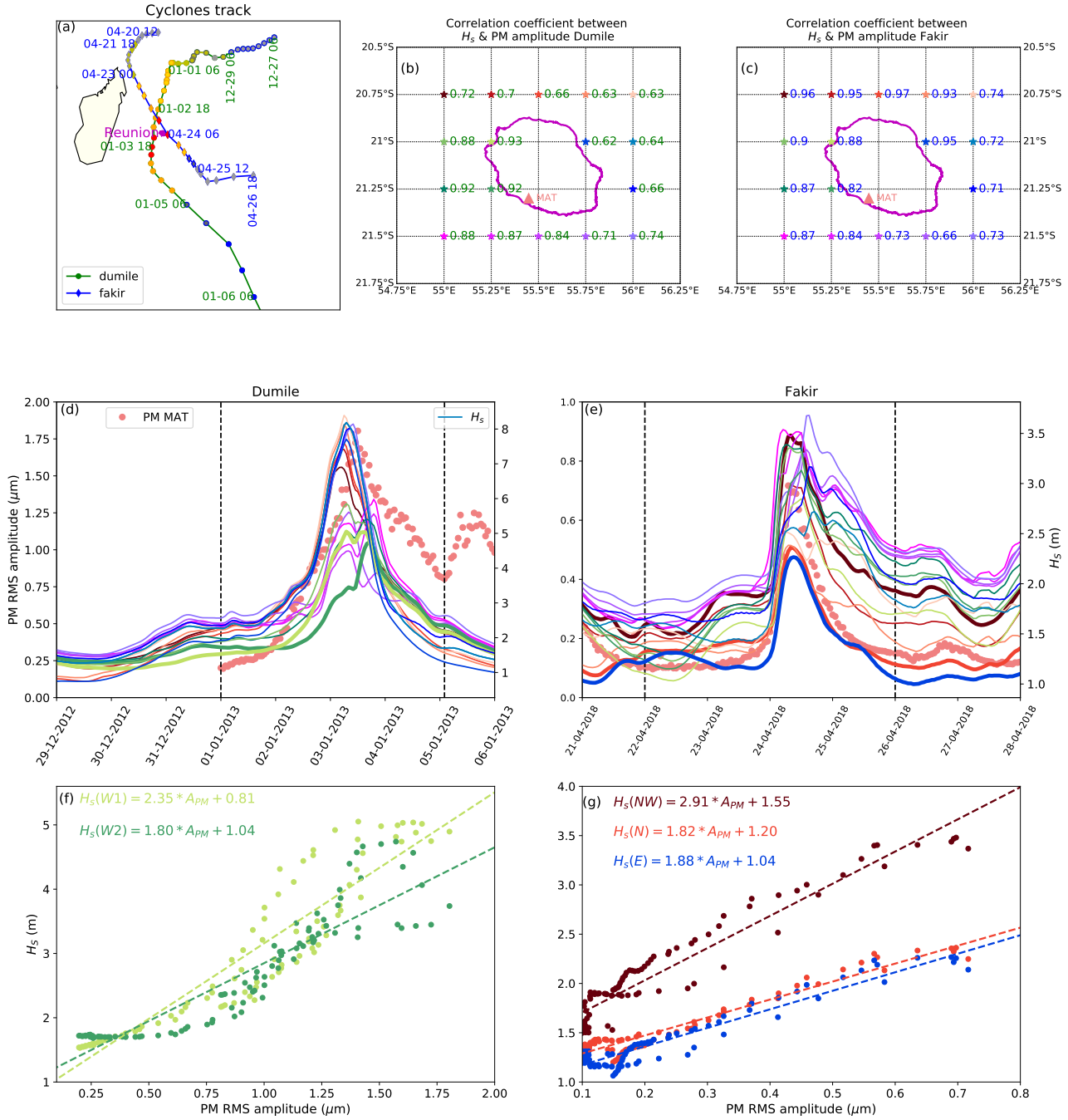

Figure 10. Primary microseisms and significant wave-height correlation for TC Dumile and fakir. (**a**) Trajectories of Dumile (in December 2012–January 2013, dots symbol) and Fakir (in April 2018, diamonds symbol). The cyclone is located every 6 h. To avoid overcrowded map, month, day and hour only are plotted on the maps. The cyclone categories have the same legend as in Figure 8. (**b**) Correlation coefficient between H_S modeled at different nodes around the island and PM amplitude recorded at terrestrial station MAT (pink triangle) for Dumile. (**c**) Same as (**b**) but for Fakir. (**d**) Dumile RMS PM amplitude at MAT station (pink dots), together with the significant wave heights H_S (colored continuous lines) from the GOW2 models extracted at different nodes around the island (with the same color as the nodes in (**b**)). H_S used to determine the transfer functions are shown in bold lines. Vertical dashed lines indicate the time window used to compute the correlation coefficient and the transfer functions. (**e**) Same as (**d**) but for Fakir. (**f**,**g**) Relation between the significant wave height H_S as a function of the hourly RMS amplitude of the PM for Dumile and Fakir at station MAT, together with the corresponding linear transfer functions. Dot colors are the same as the bold H_S lines from plots (**d**,**e**).

Table 2. Correlation between the PM amplitude A_{PM} and significant wave height H_S (PSD_{SM}). Node corresponds to the selected node location, as for Figure 10.

Node	Location	P_{coef}	Transfer Function	Cyclone
W1	55.25° E 21.00° S	0.93	$H_s(\mathrm{W1}) = 2.35 \times \mathrm{A_{PM}} + 0.81$	Dumile
W2	55.25° E 21.25° S	0.92	$H_s(\mathrm{W2}) = 1.80 \times \mathrm{A_{PM}} + 1.04$	Dumile
NW	55.00° E 20.75° S	0.96	$H_s(\mathrm{NW}) = 2.91 \times \mathrm{A_{PM}} + 1.55$	Fakir
N	55.50° E 20.75° S	0.97	$H_s(\mathrm{N}) = 1.82 \times \mathrm{A_{PM}} + 1.20$	Fakir
E	55.75° E 21.00° S	0.95	$H_s(\mathrm{E}) = 1.88 \times \mathrm{A_{PM}} + 1.04$	Fakir

To validate the transfer functions, we estimated H_S for several cyclones that passed near La Réunion, and recorded by seismic station MAT (Figures S6–S8). In these figures are shown first (in a) the tracks of the cyclones considered and then the H_S-PM Pearson correlation coefficients (P_{coef}) at the wave model nodes located around the island for (b, c and d). The three bottom subplots (e, f and g) present the observed PM at station MAT, together with the estimated H_S issued from the transfer function and the modeled GOW2. The vertical black dashed lines limit the period used to compute the P_{coef}. In general, the difference between the modeled and computed H_S is less than 1 m, for any nodes that had $P_{corr} \geq 0.8$, whereas larger disagreement is seen between the two parameters with $P_{coef} < 0.8$. More details about the transfer function validation are given in Section S2.

4. Conclusions

We investigated microseisms generated by tropical cyclones/storms between 1999 and 2020 in the SWIO, using seismic stations in Réunion Island. The daily average of the PSD indicates the intensification of the microseisms in the presence of cyclone. Our analysis of the temporal evolution of the PSD of the SM, at periods ∼4 to 7 s, indicates a close relationship between the SM amplitude and the cyclone intensity. SM polarization analyses show that one can retrieve the BAZ of the storm center in the presence of well-polarized signals, i.e., $CpH > 0.6$ and isolated cyclone. The near-coastal PM amplitude (in the 10 to 20 s period) correlates well with the significant wave height from global hindcast model, with $P_{coef} > 0.8$. We have shown that PM represent a good proxy of the oceanic wave heights under cyclonic conditions. We thus computed transfer functions between the two parameters, allowing the derivation of modeled cyclonic significant wave heights from the seismic noise amplitude recorded on land, and to provide the new opportunity to use coastal and island seismic stations as terrestrial wave gauges. Continuous monitoring of microseisms provides therefore additional information on the cyclone and ocean activity, complementing satellite and other ground or marine observations.

Our results increase the number of the observational parameters related to past cyclones in the SWIO, which is crucial for better understanding the effects and signatures of cyclones (here the ocean activity) and for better forecasting the future cyclone activity and the related hazards. The present work demonstrates the feasibility of using microseismic noise in monitoring past oceanic activity. However, the non-linear coupling between atmosphere and ocean (hence the generation of microseismic noise) may limit the monitoring of the cyclone activity in real time, using microseismic data alone. Moreover, the simultaneous occurrence of the austral swell and/or two cyclones also complexifies the data analysis, in particular for determining its location. This issue could be solved by performing an $f-k$ (frequency-wave number) analysis and/or other methods that were referenced in Section 3.2.1. Despite these limitations, the present work suggests that the use of the seismic data to quantify the sea state may bring a clear added value and even if there are still challenges and improvements that needs to be overcome beforehand, real-time monitoring of sea state from seismic data is undoubtedly a realistic opportunity.

Supplementary Materials: The following are available online at https://www.mdpi.com/article/10.3390/atmos12040488/s1.

Author Contributions: Conceptualization, E.J.R. and G.B.; methodology, E.J.R. and G.B.; software, E.J.R.; validation, E.J.R., G.B. and E.C.; formal analysis, E.J.R.; investigation, E.J.R.; data curation, E.J.R., G.B., F.R.F., A.G., and E.C.; writing—original draft preparation, E.J.R.; writing—review and editing, E.J.R., G.B., E.C., F.R.F., and A.G.; project administration, G.B. and E.J.R.; funding acquisition, G.B.; All authors have read and agreed to the published version of the manuscript.

Funding: This research was funded by the European Union, the Regional Council of Réunion Island and the French State under the frame of INTERREG-V Indian Ocean 2014–2020 research project "ReNovRisk Cyclones and Climate Change" (TF, A1.3).

Institutional Review Board Statement: Not applicable.

Informed Consent Statement: Not applicable.

Data Availability Statement: The data presented in this study are available on request from the RESIF data center.

Acknowledgments: This work benefited from the funding of the European Union, the Regional Council of Réunion Island and the French State under the frame of INTERREG-V Indian Ocean 2014–2020 research project "ReNovRisk-Cyclones and Climate Change" (TF, A1.3). E. Rindraharisaona was funded by the ReNovRisk project. Thanks to the University of La Réunion and the Laboratoire Geosciences Réunion for their supports. We acknowledge the French Geoscope network for the quality and the access to the RER seismic data. We are thankful to INSU-RESIF/SISMOB instrumental pool for providing five stations deployed in the "Rivière des Pluies" network and to CNRS-INSU (Institut National des Sciences de l'Univers) funding from the TelluS-SYSTER program. The data are archived at RESIF data center (http://seismology.resif.fr, accessed on 12 April 2021). We are very grateful to the OVPF (Observatoire Volcanologique du Piton de la Fournaise) and to IPGP colleagues who maintain the PF seismic stations and for the easy access and the quality of their data. We appreciate the help of E. Delcher during the Riviere des Pluies fieldworks. We thank Laura Ermert and an anonymous reviewer for providing constructive comments and suggestions in their reviews and the Editor for additional careful reading of the manuscript. This is IPGP contribution number 4188.

Conflicts of Interest: The authors declare no conflict of interest.

Abbreviations

The following abbreviations are used in this manuscript:

FDSN	Federation of Digital Sesimograph Networks
IPGP	Institut de Physique du Globe de Paris
OVPF	Observatoire Volcanologique du Piton de la Fournaise
SWIO	South West Indian Ocean
TC	Tropical cyclone
PM	Primary microseisms
SM	Secondary microseisms
LPSM	Long period secondary microseisms
MF	Météo France
PSD	Power spectral density
BAZ	Backazimuth
H_S	Significant wave height

References

1. Grevemeyer, I.; Herber, R.; Essen, H.H. Microseismological evidence for a changing wave climate in the northeast Atlantic Ocean. *Nature* **2000**, *408*, 349–352. [CrossRef]
2. Longuet-Higgins, M.S. A theory of the origin of microseisms. *Philos. Trans. R. Soc. Lond. Ser. A Math. Phys. Sci.* **1950**, *243*, 1–35.
3. Hasselmann, K. A statistical analysis of the generation of microseisms. *Rev. Geophys.* **1963**, *1*, 177–210. [CrossRef]
4. Davy, C.; Barruol, G.; Fontaine, F.R.; Cordier, E. Analyses of extreme swell events on La Réunion Island from microseismic noise. *Geophys. J. Int.* **2016**, *207*, 1767–1782. [CrossRef]
5. Rindraharisaona, E.; Cordier, E.; Barruol, G.; Fontaine, F.; Singh, M. Assessing swells in La Réunion Island from terrestrial seismic observations, oceanographic records and offshore wave models. *Geophys. J. Int.* **2020**, *221*, 1883–1895. [CrossRef]
6. Ardhuin, F.; Gualtieri, L.; Stutzmann, E. How ocean waves rock the Earth: Two mechanisms explain microseisms with periods 3 to 300 s. *Geophys. Res. Lett.* **2015**, *42*, 765–772. [CrossRef]

7. Barruol, G.; Reymond, D.; Fontaine, F.R.; Hyvernaud, O.; Maurer, V.; Maamaatuaiahutapu, K. Characterizing swells in the southern Pacific from seismic and infrasonic noise analyses. *Geophys. J. Int.* **2006**, *164*, 516–542. [CrossRef]
8. Ardhuin, F.; Stutzmann, E.; Schimmel, M.; Mangeney, A. Ocean wave sources of seismic noise. *J. Geophys. Res. Ocean.* **2011**, *116*. [CrossRef]
9. Davy, C.; Barruol, G.; Fontaine, F.R.; Sigloch, K.; Stutzmann, E. Tracking major storms from microseismic and hydroacoustic observations on the seafloor. *Geophys. Res. Lett.* **2014**, *41*, 8825–8831. [CrossRef]
10. Essen, H.H.; Krüger, F.; Dahm, T.; Grevemeyer, I. On the generation of secondary microseisms observed in northern and central Europe. *J. Geophys. Res. Solid Earth* **2003**, *108*. [CrossRef]
11. Obrebski, M.; Ardhuin, F.; Stutzmann, E.; Schimmel, M. How moderate sea states can generate loud seismic noise in the deep ocean. *Geophys. Res. Lett.* **2012**, *39*. [CrossRef]
12. Obrebski, M.; Ardhuin, F.; Stutzmann, E.; Schimmel, M. Detection of microseismic compressional (P) body waves aided by numerical modeling of oceanic noise sources. *J. Geophys. Res. Solid Earth* **2013**, *118*, 4312–4324. [CrossRef]
13. Barruol, G.; Davy, C.; Fontaine, F.R.; Schlindwein, V.; Sigloch, K. Monitoring austral and cyclonic swells in the "Iles Eparses"(Mozambique channel) from microseismic noise. *Acta Oecologica* **2016**, *72*, 120–128. [CrossRef]
14. Stutzmann, E.; Ardhuin, F.; Schimmel, M.; Mangeney, A.; Patau, G. Modelling long-term seismic noise in various environments. *Geophys. J. Int.* **2012**, *191*, 707–722. [CrossRef]
15. Gualtieri, L.; Stutzmann, É.; Capdeville, Y.; Farra, V.; Mangeney, A.; Morelli, A. On the shaping factors of the secondary microseismic wavefield. *J. Geophys. Res. Solid Earth* **2015**, *120*, 6241–6262. [CrossRef]
16. Lin, J.; Lin, J.; Xu, M. Microseisms generated by super typhoon Megi in the western Pacific Ocean. *J. Geophys. Res. Ocean.* **2017**, *122*, 9518–9529. [CrossRef]
17. Gualtieri, L.; Camargo, S.J.; Pascale, S.; Pons, F.M.; Ekström, G. The persistent signature of tropical cyclones in ambient seismic noise. *Earth Planet. Sci. Lett.* **2018**, *484*, 287–294. [CrossRef]
18. Retailleau, L.; Gualtieri, L. Toward high-resolution period-dependent seismic monitoring of tropical cyclones. *Geophys. Res. Lett.* **2019**, *46*, 1329–1337. [CrossRef]
19. Simonelli, A.; De Luca, G.; Giacomelli, U.; Terreni, G.; Di Virgilio, A. Observation by Means of An Underground Ring Laser Gyroscope of Love Waves Generated in the Mediterranean Sea: Source Direction and Comparison with Models. *Seismol. Res. Lett.* **2020**, *91*, 1730–1737. [CrossRef]
20. Hadziioannou, C.; Gaebler, P.; Schreiber, U.; Wassermann, J.; Igel, H. Examining ambient noise using colocated measurements of rotational and translational motion. *J. Seismol.* **2012**, *16*, 787–796. [CrossRef]
21. Gerstoft, P.; Fehler, M.C.; Sabra, K.G. When katrina hit california. *Geophys. Res. Lett.* **2006**, *33*. [CrossRef]
22. Perez, J.; Menendez, M.; Losada, I.J. GOW2: A global wave hindcast for coastal applications. *Coast. Eng.* **2017**, *124*, 1–11. [CrossRef]
23. Leroux, M.D.; Meister, J.; Mekies, D.; Dorla, A.L.; Caroff, P. A climatology of southwest Indian Ocean tropical systems: Their number, tracks, impacts, sizes, empirical maximum potential intensity, and intensity changes. *J. Appl. Meteorol. Climatol.* **2018**, *57*, 1021–1041. [CrossRef]
24. Fontaine, F.R.; Barruol, G.; Gonzalez, A. Rivière des Pluies Project, La Réunion Island, 2015–2018. RESIF–Réseau Sismologique et Géodésique Français. *Seism. Netw.* **2015**. [CrossRef]
25. McNamara, D.E.; Buland, R.P. Ambient noise levels in the continental United States. *Bull. Seismol. Soc. Am.* **2004**, *94*, 1517–1527. [CrossRef]
26. Flinn, E. Signal analysis using rectilinearity and direction of particle motion. *Proc. IEEE* **1965**, *53*, 1874–1876. [CrossRef]
27. Fontaine, F.R.; Barruol, G.; Kennett, B.L.; Bokelmann, G.H.; Reymond, D. Upper mantle anisotropy beneath Australia and Tahiti from P wave polarization: Implications for real-time earthquake location. *J. Geophys. Res. Solid Earth* **2009**, *114*. [CrossRef]
28. Herrmann, R.B. Computer programs in seismology: An evolving tool for instruction and research. *Seismol. Res. Lett.* **2013**, *84*, 1081–1088. [CrossRef]
29. Davy, C.; Stutzmann, E.; Barruol, G.; Fontaine, F.R.; Schimmel, M. Sources of secondary microseisms in the Indian Ocean. *Geophys. J. Int.* **2015**, *202*, 1180–1189. [CrossRef]
30. Peterson, J.R. *Observations and Modeling of Seismic Background Noise*; Technical Report; US Geological Survey: Reston, VA, USA, 1993.
31. Agresti, A. *Foundations of Linear and Generalized Linear Models*; John Wiley & Sons: Hoboken, NJ, USA, 2015.
32. Hasselmann, K.; Barnett, T.; Bouws, E.; Carlson, H.; Cartwright, D.; Enke, K.; Ewing, J.; Gienapp, H.; Hasselmann, D.; Kruseman, P.; et al. Measurements of wind-wave growth and swell decay during the Joint North Sea Wave Project (JONSWAP). *Ergaenzungsheft Zur Dtsch. Hydrogr. Z. Reihe A* **1973**.
33. Tolman, H.L.; The WAVEWATCH III Development Group. User Manual and System Documentation of WAVEWATCH III® version 4.18 Technical Note 316, NOAA/NWS/NCEP/MMAB, 282 pp. +Appendices. 2014. Available online: https://polar.ncep.noaa.gov/waves/wavewatch/ (accessed on 12 April 2021).

AGU PUBLICATIONS

Journal of Advances in Modeling Earth Systems

RESEARCH ARTICLE
10.1002/2017MS001177

Key Points:
- A new coupled Ocean-Waves-Atmosphere system (MSWC) is presented in this paper
- MSWC successfully simulates air-sea processes under a tropical cyclone at kilometer resolution
- MSWC shows the importance of using a fully coupled system to have consistent sea salt aerosol fluxes and concentration

Correspondence to:
J. Pianezze,
joris.pianezze@univ-reunion.fr

Citation:
Pianezze, J., Barthe, C., Bielli, S., Tulet, P., Jullien, S., Cambon, G., et al. (2018). A new coupled ocean-waves-atmosphere model designed for tropical storm studies: Example of tropical cyclone Bejisa (2013–2014) in the South-West Indian Ocean. *Journal of Advances in Modeling Earth Systems*, *10*, 801–825. https://doi.org/10.1002/2017MS001177

Received 21 SEP 2017
Accepted 25 FEB 2018
Accepted article online 1 MAR 2018
Published online 23 MAR 2018

A New Coupled Ocean-Waves-Atmosphere Model Designed for Tropical Storm Studies: Example of Tropical Cyclone Bejisa (2013–2014) in the South-West Indian Ocean

J. Pianezze[1], C. Barthe[1], S. Bielli[1], P. Tulet[1], S. Jullien[2], G. Cambon[2], O. Bousquet[1], M. Claeys[1], and E. Cordier[3]

[1]Laboratoire de l'Atmosphère et des Cyclones (LACy), Université La Réunion, CNRS, Météo-France, Saint-Denis, France, [2]Ifremer, Laboratoire d'Océanographie Physique et Spatiale (LOPS), Université Brest, CNRS, IRD, IUEM, Plouzané, France, [3]Observatoire des Sciences de l'Univers de La Réunion (OSU-R), Université La Réunion, CNRS, Saint-Denis, France

Abstract Ocean-Waves-Atmosphere (OWA) exchanges are not well represented in current Numerical Weather Prediction (NWP) systems, which can lead to large uncertainties in tropical cyclone track and intensity forecasts. In order to explore and better understand the impact of OWA interactions on tropical cyclone modeling, a fully coupled OWA system based on the atmospheric model Meso-NH, the oceanic model CROCO, and the wave model WW3 and called MSWC was designed and applied to the case of tropical cyclone Bejisa (2013–2014). The fully coupled OWA simulation shows good agreement with the literature and available observations. In particular, simulated significant wave height is within 30 cm of measurements made with buoys and altimeters. Short-term ($<$ 2 days) sensitivity experiments used to highlight the effect of oceanic waves coupling show limited impact on the track, the intensity evolution, and the turbulent surface fluxes of the tropical cyclone. However, it is also shown that using a fully coupled OWA system is essential to obtain consistent sea salt emissions. Spatial and temporal coherence of the sea state with the 10 m wind speed are necessary to produce sea salt aerosol emissions in the right place (in the eyewall of the tropical cyclone) and with the right size distribution, which is critical for cloud microphysics.

1. Introduction

Tropical cyclones (TC) are among the most devastating meteorological phenomena on Earth. They can be associated with precipitation, wind gusts, storm surges, flooding, and landslides as well as oceanic waves which can cause significant human and economic losses. Despite the considerable progress made over recent decades, intensity and, to some extent, trajectory forecasts still suffer from serious deficiencies. A possible way to improve TC forecasts is to take Ocean-Waves-Atmosphere (OWA) exchanges fully into account to better represent interactions between a TC and its environment.

Many recent studies have focused on the contribution of OWA coupling to tropical cyclone structure (e.g., Bao et al., 2000; Chen et al., 2007; Doyle, 2002; Liu et al., 2011; Warner et al., 2010; Zambon et al., 2014; Zhao et al., 2017). It has been shown that coupling the atmosphere with a 3-D oceanic model is essential to improve the accuracy of tropical cyclone intensity forecasts (Bender & Ginis, 2000). In particular, sea surface cooling under TC reduces the enthalpy fluxes and humidity convergence at the cyclone scale (Jullien et al., 2014; Smith et al., 2009), and so the tropical cyclone intensity growth. This cooling can be attributed to the extraction of heat by the TC (Emanuel, 1986; Holland, 1997; Rotunno & Emanuel, 1987), to strong upwelling and/or to asymmetric mixing provided by the oceanic momentum (e.g., Jullien et al., 2012; Price, 1981; Shay et al., 1989). It can also have an opposite effect. For example, as demonstrated by Lee and Chen (2014), by creating a stable boundary layer behind the cyclone, cooling can suppress convection in rainbands and enhance the transport of air with high energy into the inner core, thus, counterbalancing the expected loss of intensity.

In these studies, it has also been shown that oceanic waves play an important role in tropical cyclone intensity forecasts. As waves represent the dynamical interface of the ocean and the atmosphere, they are involved in the TC life cycle and air-sea exchanges. Oceanic waves drive the atmospheric turbulent fluxes as they modify the wind stress (e.g., Doyle, 2002; Kudryavtsev & Makin, 2007; Liu et al., 2011; Moon et al., 2007;

Wada et al., 2014). For example, Lee and Chen (2012) have shown that the wind-wave coupling deepens the inflow layer, thus increasing the TC intensity. It has also been shown that nonbreaking waves enhance the vertical mixing of the upper ocean (Breivik et al., 2015), which, in return, could modify the sea surface temperature cooling and therefore the tropical cyclone intensity (Aijaz et al., 2017).

Oceanic waves also play an important role through the emission of sea spray. Most studies about sea spray in tropical cyclones have focused on their impact on the ocean-atmosphere fluxes (Andreas & Emanuel, 2001; Bao et al., 2000; Fairall et al., 1994; Wang et al., 2001). One of the main roles of sea spray at high wind speed is to redistribute momentum in the near-surface layer, acting to slow down the near-surface wind speed (Andreas, 2004). This mechanism could be correlated with the saturation of the observed drag coefficient (Potter et al., 2015; Powell et al., 2003). Sea spray also releases water vapor by evaporation and loses sensible heat to the atmosphere, thus modifying the enthalpy fluxes (Richter & Stern, 2014; Wang et al., 2001). Recently, using a fully coupled Ocean-Waves-Atmosphere model, Zhao et al. (2017) focused on the effect of sea spray evaporation and found that sea spray led to an increase of typhoon intensity by enhancing the air-sea fluxes.

In addition, sea spray evaporates into sea salt aerosols which are one of the main sources of cloud condensation nuclei (CCN) in the marine environment (e.g., de Leeuw et al., 2011; Rosenfeld et al., 2014) over which tropical cyclones develop and evolve. Thus, such aerosols can also influence the tropical cyclone structure and intensity through cloud formation, lifetime, and precipitation (Fan et al., 2016; Herbener et al., 2014; Rosenfeld et al., 2012), and references therein). Recent findings also suggest that they could be a source of ice nucleating particles (DeMott et al., 2016; McCluskey et al., 2017; Wang et al., 2017; Wilson et al., 2015). Thus, a key point lies in the representation of their emission in numerical models. A review of sea salt aerosol source functions can be found in Grythe et al. (2014). The first parameterizations were mainly based on the 10 m wind speed (de Leeuw et al., 2011; Jaeglé et al., 2011; Monahan et al., 1986, among others). Recently, the sea surface temperature (Jaeglé et al., 2011), the sea surface salinity (Sofiev et al., 2011), and the sea state (Ovadnevaite et al., 2014) have also been taken into account. With the growing complexity of these parameterizations, it is necessary to use a consistent coupled system taking the interactions between the ocean, the waves, and the atmosphere into account online.

It is also essential to use a high-resolution ($<$ 5 km resolution) coupled system to explicitly represent deep convection which results in a better simulated structure of the tropical cyclone (Fierro et al., 2009; Gentry & Lackmann, 2010; Jin et al., 2014). Few OWA coupling studies using this grid resolution have been identified (Doyle et al., 2014; Jin et al., 2014; Lee & Chen, 2012).

The objective of this paper is twofold: (1) to present a new ocean-waves-atmosphere coupled system for high-resolution tropical cyclone studies, and (2) to show the importance of such a system in describing air-sea fluxes (momentum, heat, and aerosol) in tropical cyclones. This study focuses on the tropical cyclone Bejisa that developed in the south-west Indian Ocean and passed close to La Réunion in January 2014. Section 2 presents the evolution of Bejisa. The modeling strategy is described in section 3. Section 4 presents a description of the fully coupled ocean-waves-atmosphere simulation. Sensitivity of the tropical cyclone structure to oceanic waves coupling is presented in section 5, while the impact of oceanic waves on sea salt aerosols fluxes and concentration is shown in section 6. Finally, the conclusions are given in section 7.

2. Tropical Cyclone Bejisa (2014): An Overview

Bejisa was the fourth tropical storm of the 2013–2014 cyclone season in the south-west Indian Ocean. This tropical cyclone affected the islands of La Réunion and Mauritius in January 2014 (Figures 1 and 2). Since this basin is under the responsibility of the Regional Specialized Meteorological Center (RSMC) of La Réunion, the classification of RSMC La Réunion is used in this study. The intensity of storms is divided into four categories: Moderate Tropical Storm (MTS: $17 < v_{max} < 24$ m s^{-1}), Strong Tropical Storm (STS: $25 < v_{max} < 32$ m s^{-1}), Tropical Cyclone (TC: $33 < v_{max} < 43$ m s^{-1}), and Intense Tropical Cyclone (ITC: $v_{max} > 44$ m s^{-1}), where v_{max} is the 10 min averaged maximum wind speed.

On 27 December 2013, a low-pressure area developed north-east of Madagascar in the vicinity of the Farquhar Islands, a relatively unusual region for cyclogenesis. The convection started to become organized around this low-pressure area. A decrease in the east-southeast vertical wind shear and the favorable

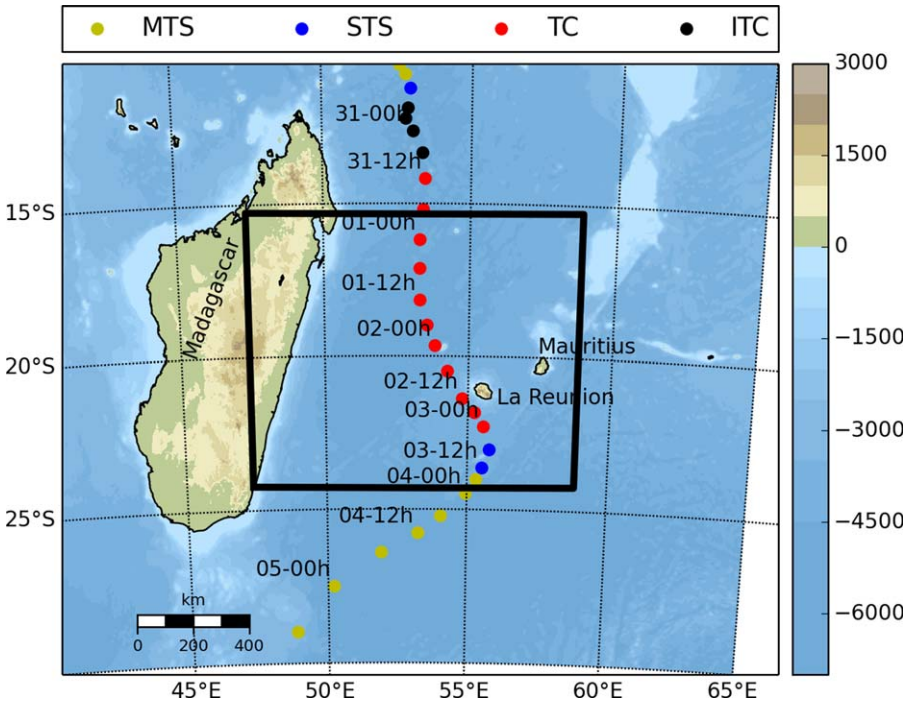

Figure 1. Orography and bathymetry (m; colors) in the domain, and best-track of Bejisa estimated by RSMC of La Réunion (colored dots). The green, blue, red, and black dots correspond to the intensity of Bejisa following the classification of RSMC La Réunion (see text for details): Moderate Tropical Storm (MTS), Strong Tropical Storm (STS), Tropical Cyclone (TC), and Intense Tropical Cyclone (ITC), respectively. The black box corresponds to the domain location for the Meso-NH, WW3 and CROCO models (cf., section 3).

altitude divergence resulted in this low-pressure system being classified as a Moderate Tropical Storm during the night of 29 December. As the vertical wind shear disappeared, the convection strengthened. A very rapid intensification phase started at 12 UTC on 29 December and lasted 24 h. This rapid intensification phase, favored by the small radius of the eye of the cyclone (diameter of about 10 km), was characterized by a 32.5 m s^{-1} increase of the 10 min averaged maximum wind speed and a deepening of the minimum central pressure by 47 hPa in 24 h, exceeding established rapid intensification thresholds (Kaplan et al., 2010). Thus, at 12 UTC on 30 December, Bejisa was classified as an Intense Tropical Cyclone with 48.9 m s^{-1} 10 min averaged maximum wind speed and 950 hPa minimum central pressure. On 31 December, as the eye diameter had increased to 25 km, the vertical wind shear started to increase while a large external rainband wrapped around the inner core of the system (Figure 2a). This eyewall replacement cycle was completed during the night. On 1 January, the cyclone was located 500 km north-northwest of La Reunion and

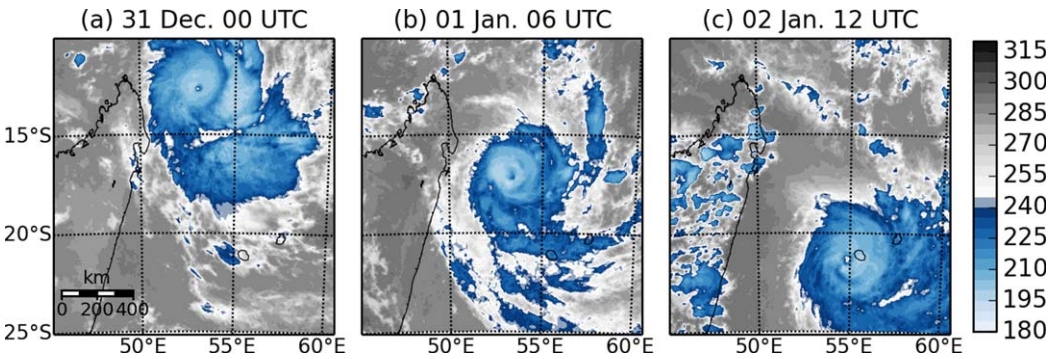

Figure 2. Brightness temperature (K) from (a) Meteosat IR channel at 00 UTC on 31 December 2013, (b) at 06 UTC on 1 January, and (c) at 12 UTC on 2 January 2014.

was propagating southward at 5.5 m s^{-1} (Figure 2b). During the next 24 h, Bejisa accelerated under the influence of a midaltitude ridge in the east. As the ridge weakened, Bejisa curved toward the south-east. On 2 January, a persisting weakness on the north to northeast side of the eyewall appeared on the scope of La Réunion radar. The radar images showed a strong instability of the eyewall while tropical cyclone Bejisa passed across the western side of La Réunion during the afternoon of 2 January (Figure 2c). The eyewall of Bejisa passed 10 km from the island at the closest. After passing La Réunion, the north-northwest part of the eyewall of Bejisa tore due to strong northwesterly winds at altitude. At 170 km to the south of La Réunion island, Bejisa was classified as a severe tropical storm and died out rapidly after turning south-southwest under the influence of a subtropical high-pressure cell located in the south of the system.

Its cyclogenesis region made Bejisa an unusual tropical cyclone that consequently affected the area (western and southwestern regions) of La Réunion. Wind gusts of less than 33 m s^{-1} were reported in the northern and eastern areas of La Réunion, and more than 41 m s^{-1} in the west and high areas of the island. The duration of the rainy period was short but intense accumulated rainfall was measured. More than 600 mm were reported in 48 h in the inner part of the island and up to 1,025 mm in Cilaos. The significant wave height of the wind and swell waves reached more than 7 m on the north-west coast of the island, which produced a strong storm surge and great damage along the west coast of the island and in the lagoon area. During this event, 180,000 people were left without electricity and 40% of the population did not have running water. The waves and river flooding caused significant damage to infrastructures in Saint Gilles. Part of the fruit production was damaged while most of vegetable crop was lost.

This study focuses on the period between 00 UTC on 1 January and 18 UTC on 2 January when Bejisa passed close to La Réunion. This period does not correspond to the most intense phase or to the rapid intensification phase but was chosen because of the interest of operational forecasts for understanding and preventing damage on La Réunion island and because of the availability of observations. It is the only period for which observations from radar, coastal buoys, and meteorological stations are available and can be used to evaluate the simulations.

3. Presentation of the Modeling System

Figure 3 shows the numerical MSWC (Meso-NH/SurfEx, WW3, and CROCO) system used in this study. These models were chosen because they can represent the fundamental processes involved in TC, from regional to coastal ones, and for deep to shallow waters. This coupling system is based on the multimodel coupling platform described in Voldoire et al. (2017), which has been extended to the use of the CROCO model. The

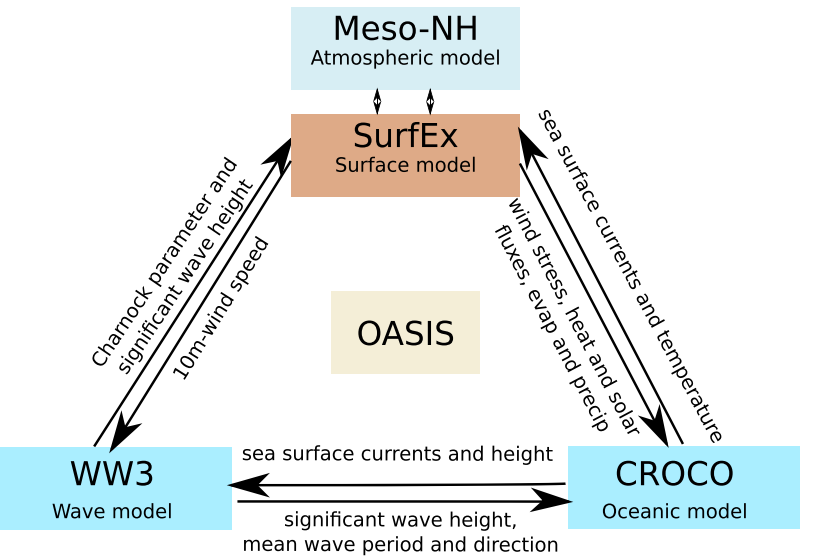

Figure 3. Schematic diagram of the coupling system. Fields exchanged among the atmospheric, wave, and oceanic models are also presented. All the parameters are exchanged at 10 min intervals.

main features and the configuration of each model are described in this section, along with the coupling strategy.

3.1. The Atmospheric Model: Meso-NH

Meso-NH is an atmospheric model developed by the Centre National de Recherches Météorologiques (Météo-France and Centre National de la Recherche Scientifique) and the Laboratoire d'Aérologie (Centre National de la Recherche Scientifique and University of Toulouse) (http://mesonh.aero.obs-mip.fr). It is a nonhydrostatic anelastic model, able to simulate the motion of the atmosphere, at scales ranging from synoptic (hundreds of kilometers) to microscale (tens of meters). Meso-NH has already been successfully used to simulate storms and tropical cyclones (Barthe et al., 2016; Chane-Ming et al., 2014; Jolivet et al., 2013; Nuissier et al., 2005; Pantillon et al., 2013, 2015, 2016).

Meso-NH has a large set of physical parameterizations to represent radiation, turbulence, clouds, precipitation, convection, chemistry, aerosols, etc. For the present study, the MNH-V5-3-0 package was used, and a simple set of physical parameterizations was chosen. The microphysics scheme (Pinty & Jabouille, 1998) was a single-moment bulk mixed-phase scheme predicting the mixing ratio of five microphysical species: cloud water, rain, cloud ice, snow, and graupel. A shallow convection parameterization based on mass-flux calculations (Bechtold et al., 2001) was used. The turbulence parameterization was based on a 1.5 order closure (Cuxart et al., 2000) with purely vertical turbulent flux computations using the mixing length of Bougeault and Lacarrère (1989). The radiative scheme was the one used at the European Center for Medium-Range Weather Forecasts (ECMWF; https://www.ecmwf.int/) (Gregory et al., 2010) including the Rapid Radiative Transfer Model (RRTM) parameterization for longwave radiation (Mlawer et al., 1997). The Organic Inorganic Log-normal Aerosol Model (ORILAM; Tulet et al., 2005) is used to simulate sea salt aerosol processes, such as emission, transport, sedimentation, and dry deposition. In this study, the sea salt aerosol size distribution consists of five log-normal modes: two modes for ultrafine sea salt aerosols (Aitken modes; radius < 0.05 μm), two others for fine sea salt aerosols (Accumulation modes; 0.05 μm $<$ radius $<$ 0.5 μm), and an other one for coarse sea salt aerosols (Coarse mode; radius > 0.5 μm). These five log-normal modes are described by the sea salt aerosols number concentration (the number median radius and geometric standard deviation being held constant). Note that the effect of sea salt aerosols on cloud microphysics is not considered in this paper.

The surface-atmosphere interactions are grouped on a surface modeling platform, called SurfEx (Surface Externalisée in French; Masson et al., 2013; Voldoire et al., 2017). Various physical models compose SurfEx to account for natural land surface, urbanized areas, lakes, and oceans. It can be used in standalone mode or coupled to various models (ocean, oceanic waves, river, etc.). The SurfEx platform used in this study included the ISBA (Interaction Soil-Biosphere-Atmosphere; Noilhan & Planton, 1989) model, a land surface model with three soil layers by default, and the COARE (Coupled Ocean-Atmosphere Response Experiment, Fairall et al., 2003) parameterization of sea surface fluxes. This parameterization allows coupling with oceanic waves (see section 3.4).

The sea salt aerosol emission parameterization used in this study was based on that of Ovadnevaite et al. (2014) and was implemented in Meso-NH/SurfEx by Claeys (2016). This is the only parameterization that takes account of a wide range of parameters that influence the emission of sea salt aerosols: the 10 m wind speed, the significant wave height and the water viscosity through the sea surface temperature and salinity. Traditionally, sea salt aerosol emissions are parameterized by 10 m wind speed alone but the dependence of the aerosol concentration on the sea-state is evident and was confirmed recently by Lenain and Melville (2017).

The Meso-NH/SurfEx domain covers an area of 1,200 km $\times$ 1,000 km with a horizontal grid spacing of 2 km. This grid length enables deep convection to be explicitly represented, which results in a better simulated structure of the tropical cyclone (Fierro et al., 2009; Gentry & Lackmann, 2010). The vertical grid has 70 stretched levels with enhanced resolution close to the ground and in the outflow region. Associated with the leapfrog temporal scheme, momentum variables were advected with a centered fourth-order scheme, while scalar and other meteorological variables were advected with a monotonic Piecewise Parabolic Method to ensure positive values (Colella & Woodward, 1984). The time step of Meso-NH is 3 s. The simulations were performed from 00 UTC on 1 January 2014 to 18 UTC on 2 January 2014. Meso-NH/SurfEx was initialized at 00 UTC with AROME-IO analysis. AROME-IO is the AROME-Indian Ocean configuration of the

operational Météo-France model AROME. Meso-NH/SurfEx was forced at the lateral boundaries by the 6 h-ECMWF operational high-resolution analysis.

3.2. The Wave Model: WW3

The wave model WW3 (WAVEWATCH3; http://polar.ncep.noaa.gov/waves/wavewatch/; Tolman, 1992; The WAVEWATCH III Development Group, 2016) solves the random phase spectral action density balance equation for selected wavenumber-direction spectra. The effects of wind-wave interactions, nonlinear wave-wave interactions, wave-bottom interactions, depth-induced breaking, dissipation, and reflection off the shoreline are parameterized. For the present study, the third-order Ultimate Quickest scheme by Tolman (2002) with the Garden Sprinkler correction was used to avoid this numerical artifact due to the discrete directions of wave propagation. Nonlinear wave-wave interactions were modeled using the Discrete Interaction Approximation (DIA, Hasselmann et al., 1985). The wind-wave interaction source term of Ardhuin et al. (2010) was used. This parameterization is built around a saturation-based dissipation, reducing the unrealistically large drag coefficients under high winds. Additionally, depth-induced wave breaking (Battjes & Janssen, 1978) and bottom friction source terms (Ardhuin et al., 2003) were used. Finally, reflection by shorelines described in detail in Ardhuin and Roland (2012) was also activated.

The grid covered the same area as Meso-NH/SurfEx with 692 × 578 points and a spatial resolution of 1/60° (∼1.7 km). The global time step of WW3 was 100 s. The spectral discretization of WW3 was 24 for the direction (every 15°) and 32 for the frequency. Along the track of tropical cyclone Bejisa, the ocean depth was roughly 4,000 m. Thus, the shallow water parameterizations were only useful close to the shoreline. A stand-alone WW3 run of 3 days, from 00 UTC on 28 December 2013 to 00 UTC on 1 January 2014 was set up to downscale from global MARC (Modélisation et Analyse pour la Recherche Côtière) hindcast (http://marc.ifremer.fr/) to our simulation domain. The horizontal resolution of the MARC hindcast is 0.5° and the spectral discretization is 24 for the direction (every 15°) and 32 for the frequency. The 10 m wind speed used to force the MARC hindcast and the stand-alone WW3 run came from the ECMWF operational high-resolution analysis. The new spectra from the stand-alone WW3 run were imposed every 3 h at the boundaries of WW3 in the coupled simulations.

3.3. The Oceanic Model: CROCO

The ocean was modeled with the Coastal and Regional Ocean COmmunity model (CROCO; http://www.croco-ocean.org). CROCO is a new model built upon ROMS-Agrif (Debreu et al., 2012; Penven et al., 2006). It includes more and more capabilities, such as OWA coupling. It is a free-surface, terrain-following coordinate model with split-explicit time stepping. It solves the incompressible primitive equations based on the Boussinesq and hydrostatic approximations and is coupled to advection-diffusion schemes for potential temperature and salinity as well as a nonlinear equation of state for density. The advection scheme is third-order upstream biased, which reduces dispersion errors, essentially enhancing precision for a given grid resolution (Shchepetkin & McWilliams, 1998). Subgrid-scale vertical mixing is introduced by the nonlocal K-profile parameterization (KPP) scheme (Large et al., 1994). The bottom stress is computed using a simple linear formulation with a constant bottom drag coefficient set to $C_d = 3.10^{-4}$. Coupling with oceanic waves is described in Marchesiello et al. (2015).

The grid covers the same area as WW3 and Meso-NH/SurfEx and with the same resolution as WW3, i.e., 1/60° (∼1.7 km) with 692 × 578 points. The temporal scheme used is a time-splitting scheme with chosen baroclinic and barotropic time steps of 100 and 2 s, respectively. The bathymetry is constructed from the GEneral Bathymetric Chart of the Oceans global bathymetry (GEBCO; available online at http://www.gebco.net). To avoid pressure gradient errors induced by terrain-following coordinates in shallow regions with steep bathymetric slope (Beckmann & Haidvogel, 1993), a local smoothing of the bottom topography is applied where the steepness of the topography exceeds a factor $r = \nabla h/h$ of 0.25 (where h is the depth). The domain has 32 vertical levels, with enhanced resolution near the surface. The original vertical grid stretching formulation described in Song & Haidvogel (1994) is used.

The model is initialized and forced at its boundaries using the 3 day ECCO2 reanalysis (Estimating the Circulation and Climate of the Ocean: Phase 2, Menemenlis et al., 2008) at 00 UTC on 1 January 2014. Figure 4a shows the sea surface temperature from the ECCO2 analysis used as an initial condition for all the simulations. The colored squares represent the sea surface temperature (SST) measured by drifting buoys from the

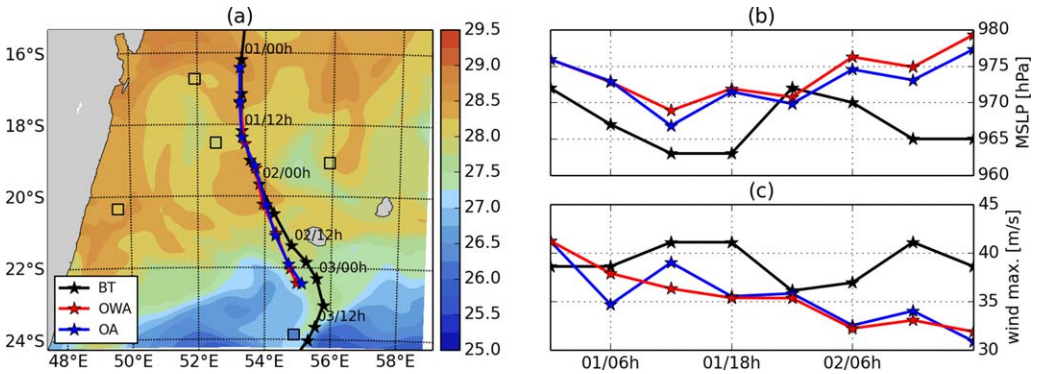

Figure 4. (a) SST (°C, colors) from the OWA simulation and from drifting buoys (WMO database; color squares) at 00 UTC on 1 January, and track of Bejisa (lines with stars). (b) Evolution of the minimum mean sea level pressure (MSLP, in hPa). (c) Evolution of the maximum sustained wind speed (in m s^{-1}). The black, red, and blue lines represent the best-track, and the OWA, and OA simulations, respectively. Each star corresponds to data at a 6 h interval.

WMO (World Meteorological Organization) database at the same time. Overall, the sea surface temperature observed by the drifting buoys is well reproduced by the analysis. A latitudinal gradient is shown in the sea surface temperature pattern, going from hotter sea surface temperatures in the north (∼29°C at 16°S) to colder ones in the south (∼26°C at 24°S). The difference between the ECCO2 analysis and the drifting buoys in the south of the domain is higher than in the north, where the sea surface temperature pattern is better reproduced. Overall, the sea surface temperature from the ECCO2 analysis reproduces the sea surface temperature from drifting buoys with less than a ∼0.2°C difference, making this analysis suitable to initialize the oceanic model.

3.4. Coupling Strategy

OASIS (Ocean Atmosphere Sea Ice Soil, Craig et al., 2017) was used to couple the oceanic, waves, and atmospheric models. The current OASIS3-MCT version is interfaced with the Model Coupling Toolkit (MCT, Jacob et al., 2005; Larson et al., 2005) and with the Spherical Coordinate Remapping Interpolation Package (SCRIP, Jones, 1999). OASIS3-MCT is fully parallelized, allowing very good computational performance. The variables that are exchanged between the various models are shown in Figure 3.

In SurfEx, turbulent fluxes at the sea surface are computed using the sea surface temperature (SST; K) and the two components of the sea surface currents (m s^{-1}) from CROCO. These parameters are used to compute the stability of the atmosphere and the relative wind. The Charnock parameter (α; dimensionless) (Charnock, 1955) from WW3 is also needed. In WW3, the Charnock parameter is computed using the Janssen (1991) formulation $\alpha = 1/\sqrt{1-\tau_w/\tau}$, with τ_w the wave-induced stress including the resolved part of the spectrum and τ the total stress. The Charnock parameter is used in SurfEx to compute the roughness length formulation (z_0; m) following Smith (1988):

$$z_0 = \alpha \frac{u_*^2}{g} + 0.11 \frac{\nu}{u_*}, \tag{1}$$

where ν is the cinematic viscosity of the air (15.6×10^{-6} m^2 s^{-1} at the ground) and g the gravitational acceleration (9.81 m s^{-2} at the ground). u_* is the friction velocity (m s^{-1}) defined as:

$$u_* = u \frac{\kappa}{\ln\left(\frac{z}{z_0} - f\left(\frac{z}{L_{MO}}\right)\right)}, \tag{2}$$

where κ, u, and z are the Von Kàrmàn constant (dimensionless value of 0.4), the relative wind speed (difference between the wind speed at the first level and the sea surface currents from CROCO) (m s^{-1}) and the height (m), respectively. $f(z/L_{MO})$ is a stability function based on Monin-Obukhov theory (dimensionless) and L_{MO} is the Monin-Obukhov length (m). These equations are solved using an iterative method. After convergence (less than five iterations), z_0 and u_* are used to compute the transfer coefficients, a component of the turbulent surface fluxes, which are the surface boundary conditions of the Meso-NH model. Without wave coupling, the Charnock parameter depends on the 10 m wind speed (Hare et al., 1999):

$$\alpha = 0.011 \quad \text{if} \quad u < 10 \text{ m s}^{-1},$$
$$\alpha = 0.011 + 0.007\frac{u-10}{8} \quad \text{if} \quad 10 \text{ m s}^{-1} < u < 18 \text{ m s}^{-1}, \tag{3}$$
$$\alpha = 0.018 \quad \text{if} \quad u > 18 \text{ m s}^{-1}.$$

Such a parameterization takes into account the oceanic waves by (1) increasing the Charnock parameter linearly with wind between 0.011 and 0.018 (increasing steepness of the waves with wind speed) and (2) saturating the Charnock parameter at high winds (impact of wave breaking and sea spray). Sensitivity experiments, made in this study and presented in section 3.5, investigate the impact of using a Charnock parameter computed from the wave model against such a parameterization.

Sea salt aerosol fluxes are computed using the significant wave height, H_s, from WW3 and SST from CROCO. Note that the effects of sea salt on turbulent air-sea fluxes and on cloud microphysics are not considered in this paper and will be addressed in a future study.

The wind-waves parameterization of Ardhuin et al. (2010) in WW3 is computed using the two components of the 10 m wind speed from SurfEx and the two components of the sea surface currents and sea surface height from CROCO. It must be noted that WW3 computes its own momentum flux using the 10 m wind speed from SurfEx. This computation is based on a bulk formulation under neutral atmospheric conditions and a subtle balance between wave growth and wave dissipation. Therefore, consequent changes in WW3 source term parameterization would be necessary to use SurfEx wind stress instead of 10 m wind speed. This will be done in a future study. The inconsistency between SurfEx and WW3 momentum flux is evaluate to be about 10% in very localized high wind speed maxima and less than a few percentages around (not shown here).

Surface boundary conditions of the oceanic model use the solar flux, the net heat flux, and the evaporation and precipitation terms from SurfEx. Momentum flux is also prescribed from SurfEx directly. Wave-to-ocean momentum flux is computed in WW3 but as an inconsistency exists between WW3 and SurfEx momentum formulation, it has been considered that SurfEx flux was more accurate as it takes into account all the atmospheric boundary layer processes. Another possibility would have been to prescribe as surface stress the wave to ocean momentum flux (computed from WW3) plus the remaining stress not used for wave growth (SurfEx stress minus WW3 stress). This has been tested and gave very similar results than prescribing directly SurfEx wind stress (not shown here). The wave-ocean interaction terms (Marchesiello et al., 2015) like the Stokes drift and the nonbreaking waves induced mixing following Uchiyama et al. (2009) are computed using the from WW3.

All models used in this study (Meso-NH/SurfEx, WW3, and CROCO) had the same domain location (see the black box in Figure 1). All surface fields were exchanged every 10 min and were interpolated from grid to grid through distance weighted nearest-neighbor interpolation with four neighbors using OASIS libraries.

3.5. Set of Experiments

A set of seven experiments was performed (Table 1) to highlight the impact of oceanic waves on the tropical cyclone evolution and on the sea salt aerosol emissions. The reference experiment was the fully coupled Ocean-Waves-Atmosphere (OWA) simulation where all the fields were exchanged. Sea salt aerosol fluxes were computed from the Ovadnevaite et al. (2014) parameterization described in section 3.1 and used the significant wave height (H_s) from WW3.

Table 1
List of Numerical Experiments

Experiments	WW3 coupling	H_s used in the sea salt aerosol fluxes parameterization
OWA	X	H_s from WW3 (online coupling)
OA		
OWA_2m	X	H_s homogeneous, constant, and equal to 2 m
OWA_9m	X	H_s homogeneous, constant, and equal to 9 m
OWA_MARC	X	H_s from MARC global hindcast
OWA_FORC	X	H_s from WW3 stand-alone run (offline coupling)
OWA_ERAI	X	H_s from ERA-Interim

Six additional simulations were performed. The first sensitivity experiment was the Ocean-Atmosphere (OA) simulation, where the wave model was removed and the Charnock parameter was computed using the Hare et al. (1999) parameterization (equation (3)). The impact of oceanic waves coupling (comparison between the OWA and OA simulations) is presented in section 5.

The other five simulations were similar to the OWA simulation but the significant wave height (H_s) used in the sea salt aerosol flux computation was different. For the OWA_2m and OWA_9m, the H_s used in the sea salt aerosol fluxes is homogenous, constant, and equal to 2 and 9 m, respectively. These values were chosen because they represent the minimum and maximum values encountered in the spatial

distribution of H_s in the OWA simulation (see section 4.3). For the OWA_ERAI experiment, the H_s used in the sea salt aerosol fluxes were extracted from the ERA Interim reanalysis (Berrisford et al., 2011). ERA-Interim data are a global atmospheric reanalysis with a spatial resolution of approximately 80 km. The horizontal resolution of these data is low but they are the only data that can be accessed via the public server of the ECMWF. For the OWA_MARC experiment, the H_s used in the sea salt aerosol fluxes was extracted from the MARC hindcast described in section 3.2. For the OWA_FORC experiment, the H_s used in the sea salt aerosol fluxes was extracted from a stand-alone WW3 run at the same resolution as the OWA simulation. This stand-alone WW3 run was forced by the 10 m wind speed of the ECMWF operational high-resolution analysis. The impact of the significant wave height on sea salt aerosol fluxes and concentration is presented in section 6.

4. Description of the Fully Coupled OWA Simulation

The aim of this section is to describe and evaluate the fully coupled OWA simulation with available observations and the literature. Best-track data are used for the evaluation of the TC track and intensity (section 4.1), buoys, and altimeters for the evaluation of the sea state (section 4.3), and drifting buoys for the evaluation of the sea surface temperature (section 4.4).

4.1. Track and Intensity

The cyclone track and intensity from the OWA simulation and from the Best-Track (BT) of RSMC La Réunion are shown in Figure 4. Best-track data are the best estimate of the characteristics of Bejisa using all the observations and models available. It includes the position (latitude and longitude) and the intensity (mean sea level pressure and maximum sustained wind speed) of the storm at 6 h intervals.

The OWA simulation (red line) reproduces the best-track (black line) closely until 00 UTC on 2 January. After that, the simulated cyclone accelerates, following a south-south-eastern direction while the observed storm moves more slowly toward the south-east. Consequently, the simulated system is located 60–70 km northwest of the estimated position of the analyzed system on 2 January between 06 UTC and 12 UTC. At the end of the simulation, the simulated cyclone decelerates as already described in section 2. Figures 4b and 4c show the temporal evolution of the minimum value of the mean sea level pressure (MSLP) and the maximum sustained wind speed, respectively. Overall, the simulated tropical cyclone is less intense than the best-track one. At the beginning of the simulation, the MSLP in the model is 976 hPa, close to the MSLP in the AROME-IO analysis (975 hPa), while the best-track MSLP is 972 hPa. The trend of the MSLP and the maximum sustained wind speed is fairly well reproduced by the model on 1 January. Starting from 00 UTC on 2 January, the intensity diverges between the simulation and the best-track. The intensity in the OWA simulation decreases by 9 hPa and 6 m s^{-1} in 18 h, while the intensity of the best-track increases by 7 hPa and 5 m s^{-1}, during the same period. Despite an underestimation of its intensity probably associated to an underestimation already present in AROME-IO initialization field, the position of Bejisa and the temporal changes of its intensity are fairly well reproduced by the OWA simulation: maximum error (before the divergence of the tracks) of 7 hPa and 6 m s^{-1} for a cyclonic system reaching 963 hPa and 41 m s^{-1}.

4.2. 10 m Wind Speed

The horizontal structure of the simulated OWA cyclone is described through the temporal evolution of the 10 m wind speed (Figures 5a, 5c, and 5e). Note that the quadrants are defined with respect to the tropical cyclone's motion: the left quadrants mean to the east of the TC. This convention is used in the following.

At 18 UTC on 1 January (Figure 5a), the eye of the cyclone is clearly visible with a weak 10 m wind region (less than 10 m s^{-1}). The surrounding eyewall exhibits the maximum 10 m wind speed ($>$ 36 m s^{-1}) in the left and right quadrants of the system. At 06 UTC on 2 January (Figure 5c), the simulated system is located as close as possible to La Réunion. Its intensity has decreased (Figure 4b) and the region of maximum 10 m wind speed ($>$ 30 m s^{-1}) is now located in the front left quadrant of the system and is close to La Réunion ($\sim$50 km). The northern part of the eyewall shows a relative weakness with 10 m wind of less than 27 m s^{-1}. At 18 UTC on 2 January (Figure 5e), Bejisa is partially broken in its northwestern region as observed (see section 2), inducing a strong asymmetry of the 10 m wind speed. It barely exceeds 27 m s^{-1} at some very localized points. Overall, the TC simulated by the OWA simulation reproduces the horizontal structure and the main behavior of tropical cyclone Bejisa, as described in section 2.

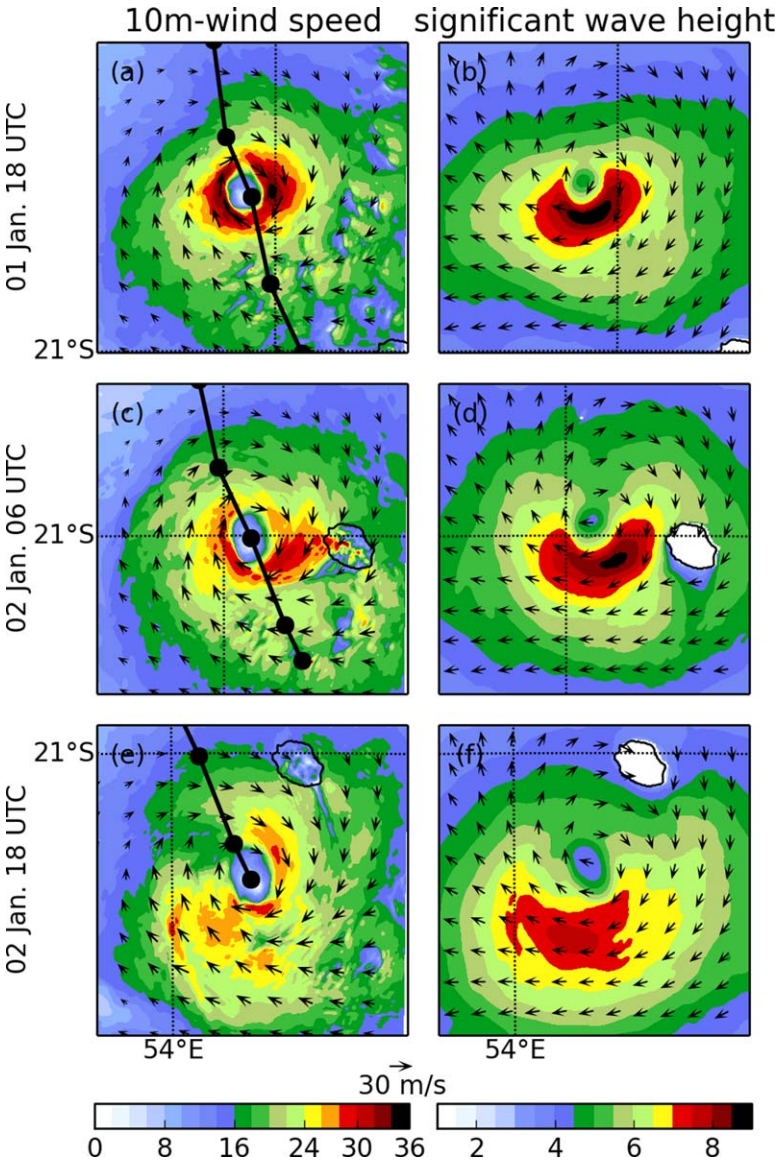

Figure 5. (left plots) 10 m-wind speed (m s^{-1}; colors) and (right plots) significant wave height for wind and swell waves (m; colors) at 18 UTC on 1 January (first row), at 06 UTC on 2 January (second row), and at 18 UTC on 2 January UTC (third row) for the OWA simulation. Black arrows correspond to the 10 m-wind speed vectors and to the wave direction in the left and right columns, respectively.

4.3. Significant Wave Height

Significant wave height is one of the key parameters involved in storm surge but also in oceanic mixing, and in the sea salt aerosol source function (section 3). In this section, H_s simulated by the OWA simulation is evaluated through comparisons with buoy and altimeter data.

Figures 5b, 5d, and 5f show the temporal evolution of the H_s in the OWA simulation. Overall, the main oceanic waves (Figures 5b, 5d, and 5f) are localized under the cyclone eyewall (Figures 5a, 5c, 5e), meaning that they are directly generated by the cyclonic wind and are not advected from outside the simulation domain. At 18 UTC on 1 January, the main wave packet has a maximum value of H_s higher than 8 m, located in the front quadrants of the cyclone. This wave packet propagates to the south with a bean-like structure. This is well-known behavior for waves associated with tropical cyclones, based on theoretical considerations (Cline, 1920), numerical modeling (Chen & Curcic, 2016; Moon et al., 2003) and in situ observations from ships (Tannehill, 1936), airplane (Wright et al., 2001), and buoy measurements (Esquivel-Trava et al., 2015).

This shape results from the higher wind speed in the quadrant associated with the forward motion of the storm. An additional mechanism is the increase of the effective fetch and the duration of the wave-growth process in the direction of the motion of the storm (Wright et al., 2001). Twelve hours before the cyclone reaches La Réunion, oceanic waves with H_s of about 3–4 m touch the northern side of the island. The wave direction turns clockwise, like the main wind direction. As noted by Wright et al. (2001), the dominant waves propagate at a more or less large angle to the 10 m wind. In the right quadrants of the system, this angle is maximum. When the cyclone is close to the western coast of La Réunion (Figure 5d), the maximum of significant wave height is close to 9 m. After passing La Réunion island, H_s decreases at the same time as the cyclone intensity (Figures 5e and 5f). Since the oceanic waves also propagate to the north, behind the cyclone, the southern side of La Réunion is impacted by the swell several hours after the passage of the cyclone (Figure 5f). Analyzing the microseismic noise using permanent and nonpermanent seismic stations, Davy et al. (2016) showed that microseismic noise was still giving a recordable signal when Bejisa was located south of the island confirming the presence of northward swell after the passage of the TC.

To evaluate the H_s simulated by the OWA simulation, a comparison with buoy data is made and presented in Figure 6. Direct observations are available from nondirectional ocean wave gauges of the CANDHIS (Centre d'Archivage National de Données de Houle In Situ; http://candhis.cetmef.developpement-durable.gouv.fr/) network (CANDHIS_97403) and from two buoys (NRL_RN2 and NRL_RN4) that were temporarily installed on the north-west shore of La Réunion (Figure 6a).

Three different stages can be distinguished on each site. From 00 to 22 UTC on 1 January, the storm is located north of the island and relatively far from it, and H_s is increasing slightly on the north of the island. At the beginning of the simulation, H_s is between 1 and 1.2 m in the model, and between 0.8 and 1 m in the observations. It increases by approximately 2 m in 22 h both in the observations and in the model. During this first stage, the model is in very good agreement with observations. From 22 UTC on 1 January to 06 UTC on 2 January, Bejisa is approaching La Réunion, and H_s increases significantly (1.5–2 m in 8 h). In the simulation, the maximum of H_s is reached at 06 UTC on 2 January for the NRL_RN2 (5.8 m) and NRL_RN4

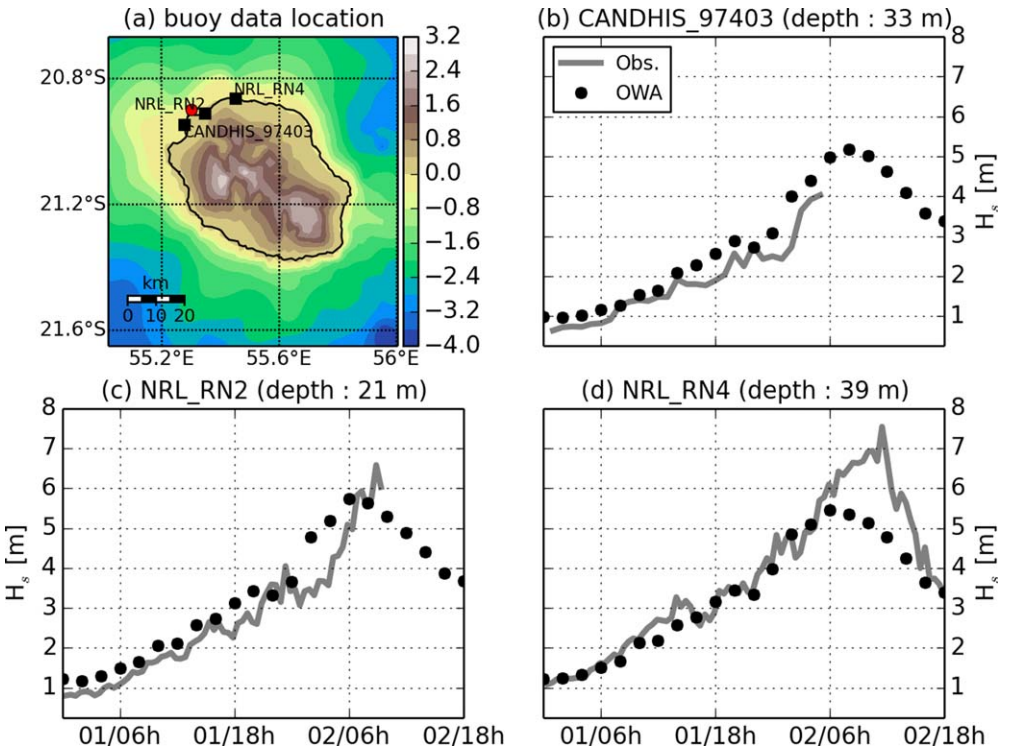

Figure 6. (a) Position of the three buoys (black squares) and bathymetry/orography (km; colors) around La Réunion. The red dot corresponds to Pointe des Galets. Evolution of the H_s (m) at the (b) CANDHIS_97403, (c) NRL_RN2, and (d) NRL_RN4 buoy locations. The gray line shows the observations while the black dots display the results of the OWA simulation.

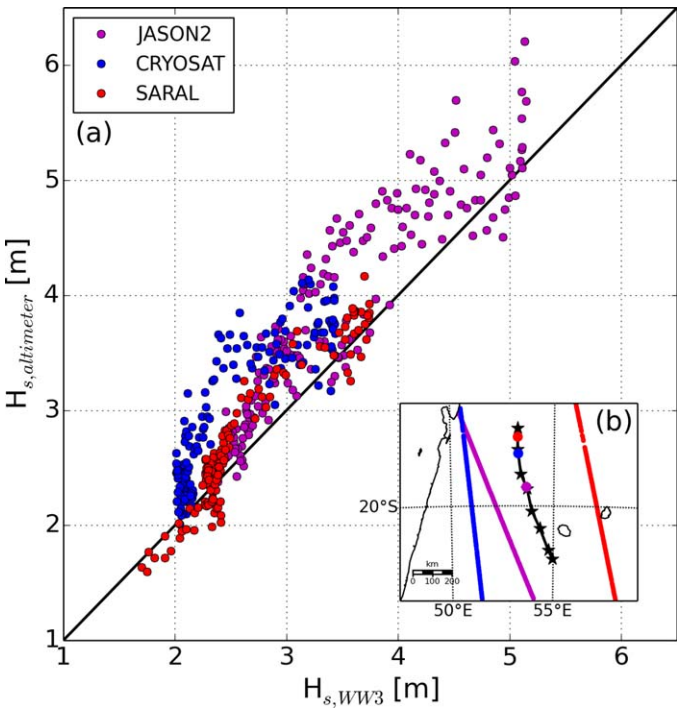

Figure 7. (a) Scatterplot of the significant wave height (m) from altimeters versus collocated significant wave height (m) from the OWA simulation. (b) Location of the satellite tracks in the domain location. Black stars correspond to the simulated track of the OWA simulation, every 6 h from 00 UTC on 1 January to 18 UTC on 2 January. Color dots correspond to the position of the simulated TC at the different altimeters crossing times (Jason-2 at 17 h 15 min UTC on 1 January, Cryosat: 7 h UTC on 1 January and Saral at 2 h 30 min UTC on 1 January). Each satellite crosses the domain in approximately 2 min.

(5.5 m) buoys, and 2 h later for the CANDHIS_97403 buoy (5.1 m). Note that the CANDHIS_97403 and NRL_RN2 buoys broke during the cyclone and did not measure the wave peak. For the remaining NRL_RN4 buoy, the model differs from the buoy data concerning the time and value of the peak of H_s. It is 5 h in advance in the simulation (06 UTC on 2 January) compared to the observations (11 UTC on 2 January). This is in agreement with a simulated system traveling faster than the observed one (Figure 4). Moreover, the simulated peak of H_s (5.5 m) is lower than the observed one (7.6 m). This is in agreement with the larger distance of the center of Bejisa from La Réunion in the simulation (∼70 km) compared to the best-track (∼50 km; Figure 4a). This could also be explained by (i) the low-resolution of the wave model that does not resolve the shallow water processes in the vicinity of the coast well (the depth at buoys location is less than 40 m for observations and close to 100 m for OWA simulation), (ii) the proximity of the buoys to the coast (less than 1 km off the coast), and (iii) the 1.7 km resolution of the wave model, which that makes comparison with these buoys delicate. During the third stage, Bejisa is moving away from the island, and the northern coast is becoming more and more protected from the cyclonic swell, leading to a decrease in H_s. The maximum H_s for the CANDHIS_97403 buoy is lower than for the other two buoys although Bejisa passed closer to this buoy. In fact, it was relatively protected by Pointe des Galets (red dot in Figure 6), and the plateau west of the buoy increased the friction, and consequently the wave breaking, leading to lower values of H_s.

To assess the simulated H_s from the OWA simulation, a comparison is also made with the data from altimeters (in Figure 7 and Table 2).

The merged and calibrated altimeter data set of Queffeulou and Croizé-Fillon (2017) is used in this study. Data from the Cryosat, Jason-2, and Altika Saral missions are available for the relevant period and region of interest and are presented in Figure 7b. Only the altimeter data in the offshore areas (further than 50 km from the coast) were taken into account, as comparisons with coastal buoy measurements indicated biases and errors in the altimeter measurements (Shanas et al., 2014), especially because of the large antenna footprint. The three altimeters' bands cover an area localized around the TC (more than 100 km from the TC center; Figure 7b), which allows an evaluation of the deep water external region of the TC. There, the H_s is not maximum and not influenced by the shallow water processes. Standard error statistics are computed to have a quantitative assessment of the OWA simulation. These statistics include the correlation coefficient (R), the bias (bias), and the root mean square error (rmse; Table 2).

The correlation coefficient is close to 1 (0.99) for all altimeter data. This means that temporal and spatial variability of the simulated H_s are highly correlated with the H_s measured using the altimeters. Regarding the bias, the simulated significant wave height is underestimated by 34 cm (less than 10%) compared to the altimeter measurements (Table 2). However, some discrepancies between altimeters can be noted. This bias is higher for comparisons with Cryosat and Jason-2 (respectively, 43 and 48 cm) which is consistent with the underestimation of the simulated H_s under TC, shown in Figure 6. Comparison of the simulated H_s with Saral altimeter shows a weaker bias of less than 11 cm (3.5%). At the time and location of Saral measurement, the simulated H_s is not yet influenced by oceanic waves generated by the simulated TC but only by preexisting wave field. This could explain the lower bias of the simulation compared to Saral than to other altimeters. Spreading of the data is now evaluated with the rmse. For Cryosat and Jason-2, the rmse is 57 cm while it does not exceed 23 cm for the Saral Altimeter. This shows that the H_s error

Table 2
Statistical Metrics (Correlation Coefficient (R), bias, rmse) of Differences Between H_s From Altimeters and OWA Simulation

Satellite	Jason-2	Cryosat	Saral	All
R	0.99	0.99	0.99	0.99
bias (cm)	−43	−48	−11	−34
rmse (cm)	57	57	23	46

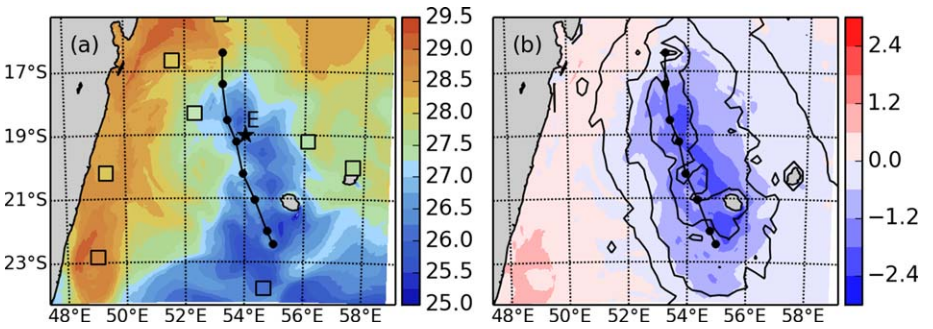

Figure 8. (a) SST (°C, colors) from the OWA simulation and drifting buoys (colored squares) at 18 UTC on 2 January. (b) Difference between the SST at 18 UTC on 2 January and at 00 UTC on 1 January (Figure 4a). The black line with dots corresponds to the track of the cyclone in the OWA simulation. In plot (b), the black contours correspond to the mean momentum flux during the OWA simulation (contours at 0.2, 0.4, and 0.8 kg m^{-1} s^{-2}). The black star on plot (a) (point (E)) is the point where vertical profiles of temperature and currents were extracted.

does not deviate by more than 60 cm from the regression line, leading to the conclusion that simulated H_s variability is in quite good agreement with H_s variability from satellites.

Overall, the significant wave height simulated by the OWA simulation is in good agreement with buoy and satellite observations, with a difference of less than 10% for big waves.

4.4. Sea Surface Temperature

Sea surface cooling under a tropical cyclone is one of the air-sea coupling processes involved in tropical cyclone evolution. To evaluate the simulated sea surface cooling, the final SST of the OWA simulation is presented in Figure 8a.

A colder SST region (26–27°C) clearly appears along the track of Bejisa, while the SST in the surrounding waters is higher than 27.5°C north of 22°S. The simulated SST is in good agreement with the data from the drifting buoys (WMO database) in the external part of the cold wake. For each buoy, less than 0.25°C difference is reported between the observation and the simulation. The difference in the SST between the end (18 UTC on 2 January) and the beginning (00 UTC on 1 January) of the simulation is shown in Figure 8b. Because of the asymmetric wind stress forcing, the SST cooling is highly asymmetric and is maximum on the left quadrants. The sea surface temperature measured from satellites exhibits this same qualitative structure but the presence of clouds makes the comparison with this simulation difficult and it is not shown here. Two combined effects explain this asymmetry. First, the addition of the strong tangential winds on the left side of the system combined with the translation speed induces more wind stress and increases oceanic vertical mixing. In addition, currents are also increased by inertial resonance, localized at the same place, with the winds. These processes result in a cooler SST on the left side of the TC and contribute to the asymmetry of the system. They have been largely modeled and observed (D'Asaro et al., 2007; Jullien et al., 2012; Price, 1981). Along the entire cyclone track, the SST cools by more than 0.6°C over a distance of 200 (100) km on the left (right) side of the system. It can be seen that the 0.4 kg m^{-1} s^{-2} contour of the mean momentum flux is well collocated with the −0.6°C cooling rate. The maximum cooling is between 1.8 and 2.4°C and persists for more than 24 h after the passage of Bejisa. It occurs in a 40 km wide band centered 50–100 km left of the system.

4.5. Oceanic Boundary Layer Evolution

To explain the SST cooling visible in Figure 8, the temporal evolution of the thermocline and of the oceanic currents was examined. Vertical profiles were extracted at the point (E) shown by a black star in Figure 8a. This point was located in the region where cooling was maximum and upstream of La Réunion to highlight the response of the thermocline after the passage of Bejisa. Figure 9 shows the temporal evolution of the mean sea level pressure and of the vertical profiles of temperature and currents extracted at this point.

For the first 15 h, the system is north point E (Figure 8a). The SST is around 28°C and the thermocline is located at 55–60 m depth (Figure 9b). Between 15 and 25 h of simulation, while the storm passes close to the point E (where the MSLP is minimum in Figure 9a), the SST decreases from 28°C to less than 26.5°C. It

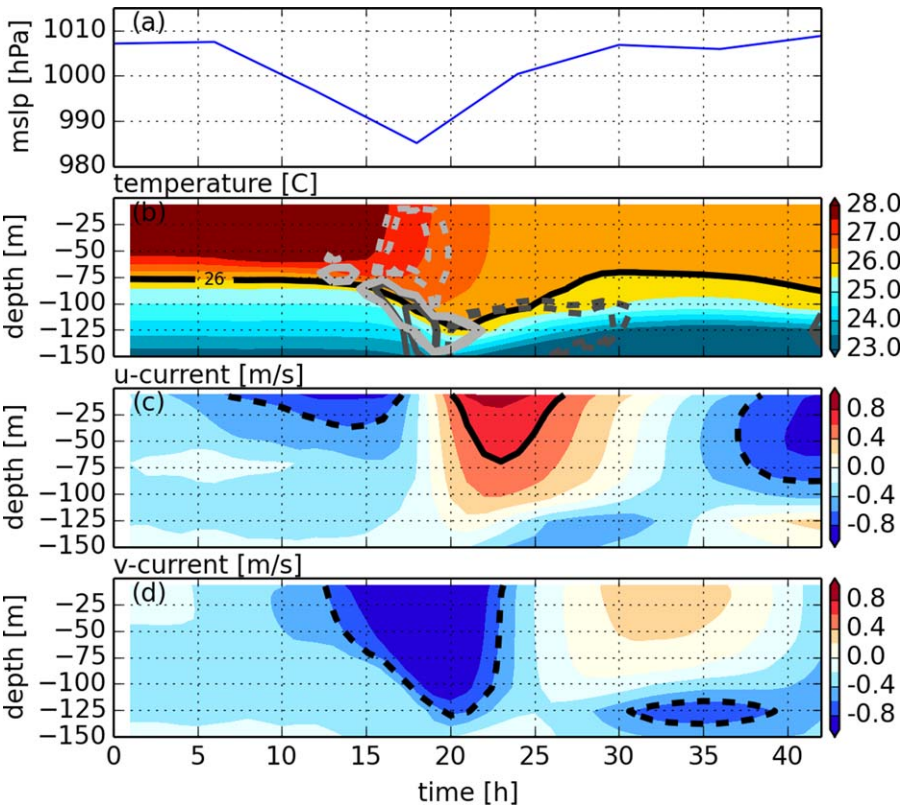

Figure 9. Time series of (a) the mean sea level pressure (MSLP; hPa), and of the vertical profiles of (b) the oceanic temperature (°C), and (c) the *u*, and (d) *v* components of the oceanic current (m s^{-1}). In plot (b), the 26°C isotherm is drawn with a black isoline. The dashed and solid contours correspond to the −4, −3, 3, and 4°C d^{-1} isolines for the vertical mixing (light gray) and total advection terms (dark gray) of the temperature budget, averaged over 1 h. In plots (c) and (d), the dashed and solid contours correspond to the −0.6 and 0.6 m s^{-1} isolines, respectively. All these variables are extracted from the point (54.0°E, 19.0°S) represented with a black star in Figure 8a.

noteworthy that the maximum cooling of the SST occurs more than 5 h after the passage of the tropical cyclone. The thermocline goes down to 120 m depth at 21 h of simulation. As the cyclone approaches the point E, the depth of the oceanic boundary layer (OBL) increases, mainly because of the vertical mixing (light gray in Figure 9b) (Price, 1981). Temperature decreases by more than 3°C over 75 m. After the passage of the cyclone, the depth of the OBL decreases by strong advection (dark gray in Figure 9a) showing that Bejisa was not strong enough to entirely erode the thermocline (Zambon et al., 2014). This behavior is similar to the upper ocean response during typhoon Kalmaegi (2014) (Zhang et al., 2016).

At the beginning of the simulation, the *u*-component of the oceanic current is negative (east-west direction) between 0 and 150 m and increases from −0.3 to −0.8 m s^{-1} at the surface while Bejisa is approaching the point E (Figure 9c). The maximum is reached after 14 h of simulation, i.e., 4 h before the cyclone is at its closest to point E. After 18 h of simulation, as the eyewall passes and the wind shifts, the *u*-component of the oceanic current changes sign and becomes positive (west-east direction) with a maximum of 0.8 m s^{-1} reached after 22 h of simulation. After 30 h (12 h after the passage of the cyclone), the *u*-component of the current changes sign again and becomes negative. The *v*-component of the oceanic current is also negative (south-north direction) during the first part of the simulation and increases from −0.2 to −0.8 m s^{-1} between the surface and 110 m depth. The simulated system passes close to the point E at 18 UTC on 1 January (Figure 9a). Since the track of Bejisa is north-south, the *v*-component of the oceanic current changes sign later than the *u*-component (∼25 h). An inertial oscillation of the *u* and *v*-components of the oceanic current with a period of ∼1 day is visible between 0 and 100 m depth (Figures 9c and 9d). This result is similar to the point S2 over deep water in the ocean-atmosphere-wave coupled simulation of Hurricane Ivan in Zambon et al. (2014).

This first evaluation of the fully coupled OWA simulation of Bejisa shows good agreement with the available observations. The associated physical processes are in accordance with the literature. In particular, MSWC reproduces well the location and evolution of waves along the northern coast of La Réunion. In addition, the oceanic cooling wake is well simulated, as is the inertial oscillation of the oceanic current.

5. Sensitivity Analysis to Oceanic Waves Coupling

In order to highlight the impact of oceanic waves coupling on the evolution of the tropical cyclone, the OWA and OA simulations (see Table 1) are compared.

5.1. Track and Intensity

To identify the impact of oceanic waves coupling on the atmosphere, storm track, and intensity from the OA and OWA simulations are compared (in Figures 4a and 4b). It appears that including a wave model does not have a significant impact on the simulated tropical cyclone track for this case study (Figure 4a). However, the minimum MSLP is 0–2.5 hPa lower for the OA simulation than in the OWA simulation (Figure 4b). Thus, including the wave model acts to reduce the intensity of the cyclone slightly. This result is consistent with previous studies (Lionello et al., 1998; Liu et al., 2011, 2012) and was attributed to the increase of the sea surface roughness by oceanic waves (next section). In Wada et al. (2012) and Zambon et al. (2014), the authors attributed this to the increase of the oceanic vertical mixing by oceanic waves. In the present study, this effect is negligible compared to the increase of sea surface roughness and will not be detailed here. It is important to recall that the effects of sea salt on turbulent surface fluxes and cloud microphysics are not taken into account despite their potential impact on TC intensity (Fan et al., 2016; Zhao et al., 2017).

5.2. Charnock Parameter and Roughness Length

The Charnock parameter is a key parameter in waves-atmosphere coupling since it is used in the roughness length formulation (equation 1). To highlight the impact of the oceanic waves coupling on the Charnock parameter and roughness length computations, the spatial distribution of these parameters for the OA and OWA simulations are shown on Figures 10a and 10d and Figures 10b and 10e, respectively. Figures 10c and 10f present scatterplots of the Charnock parameter and the roughness length as a function of the relative wind speed (horizontal wind speed at first level of the atmospheric model minus sea surface current).

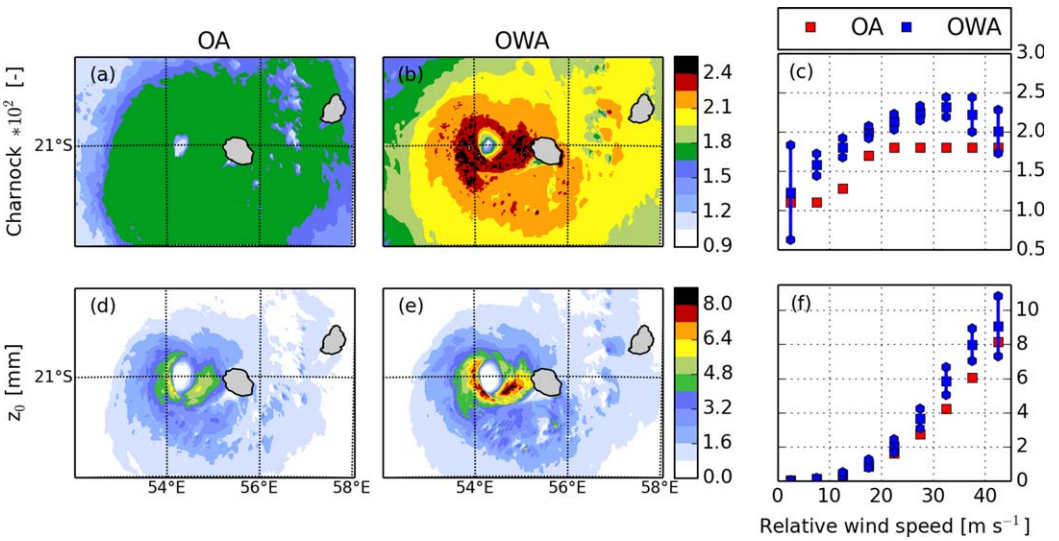

Figure 10. (left plots) Charnock parameter (w/o unit; first row) and roughness length (mm; second row) at 06 UTC on 2 January 2014 for the OA and (middle plots) OWA simulations. (right plots) Scatterplot of the Charnock parameter and roughness length versus relative wind speed. Blue and red squares correspond to mean values and blue diamonds correspond to the standard deviation.

In the OA simulation, the Charnock parameter is computed from the Hare et al. (1999) parameterization (equation (3)). Since the Charnock parameter is constant and equal to 0.018 for 10 m wind speed higher than 18 m s^{-1}, no spatial variability of this parameter is observed in the inner core of the system in the OA simulation (Figures 10a and 10c). In the OWA simulation, the spatial variability of the Charnock parameter (Figure 10b) is closely related to the 10 m wind speed distribution (Figure 5c). Moreover, it allows the sea state history to be considered from young to mature oceanic waves, represented by the standard deviation (blue diamonds on Figure 10c). It varies from 0.019 to 0.025 under the TC (Figure 10b). In the eye of the TC and for both simulations, the weak 10 m wind speed induces a low Charnock parameter. The maximum of the Charnock parameter is located in the eyewall region where the maximum values are twice as high in the OWA simulation (Figure 10b) as in the OA simulation (Figure 10a). Furthermore, a scatterplot of Charnock parameter versus of the relative wind speed (Figure 10c) shows that, for low and high relative wind speed, the Charnock parameter can vary by a factor of 2 due to the history of the sea state.

As the Charnock parameter is used to compute the roughness length (z_0), the impact of the wave coupling can also be seen on its spatial variability and extreme values (Figures 10d–10f). In the OA simulation, z_0 is between 4.8 and 5.6 mm in the eyewall and barely exceeds 5.6 mm at some points (Figure 10d) while, in the OWA simulation, z_0 exceeds 5.6 mm and even reaches 8 mm in the eyewall (Figure 10e). The scatterplot of roughness length versus the relative wind speed (Figure 10f) shows that the sea state history is only visible on the high relative wind speed ($>$ 25 m s^{-1}). This can be explained by the fact that, at low wind speed, the roughness length is controlled by the viscosity term in equation (1) and is therefore not sensitive to the Charnock parameter. Thus, the oceanic waves coupling significantly modify the roughness length at high wind speed even if the impact on tropical cyclone intensity (Figure 4b) and on the 10 m wind speed (not shown here) is mitigated. The length of the simulations might be too short to highlight the effect of oceanic wave coupling on TC structure, intensity, and track.

5.3. Turbulent Surface Fluxes

To explain the mitigated effect of oceanic waves on the TC intensity, the averaged turbulent momentum flux (τ; in kg m^{-1} s^{-2}), sensible heat flux (H; in W m^{-2}), and latent heat flux (LE; in W m^{-2}) are presented in Figure 11.

These horizontal cross-sections were obtained by reorienting the TC along the direction of motion. Then, an average was taken for momentum and heat fluxes during the simulated period. The direction of propagation is represented by the black arrows. Spatial variability of the turbulent surface fluxes given by the OWA simulation (Figures 11a, 11c, and 11e) is quite similar to that of the instantaneous roughness length (Figure 10e). Strong asymmetry is present in the turbulent surface fluxes given by the OWA simulation. Larger turbulent fluxes are located in the forward right quadrant. There, the momentum flux is about 4 kg m^{-1} s^{-2}, the sensible heat flux is 150 W m^{-2} and the latent heat flux is 600 W m^{-2}. In the opposite quadrant (rear left), values are, respectively, 3.5 (10%), 50 (30%), and 450 (25%) W m^{-2}. This asymmetry in the turbulent surface fluxes is directly linked to the cooling wake induced by the TC (Figure 8). Where cooling is maximum, the turbulent surface fluxes are reduced. For the momentum and latent heat fluxes, only the stability of the atmosphere is used, inducing a lower effect than for the sensible heat flux. For the latter, the cooling effect is greater because temperature gradient is also taken into account in its computation.

The difference between the OWA and OA simulations show the impact of oceanic waves on turbulent surface fluxes (Figures 11b, 11d, and 11f). The outstanding effect is an increase of turbulent surface fluxes in the rear-left quadrant of the TC. It is in opposition with the decrease of the fluxes due to the SST cooling wake (Figures 11a, 11c, and 11e). Globally, oceanic waves produce averaged turbulent surface fluxes that are approximately a tenth of kg m^{-1} s^{-2} or W m^{-2} stronger. This is mainly attributed to the Charnock parameter and roughness length being larger in the OWA simulation than the OA one (Figures 10c and 10f). However, divergences in turbulent flux parameterizations at high wind speeds imply a need to revisit them (Lebeaupin Brossier et al., 2008; Seyfried et al., 2017) and meaning that this sensitivity of turbulent fluxes to oceanic waves is not generalizable. Further studies with longer simulations and statistical diagnoses (as in Lengaigne et al., 2018; Samson et al., 2014) are necessary to address the physical origin of these differences.

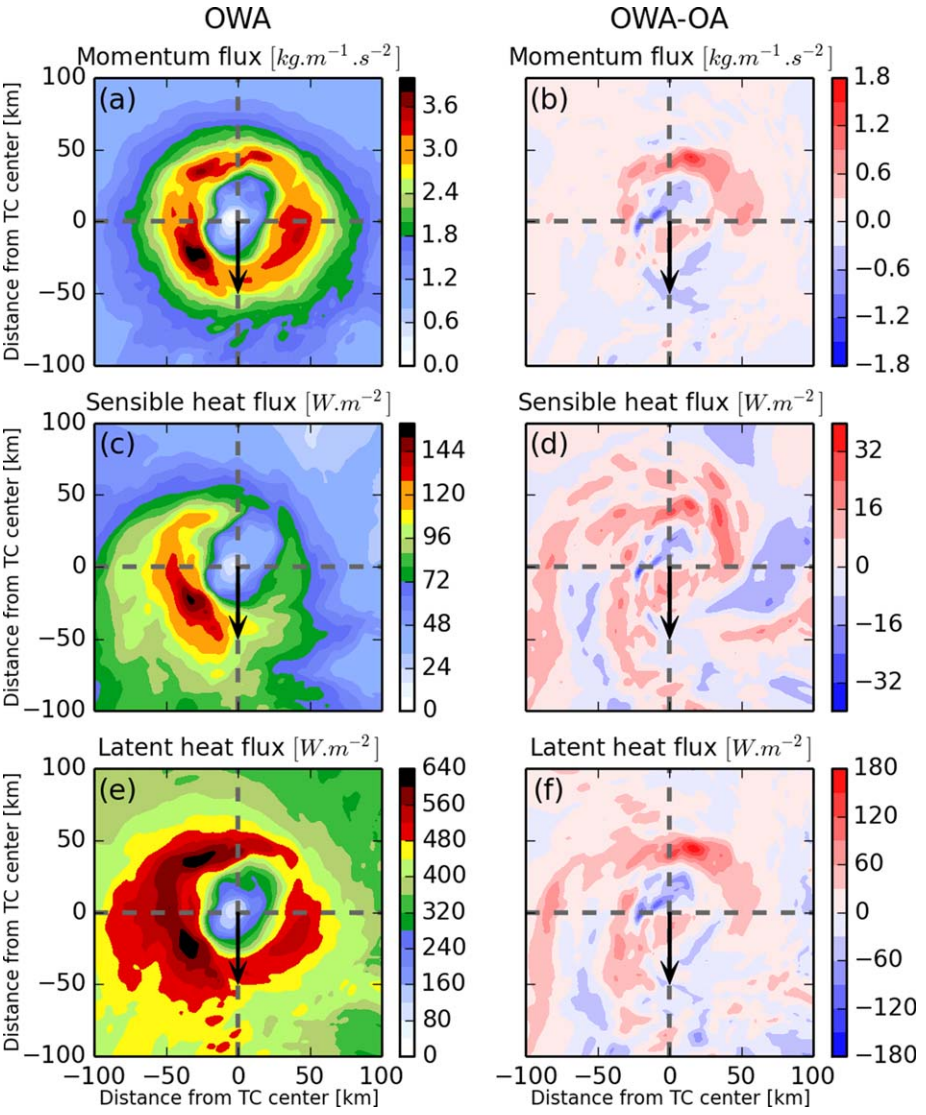

Figure 11. (a) Momentum (kg m^{-1} m^{-2}), (c) sensible heat (W m^{-2}), and (e) latent heat (W m^{-2}) fluxes simulated by the OWA simulation. (b) Differences between OWA and OA simulation for momentum (kg m^{-1} m^{-2}) (d) sensible heat (W m^{-2}), and (f) latent heat (W m^{-2}) fluxes. All these fields are averaged over the simulated time and reoriented along the TC track. The black arrows indicate the direction of TC motion. Gray dashed lines separate the different quadrants of the TC.

6. Impact of the Significant Wave Height on Sea Salt Aerosols

Due to the role of sea salt aerosols in turbulent surface fluxes and their role as cloud condensation nuclei (CCN), the impact of the significant wave height on their emission is analyzed through additional simulations (see Table 1). However as mentioned in section 3.4, the effects of sea salt on turbulent air-sea fluxes and on cloud microphysics are not considered in this paper and will be addressed in a future study.

6.1. Total Sea Salt Aerosol Mass Flux

As discussed previously, oceanic waves are one of the key parameters involved in the sea salt aerosol emissions in high wind conditions. The impact of oceanic waves on the generation of sea salt aerosols is thus examined below. Figures 12a–12f show the net total sea salt flux (sum of emission—dry deposition on the five sea salt aerosol modes) at 06 UTC on 2 January 2014. The only difference between all the simulations is the significant wave height used in the sea salt aerosol source function modeled by the Ovadnevaite et al. (2014) parameterization (see Table 1).

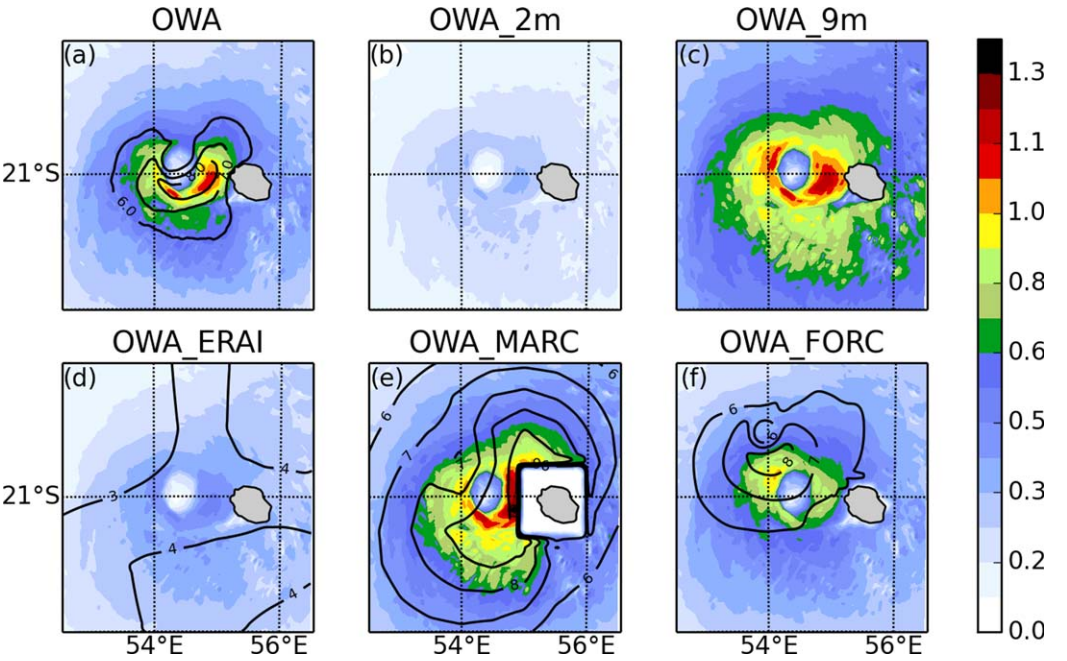

Figure 12. Total instantaneous net sea salt aerosol flux (μg m^{-2} s^{-1}, colors) at 06 UTC on 2 January for the (a) OWA, (b) OWA_2m, (c) OWA_9m, (d) OWA_ERAI, (e) OWA_MARC, and (f) OWA_FORC simulations. Black contours on plot (d) correspond to the 3.0, 3.5, and 4.0 m isolines for the significant wave height from ERA-Interim. Black contours on plots (a), (e), and (f) correspond to the 6, 7, 8, and 9 m isolines for the significant wave height from WW3 online, MARC, and WW3 offline, respectively.

In the OWA simulation (Figure 12a), the highest values of the total net sea salt flux are collocated with the maximum surface wind speed (Figure 5c) and the highest waves (Figure 12a). They reach 1.1 μg m^{-2} s^{-1} in the front quadrants of the eyewall. Along the track of the cyclone, up to 0.8 mg m^{-2} of sea salt aerosols are emitted during the first 36 h (not shown here). Outside the inner core region of the system ($\sim$ 200 km away from the storm center), the total sea salt flux is low (less than 0.3 μg m^{-2} s^{-1}) due to both lower wind speed and lower significant wave height.

The significant wave height used in OWA_2m (Figure 12b) and OWA_9m (Figure 12c) is homogeneous and, thus, does not exhibit the signature of the tropical cyclone. Consequently, the effect of the spatial variation of the significant wave height on sea salt aerosol flux can be examined. As mentioned in section 3.5, 2 and 9 m correspond to the minimum and maximum H_s values encountered in the simulation domain during Bejisa. The asymmetry in the total instantaneous net sea salt aerosol flux is almost lost in these two configurations. Indeed, for both simulations, the maximum sea salt aerosol flux is mainly driven by the 10 m wind speed. Consequently, it is localized in the eastern, southern, and western regions, whereas it was located in the front quadrants of the eyewall in the OWA simulation. Furthermore, the radial gradient of sea salt aerosol fluxes is lower in the OWA_2m and OWA_9m simulations compared to the OWA simulation.

The significant wave height in OWA_ERAI (black contours in Figure 12d) does not show the signature of the tropical cyclone, whereas the OWA, OWA_MARC, and OWA_FORC simulations do (black contours in Figures 12a, 12e, and 12f). H_s is almost uniform all around the cyclone. It only reaches 3–3.5 m while it exceeds 8 m in the OWA simulation. Consequently, the sea salt aerosol flux is around 0.3 μg m^{-2} s^{-1} in the eyewall and barely reaches 0.5 μg m^{-2} s^{-1} on the southern side of the system, where the maximum wind speed is encountered. These values are 2–3 times lower than those of the OWA simulation, which also corresponds to the H_s ratio between the two simulations. The low resolution of ERA-Interim data ($\sim$ 80 km) is mainly responsible for these differences.

The spatial extension of H_s in the OWA_MARC simulation (black contours in Figure 12e) is not consistent with the 10 m wind speed simulated by the OWA simulation (Figure 5c). The maximum of H_s is located in the front quadrants of the TC, where the maximum wind speed is found, while in OWA_MARC, the H_s is

Table 3
Instantaneous Net Sea Salt Aerosol Flux Spatially Averaged Over the Box Displayed in Figure 12 for Each of the Five Modes. ($\mu g\ m^{-2}\ s^{-1}$ and $\#\ m^{-2}\ s^{-1}$)

Simulation Unit	OWA		OWA_2m	OWA_9m
	$\mu g\ m^{-2}\ s^{-1}$ (%)	$\#\ m^{-2}\ s^{-1}$ (%)	$\#\ m^{-2}\ s^{-1}$ (%)	$\#\ m^{-2}\ s^{-1}$ (%)
Mode 1	$7. \times 10^{-4}$ (< 0.5)	6.7×10^{7} (52.5)	3.9×10^{7} (58.7)	9.1×10^{7} (49.5)
Mode 2	1.2×10^{-4} (< 0.5)	6.9×10^{5} (0.5)	2.2×10^{5} (0.3)	1.2×10^{6} (0.6)
Mode 3	5.9×10^{-6} (< 0.5)	$4. \times 10^{3}$ (< 0.01)	2.3×10^{3} (< 0.01)	5.6×10^{3} (< 0.01)
Mode 4	1.9 (99.5)	$6. \times 10^{7}$ (47.0)	2.7×10^{7} (40.9)	9.1×10^{7} (49.5)
Mode 5	9.6×10^{-3} (< 0.5)	2.7×10^{3} (< 0.01)	1.1×10^{3} (< 0.01)	4.3×10^{3} (< 0.01)

Note. For the OWA Simulation, Both the Mass Flux ($\mu g\ m^{-2}\ s^{-1}$) and the Number Flux ($\#\ m^{-2}\ s^{-1}$) are Displayed. For the OWA_2m and OWA_9m Simulations the Net Sea Salt Aerosol Flux is Presented. In parenthesis is the contribution of each mode to the total flux (in percentage).

homogeneous over the TC. This is explained by the low resolution of the wave model used in the MARC database (0.5°). These H_s differences imply strong differences in the instantaneous net sea salt fluxes, which are higher by a factor of 1.5 in the OWA_MARC simulation (Figure 12e) than in the OWA simulation (Figure 12a).

The OWA_FORC simulation highlights the problem of using a wave field from a model where the storm has a different position. Since the OWA_FORC simulation uses the H_s from WW3 forced by the ECMWF operational high-resolution analysis (black contours in Figure 12f), the significant wave height is consistent with the wind field of the ECMWF analysis and not with that of the Meso-NH simulation. In the ECMWF analysis, the center of the cyclone is located ∼50–60 km north-west of its actual position in the OWA simulation. Since the significant wave height has maximum values (∼8 m) north of the position of the simulated cyclone, the net sea salt aerosol flux is enhanced in the northern part of the cyclone (Figure 12f). Thus, the net sea salt flux reaches 0.9 $\mu g\ m^{-2}\ s^{-1}$ in the north-west quadrant while it only reaches 0.6 $\mu g\ m^{-2}\ s^{-1}$ in the southern quadrant, introducing strong asymmetry in the sea salt aerosol emissions due to inconsistent significant wave height.

Using the sea state from a full ocean-waves-atmosphere coupled system is essential to obtain consistent sea salt emissions. It produces asymmetric sea salt emissions by collocating the maximum of the sea salt flux with the highest values of surface wind speed and significant wave height. This will be a key point when considering the effect of sea salt on momentum and heat fluxes, and on the cloud lifecycle.

6.2. Modal Net Sea Salt Aerosol Mass and Number Fluxes

Table 3 presents the impact of different significant wave height on the modal distribution of the instantaneous net sea salt aerosol fluxes (emission–dry deposition for the five sea salt aerosol modes) for OWA, OWA_2m, and OWA_9m simulations (see Table 1). As mentioned in section 3.1, the sea salt aerosols distributions are modeled by five log-normal modes, ranging from ultrafine sea salt aerosols (nm) to coarse ones (μm).

For the OWA simulation, the sea salt aerosol mass flux is maximum for the fourth mode and reaches 1.9 $\mu g\ m^{-2}\ s^{-1}$. This is the main contribution (99.5%) to the total net sea salt aerosol mass flux (Figure 12). The sea salt aerosol mass flux in the four other modes is $\sim 10^2$ (fifth mode) to 10^6 times (third mode) less important than in the fourth mode. From a microphysical point of view, it is interesting to look at the sea salt aerosol flux in terms of number concentration. The highest net sea salt aerosol number flux occurs for modes 1 and 4 with about 6.0×10^7 particles $m^{-2}\ s^{-1}$ emitted for the OWA simulation. About $\sim 10^2$ and $\sim 10^4$ times less particles are emitted in the second mode, and in the third and fifth mode, respectively. It must be noted that the larger sea salt particles can more readily act as CCN because they require smaller supersaturations to be activated to become a cloud droplet (Seinfeld & Pandis, 2016).

When a constant and homogeneous significant wave height of 2 m (OWA_2m) is imposed (it corresponds to a wave height encountered more than 500 km away from the tropical cyclone center), the sea salt aerosol number flux in the fourth mode is theoretically decreased compared to the OWA simulation (Table 3). However, it is important to note that the contribution of the fourth mode to the total number flux has

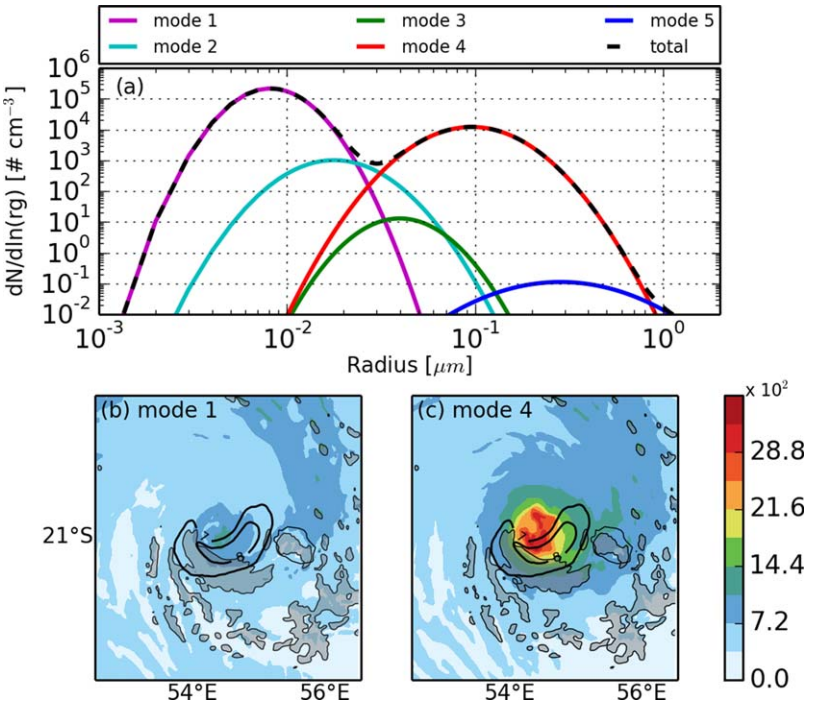

Figure 13. (a) Sea salt aerosol number size distribution for the OWA simulation. Number concentration of sea salt aerosols vertically averaged from the ground to the altitude of the isotherm 0°C (# cm^{-3}) for the (b) first and (c) fourth modes in the OWA simulation. Black contours on (b) and (c) correspond to H_s values of 7 and 8 m. The gray shaded areas correspond to instantaneous rain rate higher than 10 mm h^{-1}.

decreased from 47.0 to 40.9%, while the contribution of the first mode has increased from 52.5 to 58.8%. The second, third, and fifth modes contribute to less than 1% to the total number flux. In the OWA_9m simulation, a H_s value of 9 m, which is almost the maximum value simulated in the inner core of the system, is imposed over the domain. The first and fourth modes have the same contribution to the total number flux ($\sim$9.1 $\times$ 10^7 particles m^{-2} $^{-1}$). Contrary to the OWA_2m simulation, the contribution of the fourth mode has increased (from 47.0 to 49.5%) while the one of the first mode has decreased (from 52.5 to 49.5%). Consequently, the significant wave height does not only impact the amount of particles emitted at the ocean surface, but it also influences the proportion of aerosol particles in the five modes which is a key point for cloud droplets generation.

Figure 13a shows the sea salt aerosol number size distribution for the OWA simulation. It clearly shows that the first and fourth modes are the most important modes in terms of number concentration. The spatial variation of the sea salt aerosol number concentration integrated from 0 m to the altitude of the isotherm 0°C is plotted in Figures 13b and 13c for these two modes in the OWA simulation. In the rainband located north-east of the tropical cyclone center, the number concentration is similar for the two modes ($\sim$1,100 particles cm^{-3}). The precipitation in this region is relatively scarce, and aerosols are not efficiently scavenged. In the inner core of the system, the particles number of the two modes is very different. While it reaches 3,000 particles cm^{-3} in the fourth mode, it does not exceeds 1,500 particles cm^{-3} in the first mode. This difference can be attributed to the sea salt aerosol scavenging that acts differently in the two modes. Aerosol scavenging is less efficient for aerosol particles with radius between 0.1 and 1 μm (Randerson, 1984). Therefore, sea salt aerosols in this range of radius (typically mode 5 and part of mode 4; see Figure 13a) are still available in the atmosphere.

It is evident from these results that a careful description of the significant wave height can affect not only the spatial distribution of sea salt aerosols, but also the relative contribution of each mode in the total number flux. The number of particles in each mode is crucial for an integration in aerosols and microphysics schemes since these physical processes are strongly size-dependent.

7. Conclusions

A newly developed Ocean-Waves-Atmosphere coupled system called MSWC for Meso-NH/SurfEx/WW3/CROCO is presented in this paper. For the first time, MSWC is used to simulate a tropical cyclone. The case study is Tropical Cyclone Bejisa, which passed close to La Réunion in January 2014. The effects of the oceanic waves on the ocean and the atmosphere are examined. Through five numerical experiments, attention is focused on the impact of the oceanic waves on different surface parameters such as the Charnock parameter, the roughness length, the turbulent fluxes, and the sea salt aerosol emissions.

Overall, the ability of the fully coupled system to reproduce the behavior of the OWA interactions in the context of a tropical cyclone has been shown. The track of Bejisa was well reproduced by the model. The trend of the intensity was fairly well simulated, but its amplitude was underestimated compared to the best-track analysis. The significant wave height from the wave model exhibits a bean-like structure with the maximum values in the front quadrants of the tropical cyclone. This structure is produced by the higher wind speed in those quadrants associated with the forward motion of the storm. These quadrants are thus associated with an increase of the effective fetch in the direction of the motion of the storm. The simulated significant wave height shows globally good agreement with buoy and altimeter measurements available during this time period. The well-known decrease of the sea surface temperature in the wake of the tropical cyclone is also simulated with an increase of the depth of the thermocline. After the passage of Bejisa, a rising of the thermocline is visible. In addition, an inertial oscillation is simulated behind the tropical cyclone with a period of approximately 1 day.

The impact of oceanic waves on turbulent surface fluxes is mitigated despite a small increase of the momentum and heat fluxes when coupling with a wave model. Further studies are necessary to address the physical origin of this difference. The spatial distribution and magnitude of the sea salt aerosol fluxes and concentration of each mode show a strong dependence on the significant wave height field. It has been shown that online coupling of a wave model and an atmospheric model is necessary if the aim is to simulate sea salt aerosol emissions consistent with the wind and wave fields that generate them. Forced systems mainly have sea salt aerosol fluxes that are not located where the maximum wave heights are present. High-resolution wave height forced by another meteorological model tends to locate the sea salt source in the wrong region while low-resolution wave height data does not reproduce the magnitude of the emission. The correct location of the sea salt sources is a key point when considering the impact of sea salt on the heat and momentum fluxes. It will also be of major importance when using the sea salt aerosols generated by the cyclonic winds and waves as a source of cloud condensation and ice freezing nuclei in multimoment microphysical schemes. The complex 3-D structure of the ocean and the atmosphere and the very localized position of the oceanic waves in the front of the eyewall structure impose the use of a fully coupled system to study the turbulent and sea salt aerosol fluxes.

Tropical Cyclone Bejisa was chosen as a case study because it passed close to La Réunion, where some observations were available. In addition, high-resolution AROME-IO analyses were available which avoided the need to use a bogus or a long spin-up period. More case studies are now required to draw more general conclusions about the effect of oceanic waves on atmospheric and oceanic parameters. Such a high-resolution, fully coupled model could be used for a large panel of applications. The air-sea interactions during intensification stages could be studied and additional parameterizations of the air-sea exchanges should be tested. This model is also a powerful tool to analyze the sea state and wind field during extreme weather events, in particular for dimensioning the technology for renewable marine energy in cyclonic basins.

Acknowledgments
This work was carried out in the framework of the DiMe project, which benefits from government support managed by the Agence Nationale de la Recherche under the Investissement d'Avenir program with the reference ANR-10-IEED-0006–14. Additional financial support was also provided by the Université de la Réunion through the federation Observatoire des Milieux Naturels et des Changements Globaux (OMNCG) of the Observatoire des Sciences de l'Univers de la Réunion (OSU-R). Thanks to the reviewers for their suggestions and comments that helped to improve the manuscript. We are grateful to the society NortekMed and the DDE (Direction Départementale de l'Equipement) for providing buoy data. Philippe Caroff and Sébastien Langlade (Météo-France/RSMC La Réunion) are acknowledged for their detailed report about Bejisa cyclogenesis and evolution. Françoise Orain, Stéphane Saux-Picart, and Marie-Noelle Bouin are also acknowledged for their discussions of sea surface temperature data and turbulent surface fluxes parameterization. The simulations were performed on the supercomputer "beaufix" of Météo-France in Toulouse, France. The models used in this paper are open-source and available freely at the following websites: http://mesonh.aero.obs-mip.fr for Meso-NH/SurfEx, https://gforge.inria.fr/projects/croco/ for CROCO, https://forge.ifremer.fr/svn/ww3 for WW3, and https://portal.enes.org/oasis for OASIS.

References

Aijaz, S., Ghantous, M., Babanin, A. V., Ginis, I., Thomas, B., & Wake, G. (2017). Nonbreaking wave-induced mixing in upper ocean during tropical cyclones using coupled hurricane-ocean-wave modeling. *Journal of Geophysical Research: Oceans*, *122*, 3939–3963. https://doi.org/10.1002/2016JC012219

Andreas, E. L. (2004). Spray stress revisited. *Journal of Physical Oceanography*, *34*(6), 1429–1440. https://doi.org/10.1175/1520-0485(2004)034<1429:SSR>2.0.CO;2

Andreas, E. L., & Emanuel, K. A. (2001). Effects of sea spray on tropical cyclone intensity. *Journal of the Atmospheric Sciences*, *58*(24), 3741–3751. https://doi.org/10.1175/1520-0469(2001)058<3741:EOSSOT>2.0.CO;2

Ardhuin, F., O'Reilly, W. C., Herbers, T. H. C., & Jessen, P. F. (2003). Swell transformation across the continental shelf. Part I: Attenuation and directional broadening. *Journal of Physical Oceanography*, *33*(9), 1921–1939. https://doi.org/10.1175/1520-0485(2003)033<1921:STATCS>2.0.CO;2

Ardhuin, F., Rogers, E., Babanin, A. V., Filipot, J.-F., Magne, R., Roland, A., et al. (2010). Semiempirical dissipation source functions for ocean waves. Part I: Definition, calibration, and validation. *Journal of Physical Oceanography*, *40*(9), 1917–1941. https://doi.org/10.1175/2010JPO4324.1

Ardhuin, F., & Roland, A. (2012). Coastal wave reflection, directional spread, and seismoacoustic noise sources. *Journal of Geophysical Research*, *117*, C00J20. https://doi.org/10.1029/2011JC007832

Bao, J.-W., Wilczak, J. M., Choi, J.-K., & Kantha, L. H. (2000). Numerical simulations of air-sea interaction under high wind conditions using a coupled model: A study of hurricane development. *Monthly Weather Review*, *128*(7), 2190–2210. https://doi.org/10.1175/1520-0493(2000)128<2190:NSOASI>2.0.CO;2

Barthe, C., Hoarau, T., & Bovalo, C. (2016). Cloud electrification and lightning activity in a tropical cyclone-like vortex. *Atmospheric Research*, *180*, 297–309. https://doi.org/10.1016/j.atmosres.2016.05.023

Battjes, J. A., & Janssen, J. P. F. M. (1978). Energy loss and set-up due to breaking of random waves. In *Coastal engineering 1978* (pp. 569–587). New York, NY: American Society of Civil Engineers. https://doi.org/10.1061/9780872621909.034

Bechtold, P., Bazile, E., Guichard, F., Mascart, P., & Richard, E. (2001). A mass-flux convection scheme for regional and global models. *Quarterly Journal of the Royal Meteorological Society*, *127*, 869–886.

Beckmann, A., & Haidvogel, D. B. (1993). Numerical simulation of flow around a tall isolated seamount. Part I: Problem formulation and model accuracy. *Journal of Physical Oceanography*, *23*(8), 1736–1753. https://doi.org/10.1175/1520-0485(1993)023<1736:NSOFAA>2.0.CO;2

Bender, M. A., & Ginis, I. (2000). Real-case simulations of hurricane-ocean interaction using a high-resolution coupled model: Effects on hurricane intensity. *Monthly Weather Review*, *128*(4), 917–946. https://doi.org/10.1175/1520-0493(2000)128<0917:RCSOHO>2.0.CO;2

Berrisford, P., Dee, D., Poli, P., Brugge, P., Fielding, R., Fuentes, K. M., et al. (2011). *The ERA-Interim archive version 2.0* (ERA Rep. Ser. 1). Reading, UK: European Centre for Medium-Range Weather Forecasts (ECMWF).

Bougeault, P., & Lacarrère, P. (1989). Parameterization of orography-induced turbulence in a mesobeta-scale model. *Monthly Weather Review*, *117*(8), 1872–1890. https://doi.org/10.1175/1520-0493(1989)117<1872:POOITI>2.0.CO;2

Breivik, Ø., Mogensen, K., Bidlot, J.-R., Balmaseda, M. A., & Janssen, P. A. E. M. (2015). Surface wave effects in the NEMO ocean model: Forced and coupled experiments. *Journal of Geophysical Research: Oceans*, *120*, 2973–2992. https://doi.org/10.1002/2014JC010565

Chane-Ming, F., Ibrahim, C., Barthe, C., Jolivet, S., Keckhut, P., Liou, Y.-A., et al. (2014). Observation and a numerical study of gravity waves during tropical cyclone Ivan (2008). *Atmospheric Chemistry and Physics*, *14*(2), 641–658. https://doi.org/10.5194/acp-14-641-2014

Charnock, H. (1955). Wind stress on a water surface. *Quarterly Journal of the Royal Meteorological Society*, *81*(350), 639–640. https://doi.org/10.1002/qj.49708135027

Chen, S. S., & Curcic, M. (2016). Ocean surface waves in Hurricane Ike (2008) and Superstorm Sandy (2012): Coupled model predictions and observations. *Ocean Modelling*, *103*, 161–176. https://doi.org/10.1016/j.ocemod.2015.08.005

Chen, S. S., Zhao, W., Donelan, M. A., Price, J. F., & Walsh, E. J. (2007). The CBLAST-hurricane program and the next-generation fully coupled atmosphere-wave-ocean models for hurricane research and prediction. *Bulletin of the American Meteorological Society*, *88*(3), 311–317. https://doi.org/10.1175/BAMS-88-3-311

Claeys, M. (2016). *Modélisation des aérosols marins et de leur impact radiatif direct sur le bassin méditerranéen dans le cadre du projet CHARMEX* (Ph.D. thesis). Toulouse, France: Université de Toulouse.

Cline, I. M. (1920). Relation of changes in storm tides on the coast of the Gulf of Mexico to the center and movement of hurricanes. *Monthly Weather Review*, *48*(3), 127–146. https://doi.org/10.1175/1520-0493(1920)48<127:ROCIST>2.0.CO;2

Colella, P., & Woodward, P. R. (1984). The piecewise parabolic method (PPM) for gas-dynamical simulations. *Journal of Computational Physics*, *54*(1), 174–201. https://doi.org/10.1016/0021-9991(84)90143-8

Craig, A., Valcke, S., & Coquart, L. (2017). Development and performance of a new version of the OASIS coupler, OASIS3-MCT_3.0. *Geoscientific Model Development*, *10*, 3297–3308. https://doi.org/10.5194/gmd-10-3297-2017

Cuxart, J., Bougeault, P., & Redelsperger, J.-L. (2000). A turbulence scheme allowing for mesoscale and large-eddy simulations. *Quarterly Journal of the Royal Meteorological Society*, *126*, 1–30.

D'Asaro, E. A., Sanford, T. B., Niiler, P. P., & Terrill, E. J. (2007). Cold wake of hurricane Frances. *Geophysical Research Letters*, *34*, L15609. https://doi.org/10.1029/2007GL030160

Davy, C., Barruol, G., Fontaine, F., & Cordier, E. (2016). Analyses of extreme swell events on La Réunion Island from microseismic noise. *Geophysical Journal International*, *207*(3), 1767–1782. https://doi.org/10.1093/gji/ggw365

Debreu, L., Marchesiello, P., Penven, P., & Cambon, G. (2012). Two-way nesting in split-explicit ocean models: Algorithms, implementation and validation. *Ocean Modelling*, *49–50*, 1–21. https://doi.org/10.1016/j.ocemod.2012.03.003

de Leeuw, G., Andreas, E. L., Anguelova, M. D., Fairall, C. W., Lewis, E. R., O'Dowd, C., et al. (2011). Production flux of sea spray aerosol. *Reviews of Geophysics*, *49*, RG2001. https://doi.org/10.1029/2010RG000349

DeMott, P. J., Hill, T. C. J., McCluskey, C. S., Prather, K. A., Collins, D. B., Sullivan, R. C., et al. (2016). Sea spray aerosol as a unique source of ice nucleating particles. *Proceedings of the National Academy of Sciences of the United States of America*, *113*(21), 5797–5803. https://doi.org/10.1073/pnas.1514034112

Doyle, J. D. (2002). Coupled atmosphere-ocean wave simulations under high wind conditions. *Monthly Weather Review*, *130*(12), 3087–3099. https://doi.org/10.1175/1520-0493(2002)130<3087:CAOWSU>2.0.CO;2

Doyle, J. D., Hodur, R., Chen, S., Jin, Y., Msokaitis, J., Wang, S., et al. (2014). Tropical cyclone prediction using COAMPS-TC. *Oceanography*, *27*(3), 104–115. https://doi.org/10.5670/oceanog.2014.72

Emanuel, K. A. (1986). An air-sea interaction theory for tropical cyclones. Part I: Steady-state maintenance. *Journal of the Atmospheric Sciences*, *43*(6), 585–605. https://doi.org/10.1175/1520-0469(1986)043<0585:AASITF>2.0.CO;2

Esquivel-Trava, B., Ocampo-Torres, F. J., & Osuna, P. (2015). Spatial structure of directional wave spectra in hurricanes. *Ocean Dynamics*, *65*(1), 65–76. https://doi.org/10.1007/s10236-014-0791-9

Fairall, C. W., Bradley, E. F., Hare, J. E., Grachev, A. A., & Edson, J. B. (2003). Bulk parameterization of air-sea fluxes: Updates and verification for the COARE algorithm. *Journal of Climate*, *16*(4), 571–591. https://doi.org/10.1175/1520-0442(2003)016<0571:BPOASF>2.0.CO;2

Fairall, C. W., Kepert, J. D., & Holland, G. J. (1994). The effect of sea spray on surface energy transports over the ocean. *Global Atmosphere and Ocean System*, *2*(2–3), 121–142.

Fan, J., Wang, Y., Rosenfeld, D., & Liu, X. (2016). Review of aerosol-cloud interactions: Mechanisms, significance, and challenges. *Journal of the Atmospheric Sciences*, *73*(11), 4221–4252. https://doi.org/10.1175/JAS-D-16-0037.1

Fierro, A. O., Rogers, R. F., Marks, F. D., & Nolan, D. S. (2009). The impact of horizontal grid spacing on the microphysical and kinematic structures of strong tropical cyclones simulated with the WRF-ARW model. *Monthly Weather Review*, *137*(11), 3717–3743. https://doi.org/10.1175/2009MWR2946.1

Gentry, M. S., & Lackmann, G. M. (2010). Sensitivity of simulated tropical cyclone structure and intensity to horizontal resolution. *Monthly Weather Review*, *138*(3), 688–704. https://doi.org/10.1175/2009MWR2976.1

Gregory, D., Morcrette, J.-J., Jakob, C., Beljaars, A. C. M., & Stockdale, T. (2010). Revision of convection, radiation and cloud schemes in the ECMWF integrated forecasting system. *Quarterly Journal of the Royal Meteorological Society*, *126*(566), 1685–1710. https://doi.org/10.1002/qj.49712656607

Grythe, H., Ström, J., Krejci, R., Quinn, P., & Stohl, A. (2014). A review of sea-spray aerosol source functions using a large global set of sea salt aerosol concentration measurements. *Atmospheric Chemistry and Physics*, *14*(3), 1277–1297. https://doi.org/10.5194/acp-14-1277-2014

Hare, J. E., Persson, P. O. G., Fairall, C., & Edson, J. (1999). Behavior of Charnock's relationship for high wind conditions. In *Proceedings of 13th Symposium of Boundary Layers and Turbulence* (pp. 252–255). Dallas, TX: American Meteorological Society.

Hasselmann, S., Hasselmann, K., Allender, J. H., & Barnett, T. P. (1985). Computations and parameterizations of the nonlinear energy transfer in a gravity-wave spectrum. Part II: Parameterizations of the nonlinear energy transfer for application in wave models. *Journal of Physical Oceanography*, *15*(11), 1378–1391. https://doi.org/10.1175/1520-0485(1985)015<1378:CAPOTN>2.0.CO;2

Herbener, S. R., van den Heever, S. C., Carrió, G. G., Saleeby, S. M., & Cotton, W. R. (2014). Aerosol indirect effects on idealized tropical cyclone dynamics. *Journal of the Atmospheric Sciences*, *71*(6), 2040–2055. https://doi.org/10.1175/JAS-D-13-0202.1

Holland, G. J. (1997). The maximum potential intensity of tropical cyclones. *Journal of the Atmospheric Sciences*, *54*(21), 2519–2541. https://doi.org/10.1175/1520-0469(1997)054<2519:TMPIOT>2.0.CO;2

Jacob, R., Larson, J., & Ong, E. (2005). M × N communication and parallel interpolation in community climate system model version 3 using the model coupling toolkit. *International Journal of High Performance Computing Applications*, *19*(3), 293–307. https://doi.org/10.1177/1094342005056116

Jaeglé, L., Quinn, P. K., Bates, T. S., Alexander, B., & Lin, J.-T. (2011). Global distribution of sea salt aerosols: New constraints from in situ and remote sensing observations. *Atmospheric Chemistry and Physics*, *11*(7), 3137–3157. https://doi.org/10.5194/acp-11-3137-2011

Janssen, P. A. E. M. (1991). Quasi-linear theory of wind-wave generation applied to wave forecasting. *Journal of Physical Oceanography*, *21*(11), 1631–1642. https://doi.org/10.1175/1520-0485(1991)021<1631:QLTOWW>2.0.CO;2

Jin, H., Peng, M. S., Jin, Y., & Doyle, J. D. (2014). An evaluation of the impact of horizontal resolution on tropical cyclone predictions using COAMPS-TC. *Weather and Forecasting*, *29*(2), 252–270. https://doi.org/10.1175/WAF-D-13-00054.1

Jolivet, S., Chane-Ming, F., Barbary, D., & Roux, F. (2013). A numerical study of orographic forcing on TC Dina (2002) in South West Indian Ocean. *Annales Geophysicae*, *31*(1), 107–125. https://doi.org/10.5194/angeo-31-107-2013

Jones, P. W. (1999). First- and second-order conservative remapping schemes for grids in spherical coordinates. *Monthly Weather Review*, *127*(9), 2204–2210. https://doi.org/10.1175/1520-0493(1999)127<2204:FASOCR>2.0.CO;2

Jullien, S., Marchesiello, P., Menkes, C. E., Lefèvre, J., Jourdain, N. C., Samson, G., et al. (2014). Ocean feedback to tropical cyclones: Climatology and processes. *Climate Dynamics*, *43*(9–10), 2831–2854. https://doi.org/10.1007/s00382-014-2096-6

Jullien, S., Menkes, C. E., Marchesiello, P., Jourdain, N. C., Lengaigne, M., Koch-Larrouy, A., et al. (2012). Impact of tropical cyclones on the heat budget of the South Pacific Ocean. *Journal of Physical Oceanography*, *42*(11), 1882–1906. https://doi.org/10.1175/JPO-D-11-0133.1

Kaplan, J., DeMaria, M., & Knaff, J. A. (2010). A revised tropical cyclone rapid intensification index for the Atlantic and Eastern North Pacific basins. *Weather and Forecasting*, *25*(1), 220–241. https://doi.org/10.1175/2009WAF2222280.1

Kudryavtsev, V. N., & Makin, V. K. (2007). Aerodynamic roughness of the sea surface at high winds. *Boundary-Layer Meteorology*, *125*(2), 289–303. https://doi.org/10.1007/s10546-007-9184-7

Large, W. G., McWilliams, J. C., & Doney, S. C. (1994). Oceanic vertical mixing: A review and a model with a nonlocal boundary layer parameterization. *Reviews of Geophysics*, *32*(4), 363–403. https://doi.org/10.1029/94RG01872

Larson, J., Jacob, R., & Ong, E. (2005). The model coupling toolkit: A new Fortran90 toolkit for building multiphysics parallel coupled models. *International Journal of High Performance Computing Applications*, *19*(3), 277–292. https://doi.org/10.1177/1094342005056115

Lebeaupin Brossier, C., Ducrocq, V., & Giordani, H. (2008). Sensitivity of three Mediterranean heavy rain events to two different sea surface fluxes parameterizations in high-resolution numerical modeling. *Journal of Geophysical Research*, *113*, D21109. https://doi.org/10.1029/2007JD009613

Lee, C.-Y., & Chen, S. S. (2012). Symmetric and asymmetric structures of hurricane boundary layer in coupled atmosphere-wave-ocean models and observations. *Journal of the Atmospheric Sciences*, *69*(12), 3576–3594. https://doi.org/10.1175/JAS-D-12-046.1

Lee, C.-Y., & Chen, S. S. (2014). Stable boundary layer and its impact on tropical cyclone structure in a coupled atmosphere-ocean model. *Monthly Weather Review*, *142*(5), 1927–1944. https://doi.org/10.1175/MWR-D-13-00122.1

Lenain, L., & Melville, W. K. (2017). Evidence of sea-state dependence of aerosol concentration in the marine atmospheric boundary layer. *Journal of Physical Oceanography*, *47*(1), 69–84. https://doi.org/10.1175/JPO-D-16-0058.1

Lengaigne, M., Neetu, S., Samson, G., Vialard, J., Krishnamohan, K. S., Masson, S., et al. (2018). Influence of air-sea coupling on Indian Ocean tropical cyclones. *Climate Dynamics*, https://doi.org/10.1007/s00382-018-4152-0, in press.

Lionello, P., Malguzzi, P., & Buzzi, A. (1998). Coupling between the atmospheric circulation and the ocean wave field: An idealized case. *Journal of Physical Oceanography*, *28*(2), 161–177. https://doi.org/10.1175/1520-0485(1998)028<0161:CBTACA>2.0.CO;2

Liu, B., Guan, C., Xie, L., & Zhao, D. (2012). An investigation of the effects of wave state and sea spray on an idealized typhoon using an air-sea coupled modeling system. *Advances in Atmospheric Sciences*, *29*(2), 391–406. https://doi.org/10.1007/s00376-011-1059-7

Liu, B., Liu, H., Xie, L., Guan, C., & Zhao, D. (2011). A coupled atmosphere-wave-ocean modeling system: Simulation of the intensity of an idealized tropical cyclone. *Monthly Weather Review*, *139*(1), 132–152. https://doi.org/10.1175/2010MWR3396.1

Marchesiello, P., Benshila, R., Almar, R., Uchiyama, Y., McWilliams, J. C., & Shchepetkin, A. (2015). On tridimensional rip current modeling. *Ocean Modelling*, *96*, 36–48. https://doi.org/10.1016/j.ocemod.2015.07.003

Masson, V., Le Moigne, P., Martin, E., Faroux, S., Alias, A., Alkama, R., et al. (2013). The SURFEXv7.2 land and ocean surface platform for coupled or offline simulation of earth surface variables and fluxes. *Geoscientific Model Development*, *6*(4), 929–960. https://doi.org/10.5194/gmd-6-929-2013

McCluskey, C. S., Hill, T. C. J., Malfatti, F., Sultana, C. M., Lee, C., Santander, M. V., et al. (2017). A dynamic link between ice nucleating particles released in nascent sea spray aerosol and oceanic biological activity during two mesocosm experiments. *Journal of the Atmospheric Sciences*, *74*(1), 151–166. https://doi.org/10.1175/JAS-D-16-0087.1

Menemenlis, D., Campin, J., Heimbach, P., Hill, C., Lee, T., Nguyen, A., et al. (2008). ECCO2: High resolution global ocean and sea ice data synthesis. *Eos, Transactions American Geophysical Union*, *89*(53), Fall Meeting Supplement, Abstract OS31C-1292.

Mlawer, E. J., Taubman, S. J., Brown, P. D., Iacono, M. J., & Clough, S. A. (1997). Radiative transfer for inhomogeneous atmospheres: RRTM, a validated correlated-k model for the longwave. *Journal of Geophysical Research*, *102*(D14), 16663–16682. https://doi.org/10.1029/97JD00237

Monahan, E. C., Spiel, D. E., & Davidson, K. L. (1986). *A model of marine aerosol generation via whitecaps and wave disruption* (pp. 167–174). Dordrecht, the Netherlands: Springer. https://doi.org/10.1007/978-94-009-4668-2_16

Moon, I.-J., Ginis, I., Hara, T., & Thomas, B. (2007). A physics-based parameterization of air-sea momentum flux at high wind speeds and its impact on hurricane intensity predictions. *Monthly Weather Review*, *135*(8), 2869–2878. https://doi.org/10.1175/MWR3432.1

Moon, I.-J., Ginis, I., Hara, T., Tolman, H. L., Wright, C. W., & Walsh, E. J. (2003). Numerical simulation of sea surface directional wave spectra under hurricane wind forcing. *Journal of Physical Oceanography*, *33*(8), 1680–1706. https://doi.org/10.1175/2410.1

Noilhan, J., & Planton, S. (1989). A simple parametrization of land surface processes for meteorological models. *Monthly Weather Review*, *117*, 536–549.

Nuissier, O., Rogers, R. F., & Roux, F. (2005). A numerical simulation of Hurricane Bret on 22–23 August 1999 initialized with airborne Doppler radar and dropsonde data. *Quarterly Journal of the Royal Meteorological Society*, *131*(605), 155–194. https://doi.org/10.1256/qj.02.233

Ovadnevaite, J., Manders, A., De Leeuw, G., Ceburnis, D., Monahan, C., Partanen, A.-I., et al. (2014). A sea spray aerosol flux parameterization encapsulating wave state. *Atmospheric Chemistry and Physics*, *14*, 1837–1852. https://doi.org/10.5194/acp-14-1837-2014

Pantillon, F. P., Chaboureau, J.-P., Mascart, P. J., & Lac, C. (2013). Predictability of a Mediterranean tropical-like storm downstream of the extratropical transition of hurricane Helene (2006). *Monthly Weather Review*, *141*(6), 1943–1962. https://doi.org/10.1175/MWR-D-12-00164.1

Pantillon, F., Chaboureau, J.-P., & Richard, E. (2015). Remote impact of North Atlantic hurricanes on the Mediterranean during episodes of intense rainfall in autumn 2012. *Quarterly Journal of the Royal Meteorological Society*, *141*(688), 967–978. https://doi.org/10.1002/qj.2419

Pantillon, F., Chaboureau, J.-P., & Richard, E. (2016). Vortex-vortex interaction between Hurricane Nadine (2012) and an Atlantic cut-off dropping the predictability over the Mediterranean. *Quarterly Journal of the Royal Meteorological Society*, *142*(S1), 419–432. https://doi.org/10.1002/qj.2635

Penven, P., Debreu, L., Marchesiello, P., & McWilliams, J. C. (2006). Evaluation and application of the ROMS 1-way embedding procedure to the central California upwelling system. *Ocean Modelling*, *12*(1–2), 157–187. https://doi.org/10.1016/j.ocemod.2005.05.002

Pinty, J.-P., & Jabouille, P. (1998). *A mixed-phase cloud parameterization for use in a mesoscale non-hydrostatic model: Simulations of a squall line and of orographic precipitation*. In Proceedings of Conference on Cloud Physics (pp. 217–220). Everett, WA: American Meteorological Society.

Potter, H., Collins, C. O., Drennan, W. M., & Graber, H. C. (2015). Observations of wind stress direction during Typhoon Chaba (2010). *Geophysical Research Letters*, *42*, 9898–9905. https://doi.org/10.1002/2015GL065173

Powell, M. D., Vickery, P. J., & Reinhold, T. A. (2003). Reduced drag coefficient for high wind speeds in tropical cyclones. *Nature*, *422*(6929), 279–283. https://doi.org/10.1038/nature01481

Price, J. F. (1981). Upper ocean response to a hurricane. *Journal of Physical Oceanography*, *11*(2), 153–175. https://doi.org/10.1175/1520-0485(1981)011<0153:UORTAH>2.0.CO;2

Queffeulou, P., & Croizé-Fillon, D. (2017). *Global altimeter SWH data set–Version 11.0* (technical report). Plouzané, France: IFREMER.

Randerson, D. (Eds.) (1984). *Atmospheric science and power production* (Tech. Rep. DOE/TIC-27601). Washington, DC: Technical Information Center, Division of Biomedical Environmental Research, U.S. Department of Energy. https://doi.org/10.2172/6503687

Richter, D. H., & Stern, D. P. (2014). Evidence of spray-mediated air-sea enthalpy flux within tropical cyclones. *Geophysical Research Letters*, *41*, 2997–3003. https://doi.org/10.1002/2014GL059746

Rosenfeld, D., Andreae, M. O., Asmi, A., Chin, M., de Leeuw, G., Donovan, D. P., et al. (2014). Global observations of aerosol-cloud-precipitation-climate interactions. *Reviews of Geophysics*, *52*, 750–808. https://doi.org/10.1002/2013RG000441

Rosenfeld, D., Woodley, W. L., Khain, A., Cotton, W. R., Carrió, G., Ginis, I., et al. (2012). Aerosol effects on microstructure and intensity of tropical cyclones. *Bulletin of the American Meteorological Society*, *93*(7), 987–1001. https://doi.org/10.1175/BAMS-D-11-00147.1

Rotunno, R., & Emanuel, K. A. (1987). An air-sea interaction theory for tropical cyclones. Part II: Evolutionary study using a nonhydrostatic axisymmetric numerical model. *Journal of the Atmospheric Sciences*, *44*(3), 542–561. https://doi.org/10.1175/1520-0469(1987)044<0542:AAITFT>2.0.CO;2

Samson, G., Masson, S., Lengaigne, M., Keerthi, M. G., Vialard, J., Pous, S., et al. (2014). The NOW regional coupled model: Application to the tropical Indian Ocean climate and tropical cyclone activity. *Journal of Advances in Modeling Earth Systems*, *6*, 700–722. https://doi.org/10.1002/2014MS000324

Seinfeld, J. H., & Pandis, S. N. (2016). *Atmospheric chemistry and physics: From air pollution to climate change* (1152 p.). Hoboken, NJ: John Wiley & Sons.

Seyfried, L., Marsaleix, P., Richard, E., & Estournel, C. (2017). Modelling deep-water formation in the North-West Mediterranean Sea with a new air-sea coupled model: Sensitivity to turbulent flux parameterizations. *Ocean Science*, *13*, 1093–1112. https://doi.org/10.5194/os-13-1093-2017

Shanas, P., Sanil Kumar, V., & Hithin, N. (2014). Comparison of gridded multi-mission and along-track mono-mission satellite altimetry wave heights with in situ near-shore buoy data. *Ocean Engineering*, *83*, 24–35. https://doi.org/10.1016/j.oceaneng.2014.03.014

Shay, L. K., Elsberry, R. L., & Black, P. G. (1989). Vertical structure of the ocean current response to a hurricane. *Journal of Physical Oceanography*, *19*(5), 649–669. https://doi.org/10.1175/1520-0485(1989)019<0649:VSOTOC>2.0.CO;2

Shchepetkin, A. F., & McWilliams, J. C. (1998). Quasi-monotone advection schemes based on explicit locally adaptive dissipation. *Monthly Weather Review*, *126*(6), 1541–1580. https://doi.org/10.1175/1520-0493(1998)126<1541:QMASBO>2.0.CO;2

Smith, R. K., Montgomery, M. T., & Van Sang, N. (2009). Tropical cyclone spin-up revisited. *Quarterly Journal of the Royal Meteorological Society*, *135*(642), 1321–1335. https://doi.org/10.1002/qj.428

Smith, S. D. (1988). Coefficients for sea-surface wind stress, heat-flux, and wind profiles as a function of wind-speed and temperature. *Journal of Geophysical Research*, *93*(C12), 15467–15472. https://doi.org/10.1029/JC093iC12p15467

Sofiev, M., Soares, J., Prank, M., de Leeuw, G., & Kukkonen, J. (2011). A regional-to-global model of emission and transport of sea salt particles in the atmosphere. *Journal of Geophysical Research*, *116*, D21302. https://doi.org/10.1029/2010JD014713

Song, Y., & Haidvogel, D. (1994). A semi-implicit ocean circulation model using a generalized topography-following coordinate system. *Journal of Computational Physics*, *115*(1), 228–244. https://doi.org/10.1006/jcph.1994.1189

Tannehill, I. R. (1936). Sea swells in relation to movement and intensity of tropical storms. *Monthly Weather Review*, *64*(7), 231–238. https://doi.org/10.1175/1520-0493(1936)64<231b:SSIRTM>2.0.CO;2

The WAVEWATCH III Development Group (WW3DG) (2016). *User manual and system documentation of WAVEWATCH III version 5.16* (Tech. Note 329). College Park, MD: NOAA/NWS/NCEP/MMAB.

Tolman, H. L. (1992). Effects of numerics on the physics in a third-generation wind-wave model. *Journal of Physical Oceanography*, *22*(10), 1095–1111. https://doi.org/10.1175/1520-0485(1992)022<1095:EONOTP>2.0.CO;2

Tolman, H. L. (2002). Alleviating the garden sprinkler effect in wind wave models. *Ocean Modelling*, *4*(3–4), 269–289. https://doi.org/10.1016/S1463-5003(02)00004-5

Tulet, P., Crassier, V., Cousin, F., Suhre, K., & Rosset, R. (2005). ORILAM, a three-moment lognormal aerosol scheme for mesoscale atmospheric model: Online coupling into the Meso-NH-C model and validation on the Escompte campaign. *Journal of Geophysical Research*, *110*, D18201. https://doi.org/10.1029/2004JD005716

Uchiyama, Y., McWilliams, J. C., & Restrepo, J. M. (2009). Wave-current interaction in nearshore shear instability analyzed with a vortex force formalism. *Journal of Geophysical Research*, *114*, C06021. https://doi.org/10.1029/2008JC005135

Voldoire, A., Decharme, B., Pianezze, J., Lebeaupin Brossier, C., Sevault, F., Seyfried, L., et al. (2017). SURFEX v8.0 interface with OASIS3-MCT to couple atmosphere with hydrology, ocean, waves and sea-ice models, from coastal to global scales. *Geoscientific Model Development*, *10*(11), 4207–4227. https://doi.org/10.5194/gmd-10-4207-2017

Wada, A., Uehara, T., & Ishizaki, S. (2014). Typhoon-induced sea surface cooling during the 2011 and 2012 typhoon seasons: Observational evidence and numerical investigations of the sea surface cooling effect using typhoon simulations. *Progress in Earth and Planetary Science*, *1*(1), 11. https://doi.org/10.1186/2197-4284-1-11

Wada, A., Usui, N., & Sato, K. (2012). Relationship of maximum tropical cyclone intensity to sea surface temperature and tropical cyclone heat potential in the North Pacific Ocean. *Journal of Geophysical Research*, *117*, D11118. https://doi.org/10.1029/2012JD017583

Wang, X., Deane, G. B., Moore, K. A., Ryder, O. S., Stokes, M. D., Beall, C. M., et al. (2017). The role of jet and film drops in controlling the mixing state of submicron sea spray aerosol particles. *Proceedings of the National Academy of Sciences of the United States of America*, *114*(27), 6978–6983. https://doi.org/10.1073/pnas.1702420114

Wang, Y., Kepert, J. D., & Holland, G. J. (2001). The effect of sea spray evaporation on tropical cyclone boundary layer structure and intensity. *Monthly Weather Review*, *129*(10), 2481–2500. https://doi.org/10.1175/1520-0493(2001)129<2481:TEOSSE>2.0.CO;2

Warner, J. C., Armstrong, B., He, R., & Zambon, J. B. (2010). Development of a coupled ocean-atmosphere-wave-sediment transport (COAWST) modeling system. *Ocean Modelling*, *35*(3), 230–244. https://doi.org/10.1016/j.ocemod.2010.07.010

Wilson, T. W., Ladino, L. A., Alpert, P. A., Breckels, M. N., Brooks, I. M., Browse, J., et al. (2015). A marine biogenic source of atmospheric ice-nucleating particles. *Nature*, *525*(7568), 234–238.

Wright, C. W., Walsh, E. J., Vandemark, D., Krabill, W. B., Garcia, A. W., Houston, S. H., et al. (2001). Hurricane directional wave spectrum spatial variation in the open ocean. *Journal of Physical Oceanography*, *31*(8), 2472–2488. https://doi.org/10.1175/1520-0485(2001)031<2472:HDWSSV>2.0.CO;2

Zambon, J. B., He, R., & Warner, J. C. (2014). Investigation of hurricane Ivan using the coupled ocean-atmosphere-wave-sediment transport (COAWST) model. *Ocean Dynamics*, *64*(11), 1535–1554. https://doi.org/10.1007/s10236-014-0777-7

Zhang, H., Chen, D., Zhou, L., Liu, X., Ding, T., & Zhou, B. (2016). Upper ocean response to typhoon Kalmaegi (2014). *Journal of Geophysical Research: Oceans*, *121*, 6520–6535. https://doi.org/10.1002/2016JC012064

Zhao, B., Qiao, F., Cavaleri, L., Wang, G., Bertotti, L., & Liu, L. (2017). Sensitivity of typhoon modeling to surface waves and rainfall. *Journal of Geophysical Research: Oceans*, *122*, 1702–1723. https://doi.org/10.1002/2016JC012262